

UNIVERSIDAD DE CANTABRIA  
Instituto de Física de Cantabria  
IFCA (CSIC-UC)



Sensores de silicio avanzados para futuros  
experimentos colisionadores

*”Advanced silicon sensors for future  
collider experiments”*

Tesis Doctoral  
Esteban Currás Rivera

Santander, Abril 2017

---

## Declaración de Autoría

**Iván Vila Álvarez**, Doctor en Ciencias Físicas y Científico Titular del Consejo Superior de Investigaciones Científicas,

**Certifica** que la presente memoria

**Sensores de silicio avanzados para futuros experimentos colisionadores (*Advanced silicon sensors for future collider experiments*)**

ha sido realizada por Esteban Currás Rivera bajo mi dirección en el Instituto de Física de Cantabria, para optar al título de Doctor por la Universidad de Cantabria. Considero que esta memoria contiene aportaciones científicas suficientemente relevantes como para constituir la Tesis Doctoral del interesado.

En Santander, a 27 de abril de 2017.

Iván Vila Álvarez

---

*Esta tesis ha sido desarrollada dentro del “Programa Oficial de Doctorado en Ciencias, Tecnología y Computación” regulado por el Real Decreto 1393/2007 (BOE núm. 36, de 10 de febrero de 2010. RUCT: 5310324) con mención hacia la excelencia (BOE núm. 253, de 20 de octubre de 2011. Referencia:MEE2011-0061). Para la realización de esta tesis, Esteban Currás Rivera ha disfrutado de una ayuda en el Instituto de Física de Cantabria (IFCA), centro mixto dependiente del Consejo Superior de Investigaciones Científicas (CSIC) y de la Universidad de Cantabria (UC). Durante la misma, para fomentar la excelencia del programa de doctorado, la formación del doctorando y la obtención de la Mención Internacional en el título de Doctor en Ciencias, Tecnología y Computación concedida por Orden ECD/3628-2011 de 26 de diciembre (BOE de 14 de enero de 2012), el autor ha realizado una estancia en el laboratorio de detectores de estado sólido del Centro Europeo de Investigación Nuclear (CERN) con una duración de dos años y tres meses (de octubre de 2014 a diciembre de 2016).*

---

## Acknowledgment

I would like to thank everyone who contributed to this work, advised and supported me during these challenging years of interesting, motivating and constructive work, with many good moments and very tough work behind.

First of all I would like to thank Prof. Dr. Iván Vila for his impressive supervision of this work giving me support and always advising me in the right direction. At the same time, I am also very thankful to Dr. Michael Moll and Dr. Marcello Mannelli for their incredible supervision during my stay at CERN. They always encouraged me with my work giving me excellent advices and following all my steps in detail for a good understanding of my work. Without all of them, this work would not have been possible.

I am grateful to all the members of the IFCA group with who I worked during my first two years. They made my work much easier with their help, advise and always the best availability when I needed it. I am also grateful to all the members of the SSD department at CERN leaded by Michael, with who I spent more than two years and they made my work much easier too. They were always available for advice and help and they always kept a very friendly working atmosphere.

I am very thankful to the HGICAL group lead by Marcello, for allowing me to have taken part in this interesting project. We have had very constructive meetings in which I have learned many things related to many aspect of my work and giving me the best possible overview the project. At the same time, I am very thankful to Dr. Dave Barney and all his group for all the time that we shared together during the test-beams and later analysis and discussions. I would like to thanks everyone who was involved in all the timing test-beams and later analysis of the data for allowing me to have taken part in the task from which learned many new things.

I am very thankful to Dr. Shervin Nourbakhsh and Dr. Georg Steinbrueck and all his group at Hamburg University for guiding me at the beginning of my work in the HGICAL project.

I would like to thank RD50 coloboration, it is an honor to be a part of this collaboration and participate in the always very interesting and constructive workshops. Finally, I am grateful to the European project AIDA2020 who supported part of my work in this thesis.



# Contents

<b>Preface</b>	<b>ix</b>
<b>1 Introduction</b>	<b>1</b>
1.1 The High Granularity Calorimeter at CMS . . . . .	5
1.2 Low-material Long-ladder tracker systems for lepton colliders . . . . .	11
<b>2 Silicon detectors technology and radiation damage</b>	<b>15</b>
2.1 Overview . . . . .	15
2.2 Physics of silicon detectors . . . . .	16
2.2.1 Working principle and doping . . . . .	16
2.2.2 The pn-junction . . . . .	17
2.3 Signal formation in silicon detectors . . . . .	20
2.3.1 Ramo's Theorem . . . . .	20
2.3.2 Signal formation . . . . .	20
2.4 Silicon crystal production methods . . . . .	21
2.4.1 Czochralski process . . . . .	22
2.4.2 Float Zone process . . . . .	22

---

2.4.3	Epitaxial process . . . . .	25
2.5	Radiation damage . . . . .	26
2.5.1	The NIEL hypothesis . . . . .	26
2.5.2	Annealing . . . . .	28
2.5.3	Trapping . . . . .	29
2.5.4	Impact on the reverse current . . . . .	30
2.5.5	Effects on depletion voltage . . . . .	31
2.5.6	Charge Multiplication . . . . .	32
2.5.7	Surface damage . . . . .	33
<b>3</b>	<b>Experimental methods</b>	<b>35</b>
3.1	Electrical characterization: current-voltage and capacitance-voltage . . . . .	36
3.1.1	Current-Voltage characterization . . . . .	37
3.1.2	Capacitance-Voltage characterization . . . . .	38
3.2	Laser characterization: Transient Current Technique . . . . .	42
3.2.1	Adjustment of the laser intensity . . . . .	46
3.3	Radioactive source characterization . . . . .	48
3.3.1	Description of the set-up . . . . .	49
3.3.2	Data taking . . . . .	52
3.3.3	Analysis . . . . .	53
3.3.4	Oscilloscope and amplifier calibration . . . . .	54
3.4	Test beam . . . . .	56

3.5	Irradiation facilities . . . . .	58
<b>4</b>	<b>Radiation tolerance assessment of deep diffused float zone and epitaxial diodes</b>	<b>61</b>
4.1	Devices under investigation and irradiation fluences . . . . .	61
4.2	Current-voltage characterization: bulk damage and power consumption . . . . .	65
4.3	Capacitance-voltage characterization: thickness study . . . . .	70
4.4	Transient current technique: charge collection efficiency studies . . . . .	76
4.4.1	Study of the surface homogeneity . . . . .	79
4.4.2	Reproducibility of the measurements . . . . .	84
4.4.3	Thickness measurement using edge-TCT technique . . . . .	85
4.5	Radioactive source characterization . . . . .	86
<b>5</b>	<b>Timing performance of deep diffused Float Zone diodes</b>	<b>95</b>
5.1	Introduction . . . . .	95
5.2	Experimental arrangements . . . . .	96
5.3	Analysis . . . . .	98
5.3.1	MIP calibration . . . . .	98
5.3.2	Multi MIP Signal study . . . . .	100
5.3.3	Timing resolution . . . . .	101
<b>6</b>	<b>Two-dimensional position-sensitive microstrip sensor with resistive electrodes</b>	<b>109</b>
6.1	Concept: Resistive charge division in microstrips sensors . . . . .	110
6.2	Proof of concept prototypes . . . . .	112
6.3	Electrical simulation vs laser characterization . . . . .	113

---

6.4	Studies on the position measurement error . . . . .	116
6.5	Signal-to-noise studies with radioactive source . . . . .	119
6.6	Test-beam studies: beam monitoring and spacial resolution . . . . .	122
6.6.1	Experimental set-up . . . . .	122
6.6.2	Analysis and results . . . . .	124
<b>7</b>	<b>Summary and conclusions</b>	<b>131</b>
<b>8</b>	<b>Resumen</b>	<b>135</b>
8.1	Introducción . . . . .	135
8.2	Técnicas de caracterización . . . . .	137
8.3	Resultados . . . . .	138
8.3.1	Daño por radiación en diodos de silicio . . . . .	139
8.3.2	Resolución temporal en diodos de silicio . . . . .	141
8.3.3	Detectores de microtiras sensibles en dos coordenadas . . . . .	142
8.4	Conclusiones . . . . .	142
<b>A</b>	<b>Acronyms</b>	<b>147</b>
	<b>List of Figures</b>	<b>151</b>
	<b>List of Tables</b>	<b>159</b>
	<b>Bibliography</b>	<b>161</b>

# Preface

This work is submitted for the degree of Doctor of Philosophy in Science, Technology and Computation at the University of Cantabria. The work done here was conducted under the supervision of Doctor Iván Vila Álvarez at the Instituto de Física de Cantabria (IFCA). The work was started at IFCA in September 2012 and finished at CERN from October 2014 to April 2017.

The goal of this work is the study of new silicon sensors for future experiments at particle colliders. The characterization, set-ups used and results of this work are presented. The work and results herein presented are original.



# Chapter 1

## Introduction

Elementary Particle physics, also known as high energy physics (HEP), is the branch of physics focused on the study of the fundamental constituents of matter. Modern particle physics research is focused on subatomic particles which are governed by quantum mechanics. Since the 1970s, HEP has described the fundamental structure of matter using a series of equations called the Standard Model (SM). This model describes how everything observed in the Universe is made from a few basic blocks called fundamental particles. The term fundamental particles is applied to those particles that are, according to current understanding, presumed to be indivisible and not composed of other particles.

Historically, the particle accelerators are the most successful tool that physicists have to discover new particles. In the last decades, diverse particle accelerators have been developed and very important discoveries have been made using them. The most important ones in term of discoveries are:

- The Super Proton Synchrotron (SPS) [1] is a particle accelerator of the synchrotron type at CERN (the European Organization for Nuclear Research). It is housed in a circular tunnel of nearly 7 km of circumference and it started its operation in 1976. It is capable to accelerate protons up to 450 GeV and now it is used as the final injector for the Large Hadron Collider (LHC) [2]. A major highlight came in 1983 with the Nobel-prize-winning discovery of W and Z particles, with the SPS running as a proton-antiproton collider.
- The Large Electron-Positron Collider (LEP) [3] was one of the largest particle accelerators ever built. It was constructed at CERN and it collided electrons with positrons at

---

energies that reached 209 GeV. It was a circular collider of 27 km of circumference that was in operation from 1989 until 2000. Then, it was replaced for the LHC. The main achievements of LEP was to determined the number of families of particles containing what are known as light neutrinos in 1989.

- The Tevatron [4] was a circular particle accelerator placed at the Fermi National Accelerator Laboratory (Fermilab), in Illinois, United States. The Tevatron was a synchrotron that accelerated protons and antiprotons in almost 7 km ring to energies of up to 1 TeV. The Tevatron was completed in 1983 and was in operation until 2011. It confirmed the existence of several subatomic particles, but the most important achievement was in 1995 when the discovery of the top quark was announced, and by 2007 its mass was measured to a precision of nearly 1%.
- Currently, the world's largest and most powerful particle collider existing is the previous mentioned LHC, places at CERN in the France-Switzerland border near Geneva, Switzerland. It was built between 1998 and 2008, it lies in the same tunnel as its predecessor LEP and in 2015 it was able to rich a total energy of 13 TeV. The proton-proton collision is the primary operation method and the most important achievement was the observation of the Higgs boson announced in 2012.

The LHC's collider tunnel contains two parallel beamlines that intersect at four points. More than 1000 dipole magnets keep the beams on their circular path and almost 400 quadrupole magnets are used to keep the beams focused. On each interaction point there is a very strong quadrupole magnets for maximizing the probability of interactions where the two beams cross. The LHC's aim is to allow physicists to test the predictions of different theories of HEP and in particular, to further test the properties of the Higgs boson and the large family of new particles predicted by theory. In figure 1.1 can be seen a schematic map of the CERN accelerator complex.

At present, the near term European and international strategies of the particle physics community are centred on full exploitation of the physics potential of the LHC through its high-luminosity upgrade (HL-LHC). But a wide number of next generation collider facilities have been proposed and are currently under consideration for the medium and far future strategies of the particle physics community [6]. The most relevant proposals are listed below:

- The International Linear Collider (ILC) [7] is a proposed linear particle accelerator of about 40 km long, that will collide electrons with positrons with a planned energy

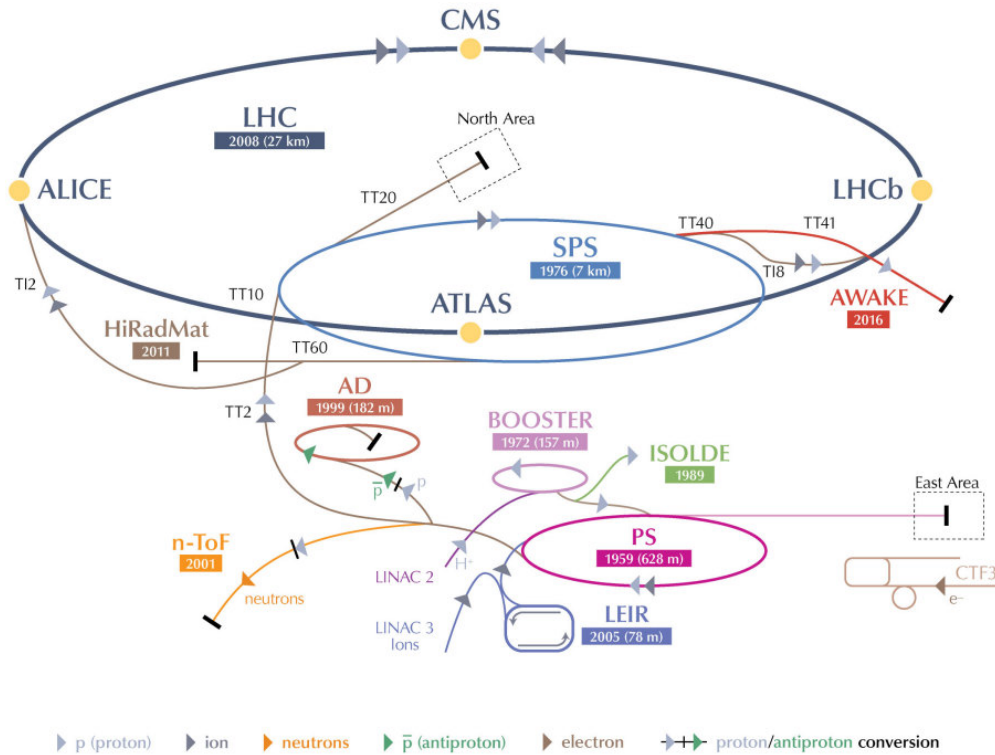


Figure 1.1: Schematic map of the CERN accelerator complex [5].

collision of 500 GeV (up to 1 TeV in a later upgrade) and an expected luminosity of  $2 \times 10^{34} \text{ cm}^{-2} \text{ s}^{-1}$ . The proposed location for the ILC is Japan. But studies for an alternative project, the Compact Linear Collider (CLIC) are also underway.

- The Compact Linear Collider (CLIC) [8] is a proposed linear particle accelerator of about 60 km long. It is designed to perform electron/positron collisions at energies of 3 TeV with a goal luminosity of  $5 \times 10^{34} \text{ cm}^{-2} \text{ s}^{-1}$ . The proposed location for the CLIC is CERN area (Switzerland/France).
- The Future Circular Collider (FCC) [9] is a proposed circular collider of about 100 Km of circumference. It aims to complement existing technical designs for the two linear electron/positron colliders mentioned (ILC and CLIC). The study has an emphasis on two possible collider scenarios: a hadron collider (proton/proton) with a collision energy up to 100 TeV and a lepton collider (electron/positron) with a collision energy up to 250 GeV. In both cases the luminosity expected is around  $5 \times 10^{34} \text{ cm}^{-2} \text{ s}^{-1}$ . The proposed location for the LCC is CERN area (Switzerland/France).
- The Circular Electron Positron Collider (CEPC) and the Super Proton-Proton Collider

---

(SPPC) [10] are two-stage circular collider project proposed by China of 54 km of circumference that will be located in China. The CEPC will perform electron/positron collisions at energies of 250 GEV and the SPPC will perform proton/proton collisions at energy of about 50 TeV. In both cases the goal luminosity is  $5 \times 10^{34} \text{ cm}^{-2}\text{s}^{-1}$ .

In parallel with the accelerators developments, the detector technologies have evolved and improved along these decades to cope with the new technological challenges required by the ever increasing detector performance requirements and, in some cases also, by the increasing hostile operation conditions. Concerning the future HL-LHC, the current detector R&D is focused into the following lines:

- Radiation tolerance up to a hadron fluence of  $10^{16} n_{eq}/\text{cm}^2$  and  $1GGy$  dose for the closest detector to the interaction point and low eta regions.
- Disentangling the multiple hard-scattering interactions per bunch crossing (pile-up events); around 200 primary vertices are expected at the peak luminosity.
- To cope with the high track occupancy environment, with tens of thousands of tracks per bunch crossing.

Complimentary to the HL-LHC detector requirements, the future leptonic colliders impose additional challenges, namely:

- Very low material budget tracking and vertexing detectors to reduce the effect of the multiple scattering on their performance.
- Very low power dissipation sensing technologies to avoid active cooling systems and the consequent material budget burden.

Common to both types of collider experiments, calorimetry has evolved towards the use of particle-flow algorithms requiring an unprecedented granularity with a number of readout channels similar to the current tracker systems; implementing a truly *imaging-calorimetry*.

During this last decade, the silicon-based sensing technologies have become the enabling technology able to cope with all the above listed challenges. Silicon-based sensors are being considered or used as the baseline sensing solution for vertexing, tracking, calorimetry and

muon identification in future detector experiments; moreover, the emerging field of track timing detectors (to be used for disentangling the pile-up events) is also making profuse use of silicon sensors with intrinsic signal gain.

In accordance with the above mentioned RD lines, in this thesis, we address two key technological challenges: the radiation tolerance assessment and timing performance studies of thin planar diodes to be used as sensing technology in the recently approved CMS forward sampling calorimeter for the HL-LHC operation, the High Granularity Calorimeter (HGCal); and, complementary, we carried out a detailed study of a novel kind of position-sensitive microstrip sensors for ionising particles which implements the well established charge-division method to determine the particle impinging position along the microstrip electrode direction; this technology could become an interesting low-material budget solution for the new generation of tracking detectors to be operated in the future lepton collider experiments. In the following sections, we will introduce briefly the experimental contexts on which this two technologies can be implemented.

## 1.1 The High Granularity Calorimeter at CMS

As previously mentioned, the full exploitation of the LHC is the highest priority in the European Strategy for Particle Physics [11]. In order to extend its discovery potential, the LHC will need a major upgrade around 2020 to increase its luminosity (rate of collisions) by a factor of 10 beyond the original design value (from 300 to 3000 fb<sup>-1</sup>). This proposal upgrade is called the HL-LHC (High Luminosity Large Hadron Collider) or phase-II [12]. HL-LHC relies on a number of key innovative technologies, representing exceptional technological challenges, such as cutting-edge 13 Tesla superconducting magnets, very compact and ultra-precise superconducting cavities for beam rotation, and 300 m long high power superconducting links with zero energy dissipation. The HL-LHC is expected to operate during 10 years.

Under this conditions the performance degradation of detectors due to integrated radiation dose/fluence will need to be addressed. The CMS collaboration is planning to upgrade many components in order to maintain the physics performance for the HL-LHC. Some of these components are the calorimeters, that within the planned HL-LHC physics program are critical for the identification and reconstruction of photons and electrons and the measurements of jets and missing transverse momentum. The existing CMS calorimeters were designed to

---

meet these challenges for  $500 \text{ fb}^{-1}$  at the LHC over 10 years of data-taking. The HL-LHC performance criteria require a re-examination of the ability of the detector active material and electronics to meet the requirements of  $3000 \text{ fb}^{-1}$ . Thus, upgrades to the calorimeters are proposed including the replacement of the endcap calorimetry systems to overcome the detector degradation mainly due to the high integrated doses that will sustain and the pileup effect that will become more severe. To address these challenges, CMS proposes a new design for the endcap calorimeters with a new high-granularity calorimeter. It will include silicon as an active material in the electromagnetic calorimeter (EE) and the high-radiation regions of the front hadron calorimeter (FH) and the back hadron calorimeter (BH). Nevertheless, in the low-radiation regions of the FH and BH, the active material will be plastic scintillator with silicon photomultiplier (SiPM). The proposed design incorporates a silicon with Cu, CuW and Pb absorber in the electromagnetic section followed by two hadronic sections, both using steel as the primary absorber material. The high transverse and longitudinal granularity of the detector allows tracking and separation of signal and pileup particles inside the calorimeter. A dense high-granularity calorimeter offers the opportunity of high performance in the presence of high pileup. For high-luminosity running in the LHC, the proposed calorimeter offers the prospect of resolving single particles and jets in the dense pileup environment of the forward (endcap) regions.

The overall design of the HGCal, is shown in Figure 1.2. The volume begins with the electromagnetic endcap calorimeter with a Cu/CuW/Pb-silicon sampling electromagnetic calorimeter of 28 layer, with a depth of about  $25 X_0$  and  $1.3 \lambda$ . Moving outwards from the interaction region, it is followed by the front hadron calorimeter, which is a steel-silicon/scintillator calorimeter of 12 layers and  $3.5 \lambda$  deep. This is followed by a  $5 \lambda$  steel-silicon/scintillator sampling backing calorimeter for a total calorimeter depth of  $10 \lambda$  measured in the longitudinal direction.

The EE and the high-radiation regions of the FH and BH will use planes of silicon as the active medium, while in the low-radiation regions of the FH and BH, can be constructed with plastic scintillator, as is the current HE.

For the EE a variable longitudinal sampling is proposed: 10 layers of  $0.65 X_0$  thickness absorber, then 10 layers of  $0.88 X_0$  thickness absorbers and finally 8 layers of  $1.26 X_0$  thickness absorbers all of them followed by a plane of silicon. The FH and the BH have a thickness of  $3.5 \lambda$  and  $5 \lambda$  respectively, with 12 samplings each, and a total thickness of about 60 cm. Each sampling layer in the FH, BH and EE, is read out independently. Table 1.1 shows the main parameters of the EE and FH.

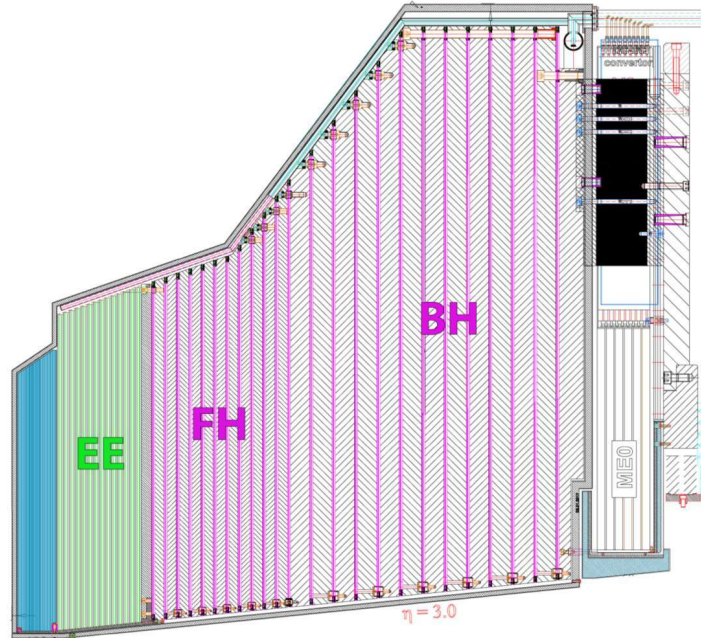


Figure 1.2: Technical drawing of the HGCal overall structure. The EE at the front face. Directly behind it there is the FH. Behind that is the BH [13].

	EE	FH & BH	Total
Area of silicon	380	209	589
Channels	4.3M	1.8M	6.1M (1)
Detector modules	13.9k	7.6k	21.5k
Weight (one endcap) (tonnes)	16.2	36.5	52.7
Number of Si planes	28	24	52

Table 1.1: Parameters of the EE, FH and BH.

The overall mechanical design of the EE is based on the EE ILD prototype what is described in Vol.4 of the ILC TDR [14], but with a modified radial geometry. A carbon-fiber structure integrates alternatively tungsten absorber plates and empty slots in which the "cassettes" are inserted. Each cassette consists of two active planes and their associated front-end electronics on either side of absorber material. The absorber material provides both mechanical structure and support, and cooling. The structure is illustrated in figure 1.3. The cassette is built up on either side of a 6 mm-thick copper plate containing cooling channels. Pair of hexagonal silicon sensor wafers are mounted on a printed circuit board. The other faces of the sensors are glued to a tungsten-copper composite baseplate of appropriate thickness in terms of radiation length. A thin Kapton layer between the baseplate and the silicon wafer ensures high voltage insulation of the sensor back-plane.

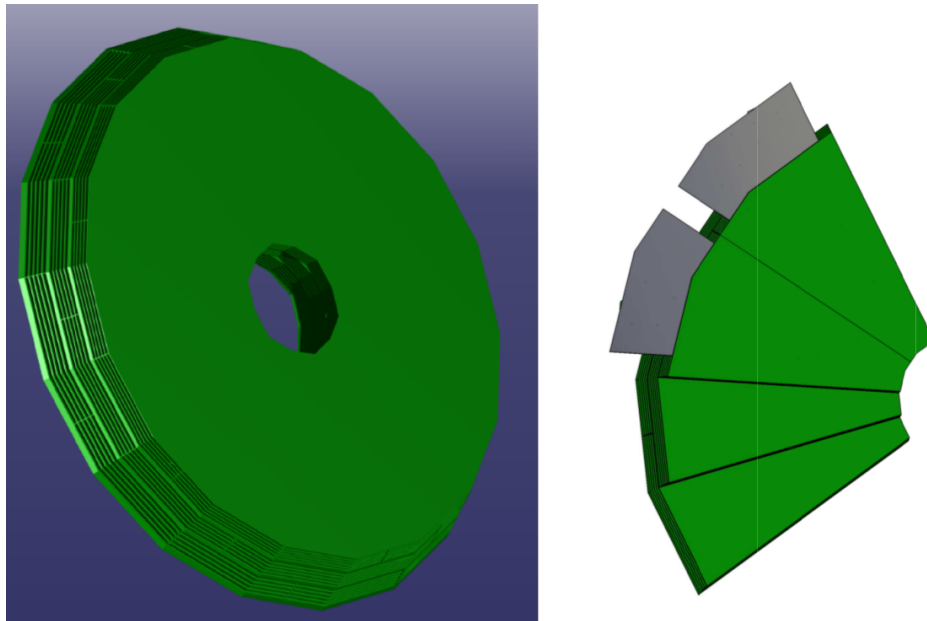


Figure 1.3: (Left) EE carbon-fibre structure integrating tungsten absorber plates alternating with empty slots. (Right) Insertion of a cassette into a slot the structure [13].

The overall mechanical structure of FH and the BH is a bolted structure following the mechanical structure of the current HE, but with cassettes, similar to those for EE but carrying only a single sensor plane, slid into the slots between the brass plates. In these cassettes, the baseplate, between the sensor wafer and the Cu cooling plate, is not required to function as an absorber.

Evaporative CO<sub>2</sub> cooling will be used. CO<sub>2</sub> evaporates from its liquid phase between  $-56^{\circ}\text{C}$  and  $+31^{\circ}\text{C}$  and a practical range of application is from  $-45^{\circ}\text{C}$  to  $+25^{\circ}\text{C}$ . The cooling

fluid would pass through stainless steel pipes embedded in the copper plates. The total power dissipated by the front-end ASIC is estimated to be 10.5 mW/channel, resulting in a total of 65 kW for both endcaps. To this must be added the power needed to drive the data links for the trigger, control and readout, giving a total of 100 kW. A further 25 kW must be added to account for the power dissipated by the leakage current across the sensors after  $3000 fb^{-1}$ , giving a total of 125 kW of power dissipated by the system inside the cold volume.

The silicon sensors for the HGC will be simple, large area, single-sided, and its readout cells will be DC-coupled. The sensors will have an active thickness of 300, 200, or 100  $\mu\text{m}$ , determined by the neutron fluence expected where they are located, see figure 1.2. The cell sizes are adjusted so as to limit the cell capacitance to about 60 pF. Table 1.2 shows the regions of the EE and FH where the different active thicknesses are used, together with the maximum neutron fluence expected after  $3000 fb^{-1}$ , the cell sizes, and the expected signal-to-noise ratio (SNR) for a MIP before and after  $3000 fb^{-1}$ . The regions are specified by the radius (R) measured from the beam axis.

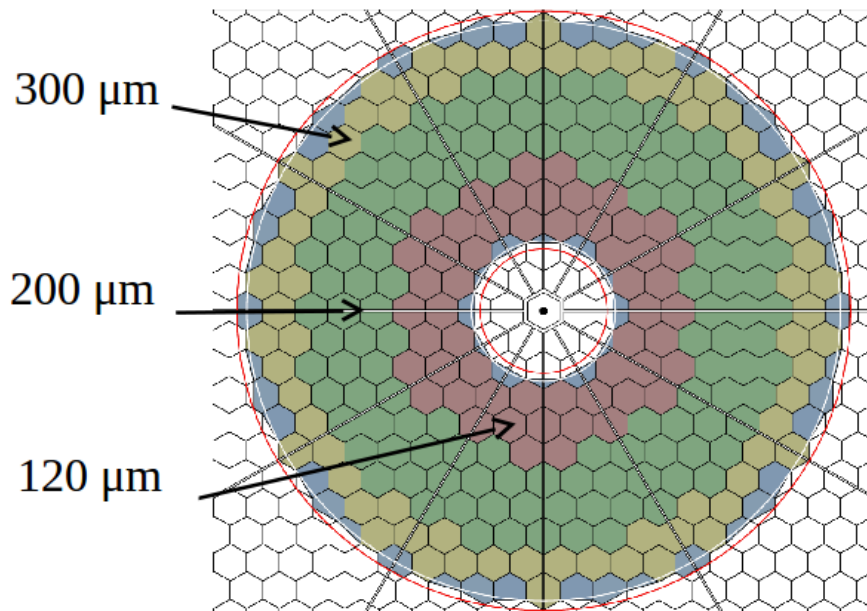


Figure 1.4: Location of the different sensors according to their active thickness. Thinner sensors are located in the innermost part of the calorimeter where the expected neutron fluence is higher [15].

To allow production on high-volume commercial lines the physical thickness of the silicon wafers will be 320  $\mu\text{m}$ . There is not yet a preferred sensor type although, the type chosen

Thickness	300 $\mu\text{m}$	200 $\mu\text{m}$	100 $\mu\text{m}$
Maximum dose (Mrad)	3	20	100
Maximum n fluence ( $\text{cm}^{-2}$ )	$6 \times 10^{14}$	$2.5 \times 10^{15}$	$1 \times 10^{16}$
EE region	$R > 120 \text{ cm}$	$120 > R > 75 \text{ cm}$	$R < 75 \text{ cm}$
FH & BH region	$R > 100 \text{ cm}$	$100 > R > 60 \text{ cm}$	$R < 60 \text{ cm}$
Si wafer area ( $\text{m}^2$ )	290	203	96
Cell size ( $\text{cm}^2$ )	1.05	1.05	0.53
Cell capacitance (pF)	40	60	60

Table 1.2: Silicon sensor arrangement: thickness of active silicon layer in the EE and FH & BH, with the associated cell size and capacitance.

by the tracker was n-on-p for its more radiation tolerance. The sensors and the cells will be hexagonally shaped, so as to make best use of the wafer surface, while providing a geometry that can be tilted. Sensors will be fabricated on 6" or 8" production lines, and a full size hexagonal sensor will cover an area about  $137 \text{ cm}^2$  in the first case.

The front-end readout chips are 70-channels wide, and include for each channel an amplifier, a 40 MHz low-power ADC and a TDC for signal digitization, as well as logic for digital data handling. The 70 channels comprise 63 standard cells, plus a further cell subdivided into seven small calibration pads. There will be either 4 or 8 front-end chips on a module, according to the number of readout channels. A large area multi-layer PCB covering most of the sensor surface will route signals from the sensor to the front-end chips. The connections to the cells on the sensor will be made with wire bonds, through suitable openings in the PCB, while the front-end chip will probably be flip-chip bonded to the PCB.

For the front-end electronics the baseline design uses a preamplifier and shaper DC-coupled to the sensors, and a time over threshold (ToT) measurements with a TCD for digitization of large signals. The ToT front-end has fast shaping with a peaking time of 15 ns after the first shaping stage and 20 ns after the second stage. The gain is around 25 mV/fC and is linear up to 100 fC, which approximately corresponds to the largest signal in the cells. A 10-bit ADC is used for measurement of small pulses, and saturates for pulses of  $\geq 100 \text{ fC}$ .

The jitter of the start time for a ToT measurements is found in simulation of the ToT front-end circuit to have an RMS value of 50 ps. Thus the ToT architecture potentially provides a high precision time measurement for each and every cell with an energy deposit larger than about 80 fC. Precision timing of showers is a very attractive possibility, with potential to

assist in the removal of pileup and the location of interaction vertices, and its realization is being actively studied.

## 1.2 Low-material Long-ladder tracker systems for lepton colliders

Lepton colliders experiments have historically provided a complementary approach for discovering new physics to the hadron collider experiments. The *cleaner* experimental conditions with a relatively reduced background and detector occupancies allow for a more precise event reconstruction. With respect to the tracking detectors, the new generation of leptonic experiments is aiming to fully suppress the need of active colling systems profiting from the envision power pulsing operation mode. Along this line, very reduced material budget and low power dissipation tracking systems are the main RD endeavour to increase the tracking performance by reducing the effect of the material-driven multiple scattering.

On way to achieve the low material budget requirements is the design of microstrip-based tracker systems with a limited number of sensing layers and a long-ladder concept consisting of long microstrip single-sided sensors and a minimal number of readout channels to avoid as much as possible the power dissipation and material. One drawback of this approach could be the limited number of hits available to carry out the pattern recognition needed to reconstruct the particle's trajectory. To mitigate such limitation being able to provide a true 3D tracking by determining the particle's hit position along the microstrip direction could be critical. To cope with this challenge, the use of the charge-division method in long microstrip sensors, with a length of several tens of centimeters, was proposed as a possible tracking technology for the International Linear Collider detector concepts a few years ago [16]; More recently, the concept was demonstrated [17, 18, 19],

Resistive charge division has been used extensively for many years to extract longitudinal position information from electronic sensors. If electronic charge or current is read out from two opposing ends of the sensor, and the impedance of the read-out circuitry is small compared to the resistance of the sensor, it is possible to measure the position of a localized deposition of charge within the sensor by comparing the relative amplitudes of the signals amplified by the two opposing read-out circuits. The mean occupancy rates in the charged-particle tracking systems of proposed leptonic detectors are small enough that long

---

shaping-time electronics can be used to read out resistive position-sensing detector elements. In turn, this admits the possibility of using resistive charge division to obtain an estimate of the longitudinal position of charged collision products as they traverse silicon microstrip sensors incorporated in the detectors.





## Chapter 2

# Silicon detectors technology and radiation damage

## 2.1 Overview

Position sensitive silicon detectors are widely used in modern HEP experiments at particle colliders due to their excellent performance. They accomplish all requirements for HEP experiments, giving information about particle tracks, momenta and charge in a very hostile environment in the innermost part of the detectors. They are basically ionization chambers, when particles liberate e-h pairs inside the semiconductor bulk. The average number of e-h pairs generated is the absorbed energy divided by the mean ionisation energy. An electric field is applied between the two electrodes which generates the movement of the charge carriers, inducing a measurable current.

The semiconductor material most widely used in particle detectors is the silicon. It is a material that is easily available from the semiconductor industry and well understood, but is possible to find semiconductor detectors of diamond or germanium. Diamond detectors are expected to offer significant advantages because of their unique characteristics, but at present they are much more expensive and more difficult to manufacture. Germanium detectors are mostly used for gamma spectroscopy in nuclear physics and in x-ray spectroscopy, they present some advantages over the silicon in terms of energy resolution but mayor drawback is that they need to be cooled to liquid nitrogen temperatures to operate to avoid producing too much electrical noise.

---

The advantages of silicon detectors are the low ionization energy (3.6 eV) and the large density material, what means that a high number of created charge carriers are generated per traversed distance: 73 e-h pairs/ $\mu\text{m}$  in silicon for a minimum ionization particle (MIP). For instance, in gas ionisation chambers the ionisation energy is greater than 30 eV. Also, the large mobility of charge carriers in silicon leads to a short charge collection time, less than 10 ns, which implies a fast readout adequate for the bunch crossing of the LHC (25 ns).

Nevertheless, silicon sensors present some disadvantages in the actual experiments. Despite the sensors themselves are thin, they need a high quantity of support material for structural integrity, biasing and cooling. Thus, the whole sensor system results in a rather large material budget.

One of the most important parameter in a detector is the signal-to-noise ratio (SNR). This value should be as large as possible and it should be above one threshold that guarantee the detection of a particle. In silicon detectors, the signal is determined by the thickness of the sensitive detector region and the charge collection efficiency (CCE) of the detector. For minimizing the noise are required a low capacitance and a low reverse current.

The radiation tolerance of silicon sensors is high. Nevertheless, the silicon sensors installed in the actual LHC experiments can not cope with the radiation environment expected in the future HL-LHC. Therefore, the detectors must be upgraded.

The physics lying behind silicon detectors and how a silicon device can be turned into a detecting device will be exposed in the following sections, a more detailed explanation can be found in these references [20, 21].

## **2.2 Physics of silicon detectors**

### **2.2.1 Working principle and doping**

In a solid crystal, the atoms form a lattice structure with the effect that their atomic orbitals begin to overlap. With an increasing number of atoms, the energy levels become increasingly dense, eventually forming a continuous band structure. The band with the highest energy level that is still fully occupied by electrons is called the valence band, the band lowest in energy with free states is referred to as the conduction band. The structure of these bands

alters a material's conductivity and allows the categorisation of materials into conductors, semiconductors and insulators. In semiconductors at low temperatures, the conduction band is not occupied by electrons. The band gap however is significantly smaller than in insulators. Because of this, from certain temperatures onwards, electrons can be excited from the valence band to the conduction band. The conductivity of a semiconductor is therefore dependent on its temperature. Intrinsic silicon follows the general behaviour of a semiconductor, acting as an insulator at low temperatures and showing conducting properties at higher temperatures. Both bands are separated by the band gap, which is 1.12 eV, as stated above.

By adding artificial impurities to the silicon crystal (doping), additional states in the band gap can be created, altering the electrical conductivity. By adding elements from the third group in the periodic table of elements (e.g. boron) to the group-IV silicon, p-type material is created. Likewise, by adding group-V elements such as phosphorus, n-type material is produced. In both cases, a silicon atom is replaced by an impurity atom. Due to the different valence electron configuration of these impurity atoms, additional free charge carriers are introduced.

To utilise silicon as a detector material, it must be sensitive to the amount of charge carriers in a signal. These charge carriers are created by means of ionisation by a traversing particle, and can amount to only about  $10^3$  charge carriers. In intrinsic silicon, however, the amount of free charge carriers is of the order of about  $10^9$ . Therefore, the amount of free charge carriers in a silicon sensor has to be reduced vastly. This process is called depletion and is achieved by application of reverse bias voltage to a so-called pn-junction.

### **2.2.2 The pn-junction**

One of the most important electronic structures is the pn-junction. Created by bringing together two extrinsic semiconductors of opposite doping, it works as a diode, conducting current basically in one direction. Starting with the separated n-doped and p-doped regions in thermal equilibrium. Bringing the two regions together, electrons will diffuse from the n-doped region to the p-doped region and recombine, while the holes from the p-doped region will do the same vice versa. The surplus of ionized donors and acceptors creates an electric field that counteracts the diffusion. The resulting region is called space charge region (SCR) and is practically free of charge carriers. In figure 2.1 an schematic of the pn-junction with space charge density profile and electric field is shown.

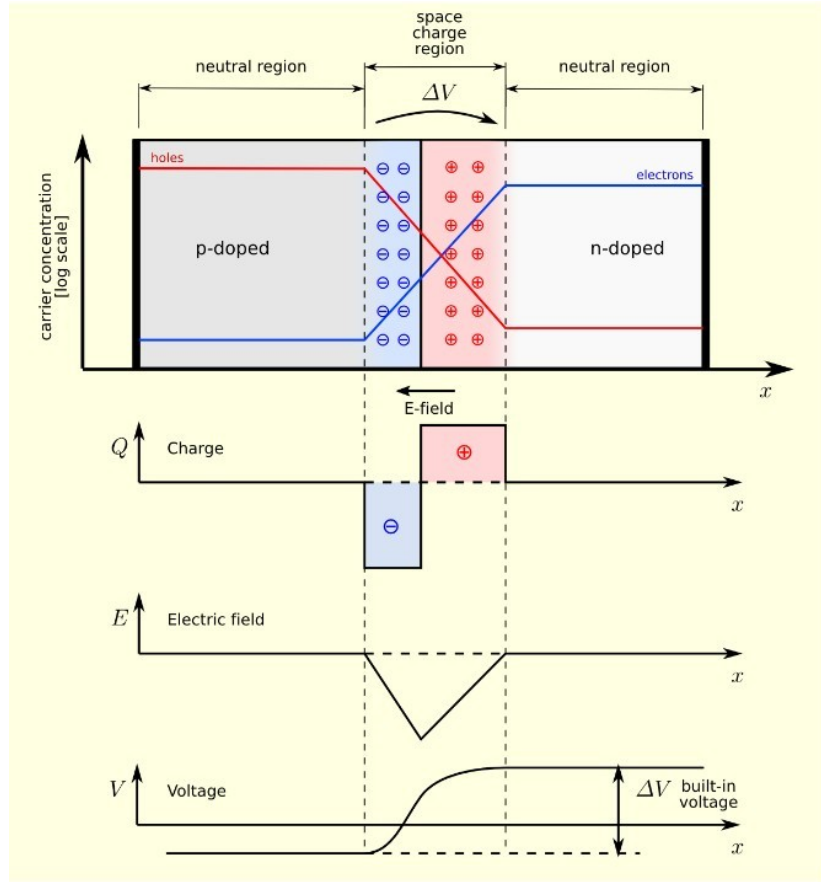


Figure 2.1: An schematic of the pn-junction in thermal equilibrium with zero-bias voltage applied. Included space charge density profile and electric field [22].

The width of the depleted region free of charge carriers, can be modified by applying an external bias having the same polarity as the built-in potential. The relationship between the thickness of the depletion region ( $W$ ) and the applied bias can be found to be:

$$W \approx \sqrt{\frac{2\epsilon_{Si}\epsilon_0(V_{bias} + V_0)}{N_{eff}}} \quad (2.1)$$

where  $V_0$  is the built-in junction potential and  $V_{bias}$  the externally applied bias,  $\epsilon_{Si}$  and  $\epsilon_0$  the dielectric permittivity of silicon and vacuum respectively and  $N_{eff}$  the effective doping concentration. The depletion region extends on both sides of the junction.

When considering a planar junction, this will expose a capacitance between the edges of the depletion region. The capacitance can be calculated by the standard formula for a planar

capacitor, taking into account the dielectric permittivity of silicon ( $\epsilon_{Si} = 11.8$ ):

$$C = \epsilon_{Si} \epsilon_0 \frac{A}{W} \quad (2.2)$$

Where  $A$  is the area of the electrodes and  $W$  is the distance between them (thickness of the depletion region). Measuring the capacitance as a function of the bias thus allows to determine, once known the geometrical dimensions of the detector, the concentration  $N_{eff}$  in the silicon bulk.

The current-voltage characteristics can be derived from the minority carrier concentration at the edge of the neutral region. As the minority carrier diffusion current is proportional to the deviation from thermal equilibrium, the current can be expressed as:

$$J = (J_{Sn} + J_{Sp}) \left( e^{\frac{qV_{bias}}{k_B T}} - 1 \right) = J_S \left( e^{\frac{qV_{bias}}{k_B T}} - 1 \right) \quad (2.3)$$

and  $J_S$  is the total reverse bias saturation current:

$$J_S = q \left( \frac{n_{p0} D_n}{\sqrt{D_n \tau_n}} + \frac{p_{n0} D_p}{\sqrt{D_p \tau_p}} \right) \quad (2.4)$$

where  $\tau_{n(p)}$  is the charge carrier lifetime,  $D_{n(p)}$  is the diffusion constant and  $n_{p0}$  ( $p_{n0}$ ) is the electron or hole density at the edge of the neutral p or n region at thermal equilibrium. For reverse biased diodes with  $n \cdot p \ll n_i^2$  the thermal generation dominates and the volume current is given by:

$$J_V \approx -q \frac{n_i}{\tau_g} W \quad (2.5)$$

Where  $\tau_g$  is the generation life time.

---

## 2.3 Signal formation in silicon detectors

### 2.3.1 Ramo's Theorem

To understand the signal formation in semiconductor detectors it is needed to have a look into Ramo's Theorem already formulated in 1939 [23]. The theorem is summarized in equation 2.6, where  $i$  is the induced current in a given electrode due to a single electron's motion,  $r(t)$  is its instantaneous position at time  $t$ ,  $e$  is the charge of the electron,  $v$  is the instantaneous velocity and the weighting field  $E_w$  is the electric field component in the  $v$ -direction. This  $E_w$  is the electric field that would exist at the electron position when the electron is removed and the electrode is set to one volt potential and all other conductors are grounded.

$$i(r(t)) = E_w(r(t)) \cdot e \cdot v(t) \quad (2.6)$$

In a silicon detector, carriers are holes and electrons, therefore equation 2.6 can be applied also to holes. The differences are in the charge sign and in the velocity, because the mobility of the carrier depends on its nature, given by equation 2.7:

$$v_{e,h} = \mu_{e,h} \cdot E \quad (2.7)$$

Electrons and holes have different mobilities (approximately  $\mu_e \simeq 3\mu_h$ ). A higher mobility can be an advantage in irradiated samples, one of the reasons why trends in silicon detectors are pointing to collect electrons instead of holes.

### 2.3.2 Signal formation

The detection mechanism in silicon detectors starts when an ionizing particle produces free electrons and holes, see figure 2.2. The number of charge carriers generated in the detector material is proportional to the energy release in the semiconductor material which is arranged between two electrodes. Thereby, a number of electrons are transferred from the valence band to the conduction band, and an equal number of holes are created in the valence band. Then, once the electron and holes are generated, they travel to the electrodes in opposite direction

under the influence of an electric field. The resultant current pulse can be measured in an outer electronic circuit, as described by the Ramo's theorem (equation 2.6).

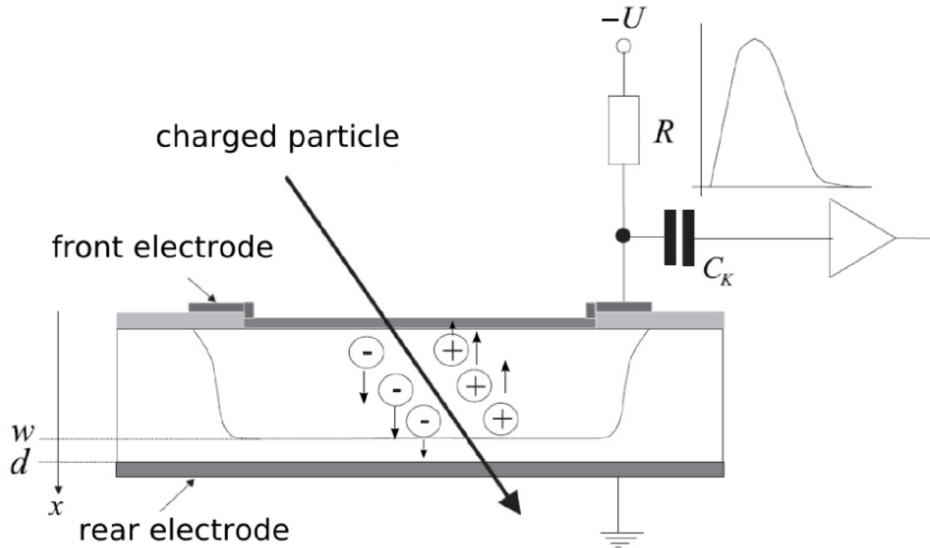


Figure 2.2: Principle of a semiconductor detector [24].

The average energy needed for producing one electron-hole pair in silicon is 3.6 eV. A MIP will produce a most probable value of 73 e-h pairs per  $\mu\text{m}$  of silicon. For a standard sensor of  $300 \mu\text{m}$  the average production of e-h pairs is about 21.900 which results in about 79.000 eV.

The conduction band is only empty at 0 K. Thermal excitation can promote electrons across the bandgap into the conduction band. In pure silicon the carrier concentration is about  $10^{10} \text{ cm}^{-3}$  at 300 K corresponding to a resistivity  $\rho \approx 400 \text{ K}\Omega\text{cm}$ .

## 2.4 Silicon crystal production methods

Silicon is the eighth most common element in the universe, but very rarely occurs as the pure free element in the Earth's crust. It is most widely distributed in dusts, sands, planetoids, and planets as various forms of silicon dioxide. Over 90 % of the Earth's crust is composed of silicate minerals, making silicon the second most abundant element in the Earth's crust after oxygen [25]. Silicon is found in countless compounds in nature and industry. Most importantly and known application is in the electronic technology, where silicon is the principle

---

platform for semiconductor devices. The most advanced semiconductor technologies require monocrystalline silicon with precise uniform chemical characteristics, for instance controlled dopant and oxygen content. This is the silicon eventually used for semiconductors, but it must be further purified to bring impurities below the parts-per-billion level.

As mentioned before, for detector application monocrystalline silicon is needed. Several processes are available for growing monocrystalline silicon, the most widely used being Float Zone, Czochralski and Epitaxial. Following those techniques are summarized.

### **2.4.1 Czochralski process**

This process (Cz) is based on the work of J.Czochralski that in 1918 developed a liquid-solid mono-component grow technique used to grow most of the crystals from which silicon wafers are produced [26]. The most important application may be the growth of large cylindrical ingots of single crystal silicon used in the electronics industry to make semiconductor devices.

First step is the preparation of high purity molten silicon that is introduced in rotating quartz crucible. Dopant can be added at this point in the wanted quantity. Then, a small piece of single crystal material known as seed crystal is dipped into the saturated molten silicon solution. Seed crystal is the equipment used to grow a large crystal of the same material. The seed crystal is extracted from the molten silicon pool pulling it upwards and rotating it at the same time. In this process the temperature gradient, pulling rate and the rotation speed influence the size of the single crystal. The drawback of the Czochralski method is the high amount of impurities, especially O, C, P, B and Al. The technique is summarized in figure 2.3.

In the magnetic Czochralski technique (MCz), a constant magnetic field is applied to the crucible. Thus, it is possible to control the impurity flow inside the melt, which allows to reduce the concentration of oxygen in the silicon crystal and provide a much better homogeneity of the impurity content.

### **2.4.2 Float Zone process**

This silicon crystal growth process was developed by Henry Theuerer in 1955. Float zone (FZ) silicon is very pure silicon that is obtained by vertical zone melting and is a high purity

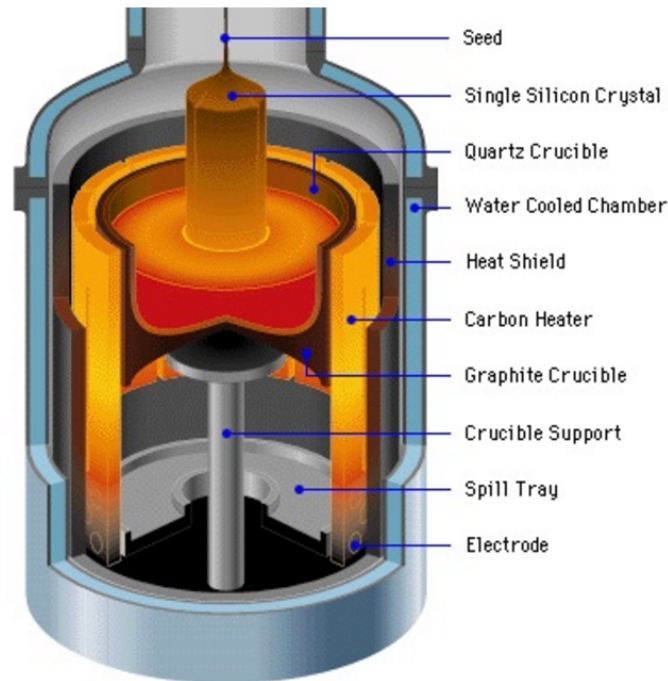


Figure 2.3: Schematic representation of the Czochralski process [27].

alternative to the Cz process. The impurity concentration is very low. Carbon and oxygen stay into the molten region rather than be incorporate into the solidified region. Therefore FZ silicon can easily achieve much higher purity and higher resistivity.

The FZ process is summarized in figure 2.4. The process starts with a high purity polycrystalline pole and a monocrystalline seed crystal. They are held face to face in a vertical position and are rotated. Both are partially melted with a radio frequency field. The seed is brought up from below to make contact with the drop of melt formed at the tip of the polysilicon rod. As the molten zone is moved along the polysilicon rod, the molten silicon solidifies into a single crystal and, at the same time, the material is purified. FZ crystals are doped by adding the doping gas phosphine ( $\text{PH}_3$ ) or diborane ( $\text{B}_2\text{H}_6$ ) to the inert gas for n- and p-type, respectively. The production usually takes place in an inert gaseous atmosphere.

- **Deep diffusion process**

Diffusion is the process whereby a particle moves from regions of higher concentrations to regions of lower concentration. One method to inactivate part of the wafer is to introduce a high number of dopants on it using this process. This process is called "deep diffusion". The deep diffused materials are originally oxygen lean floating-zone

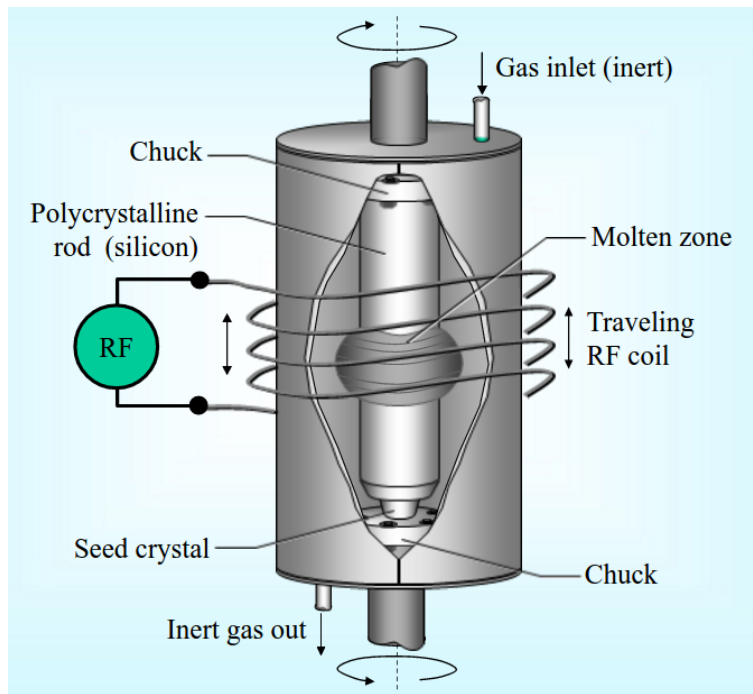


Figure 2.4: Schematic representation of the float zone crystal growth [27].

materials, cut in thick wafers. Since it can be beneficial to have thin active sensors, a part of the sensor is made inactive by introducing a high doping from the backside. A few micrometers of diffusion in the wafer can be made by using implantation techniques and a subsequent annealing to increase a few micrometers more the diffusion thickness. But several tens of micrometers of diffusion thickness can not be made using implantation techniques, and this has to be done with diffusion ovens. This is performed at very high temperatures (900-1200 °C) and for several days, depending on the targeted remaining active thickness. The silicon wafer is placed in an atmosphere containing the impurity or dopants to incorporate. At these high temperatures, the impurity atoms can move into the crystal and diffusion can therefore occur, as schematically illustrated in figure 2.5 (left) [28]. The resulting rise of conductivity towards the back side is not as steep as for materials with standard backside implantations, as it can be seen in figure 2.5 (right) [29].

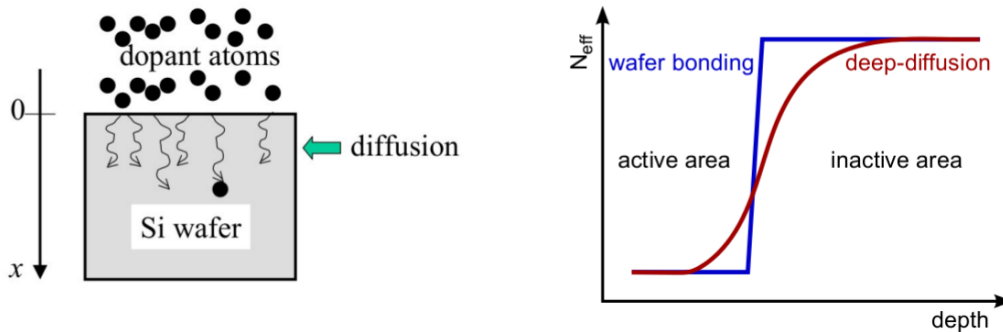


Figure 2.5: Diffusion of dopants in a silicon wafer (left) [28]. Schematic of the doping profile of a deep diffused silicon wafer (right) [29].

### 2.4.3 Epitaxial process

Epitaxy makes reference to the deposition of a mono-crystalline overlayer on a crystalline substrate used as a seed crystal. The epitaxial layer adopts the crystal orientation of the substrate and is therefore also monocrystalline.

There are different epitaxial growing methods, but the most relevant with respect to detector grade Si is the vapour phase epitaxy (VPE), sometimes also called chemical vapour deposition (CVD). In this case a carrier wafer of very low resistivity (Czochralski silicon) is required, which will act as a thick ohmic contact. Silicon is evaporated in a vacuum chamber, along with dopants in predefined quantities. The vapours will condense on the substrate, keeping the orientation of the carrier crystal. The oxygen concentration in the Epi-layer is highly inhomogeneous due to the out-diffusion from the substrate with a high oxygen concentration. Oxygen concentration will be characterized by a gradient, with higher concentrations in the region next to the carrier wafer.

This process provides the possibility to grow substrates with an extremely thin active region. This can be used for obtaining detectors with high fields even at low applied voltage. The material itself is of high purity.

---

## 2.5 Radiation damage

Silicon detectors are widely present in HEP experiments usually located in the tracking systems but also extended to the calorimeter systems like the HGCal in the CMS experiment. The amount of ionizing radiation generated with the collisions depends linearly on the luminosity, which will reach levels of  $10^{16} n_{eq}/cm^2$  in the innermost layer of the detector. In this section, an overview of the radiation damage in silicon and its effects on the macroscopic properties is presented.

### 2.5.1 The NIEL hypothesis

The concentration and nature of crystalline defects inside the detector bulk is given by the purity of the silicon wafer and its processing technique. Crystalline defects introduce new energy levels in the silicon band structure changing the electrical characteristics of the bulk. For example, a level located very deep in the bandgap can act as a generation centre for e-h pairs, resulting in an increase in the reverse current.

A Frenkel Pair is a type of point defect in crystalline lattice wherein an atom is displaced from its lattice position to an interstitial site. It occurs when an inelastic collision between a highly energetic particle and one of the lattice atoms takes place. A vacancy at the original site and an interstitial silicon atom are created. The first collision between the radiation and the atom is called Primary Knock on Atom (PKA). In silicon the minimum amount of energy necessary to generate displacement is about 25 eV.

The radiation damage produced by different particles with different energies can be scaled under the assumption of the so-called Non Ionizing Energy Loss (NIEL) hypothesis. This model can predict the variation in some macroscopic silicon properties after the radiation damage.

The NIEL hypothesis is based in the assumption of a proportionality between the Non-ionizing Energy loss by the particle within the sensor and the amount of displacement damage produced in the silicon. Thus, the radiation damage on silicon will depend on the type of particle and its energy. Slow charge hadrons will lose part of their energy by ionization but they will not have enough energy to create large clusters in the silicon, but fast charged hadrons will have enough energy to create Frenkel pairs and large cluster in the silicon. On

the other hand, neutral hadrons can only interact by inelastic collisions with the lattice atoms. A simulation of these three process was made by M.Huthinen [30], which results can be seen in figure 2.6

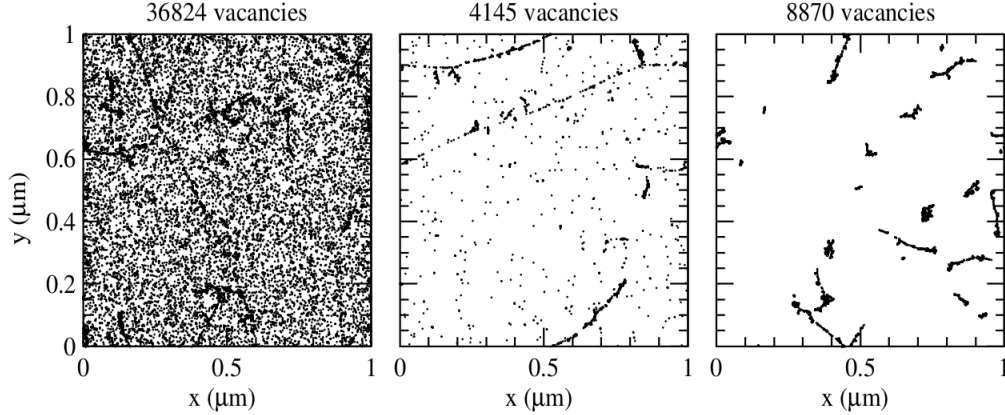


Figure 2.6: Initial distributions of vacancies by 10 MeV protons (left), 24 GeV/c protons (middle) and 1 MeV neutrons (right). The plots are projections over 1  $\mu\text{m}$  of depth ( $z$ ) and correspond to a fluence of  $10^{14}\text{cm}^{-2}$ . Source: [30]

According to the NIEL hypothesis each collision happening at the energy  $E$  (energy of the particle) will have a probability  $f_v(E, E_R)$  to produce a kicked-out atom with a recoil energy  $E_R$ . The index  $v$  indicates all possible interaction between the incoming particle with energy  $E$  and the silicon atoms in the crystal leading to displacements in the lattice. The probability of this atom of producing more dislocated atoms can be weighted using a Lindhard partition function  $P(E_R)$  [31]. Considering all the cross section  $\sigma_v(E)$  of all the possible non-ionizing interaction for the all the particles with an energy  $E$ , it is possible to calculate the NIEL and is expressed by the displacement damage cross section  $D(E)$  (also called damage function), see equation 2.8.

$$D(E) = \sum_v \sigma_v \int_0^{E_R^{max}} f_v(E, E_R) P(E_R) dE_R \quad (2.8)$$

This displacement damage cross section is rescaled to a reference value, which is the one produced by a mono-energetic beam of 1 MeV neutrons. Thus, it is possible to define a proportionality constant called hardness factor ( $k$ ), see equation 2.9, where  $\phi(E)$  is the fluence, in particles/ $\text{cm}^2$ , considered with an energy  $E$ .

---


$$k = \frac{\int D(E)\phi(E)dE}{D(E_n = 1MeV) \int \phi(E)dE} \quad (2.9)$$

With this hardness factor, any fluence  $\Phi$  of a particular kind of particle can be rescaled to the fluence of 1 MeV neutrons  $\Phi_{eq}$  producing the same displacement damage. The equivalent 1 MeV neutron fluence  $\Phi_{eq}$  can be calculated by equation 2.10.

$$\Phi_{eq} = k\Phi = \int \phi(E)dE \quad (2.10)$$

The NIEL hypothesis represents a good approximation in the case of primary damage production. This hypothesis is based on the assumption that the detector damage scales with the cumulated energy transferred to displacement in silicon. It does neither take into account annealing effects nor if the displacements are occurring in form of single displacement or in form of cluster displacement.

## 2.5.2 Annealing

The defect annealing has a very strong dependency with the temperature, as many defects are mobile, temperature plays an important role. But not only the primary defects evolve, the secondary defects are mobile as well so they can migrate and from other complex defects or dissociate. The processes that can happen during the annealing can be divided in three types:

- Complex formation, in which the defect migrates to a different site in the lattice by collecting enough energy to break the potential barrier that keeps it in its physical place. This happens usually by thermal excitation.
- Dissociation, when a defect complex consisting of more than one component is dissociated into its single components.
- Migration, when defects become mobile and migrate through the Si lattice until they are trapped by sinks. This process strongly depends on the temperature.

For annealing processes, the probability of having an interaction is given by the balance equation 2.11. Where  $N_x$  is the concentration of defects of type X and k the rate constant for the process.

$$-\frac{dN_x}{dt} = kN_x \quad (2.11)$$

The rate constant of this processes is temperature dependant and it follows the Arrhenius relation, equation 2.12. Where  $E_A$  is the activation energy for the process that takes place,  $k_B$  the Boltzmann constant and T the absolute temperature.

$$k = k_0 \exp\left(-\frac{E_A}{k_B T}\right) \quad (2.12)$$

It is important to perform annealing studies because the annealing behaviour of the defects can provide more information than given by the electrical characterization, that can help in the identification of the nature of a defect. The time constant of the annealing process can take years after irradiation, and still changes can occur at that point.

### 2.5.3 Trapping

Crystalline defects introduce localized energy levels into the bulk with a high capture cross section, which implies that if those levels are located far from the two bands, it will slow down the re-emission times, in the order of ms. Then, if part of the travelling charge gets trapped by these crystalline defects, it will not be able to be measured as usual signal integration times expected in HEP experiments are much faster, in the order of tens of nanoseconds.

The life time of the carriers is directly related to the purity of the crystal. Silicon is characterized by a very low concentration of crystalline defects. But in addition to the original crystalline defects, radiation defects are produced that can generate a much bigger trapping effect within the silicon bulk. In fact trapping is the biggest sources of signal degradation in irradiation silicon detectors after high fluences.

A parametrization of the trapping was proposed in [32]. The inverse of the lifetime is proportional to the NIEL-related bulk damage and fluence, see equation 2.13.

$$\frac{1}{\tau} = \frac{1}{\tau_i} + \phi K \quad (2.13)$$

Where  $\tau_i$  is the intrinsic lifetime of the carriers, what is negligible (about milliseconds)

---

and  $K$  a constant that depends on the carrier nature (electron or hole) and the particle type used for irradiation (e.g. neutral or charged hadrons).

## 2.5.4 Impact on the reverse current

Bulk current in silicon sensors comes from two main contributions: generation current, due to the generation of carriers in the depleted region and diffusion current, due to the diffusion of carriers from the non depleted region. In highly irradiated sensors the dominant contribution is the generation current and even in most of the unirradiated sensor. This generation current depends on the pair generation rate and generation volume.

The defects introduced close to the middle of the bandgap are the main responsible for electron-hole pairs generation and recombination by means of thermal excitation. This will generate free electron-hole pairs in the depleted region of the detector. These defects, as mention before, result macroscopically in an increase in reverse current. Thus, the reverse current increases linearly with particle fluence, this relation between the reverse current and the NIEL energy deposited by radiation follows the equation 2.14.

$$\Delta I = \alpha \Phi_{eq} V \quad (2.14)$$

The proportional factor is called alpha value ( $\alpha$ ), ( $\Delta I$ ) represents the increment of the reverse current measured after irradiation normalized by the volume of the diode ( $V$ ), and ( $\Phi_{eq}$ ) the irradiation fluence ( $\Phi_{eq}$ ). This parameter is strongly temperature dependent and can be rescaled to different temperatures using equation 2.15 [33], where  $E_{eff}$  is the effective energy and  $k_b$  the Boltzmann constant..

$$I(T) \propto T^2 \times \exp\left(-\frac{E_{eff}}{2k_b T}\right) \quad (2.15)$$

In figure 2.7 is shown the fluence dependence of the increase in the reverse current normalize to the volume, the figure was taken form [34] and the alpha value extracted from this plot is normally used as a reference in many works, which value at a given temperature depends on the annealing time at different temperatures as can be seen in figure 2.8. All the measurements were done at room temperature and then they were normalized to 20°C in the plot.

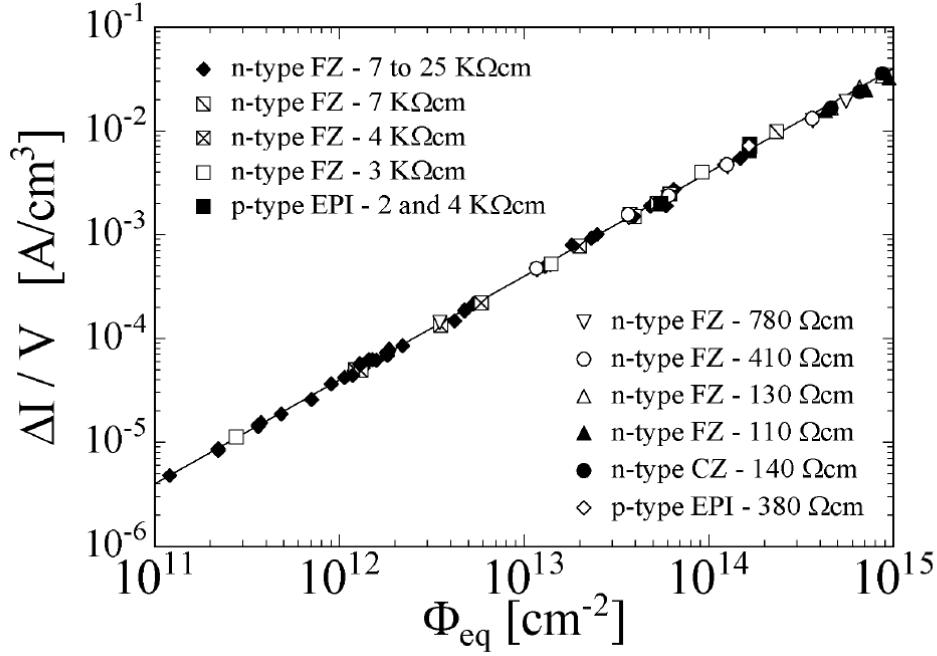


Figure 2.7: Fluence dependence of reverse current for silicon detectors produced by various process technologies from different silicon materials. Measured after an annealing of 80 minutes at 60°C. Alpha value =  $3.99 \pm 0.03 \times 10^{-17}$  A/cm [34].

### 2.5.5 Effects on depletion voltage

The depletion voltage in an unirradiated sensors is proportional to the  $N_{eff}$ . Defects produced by radiation act as a donors or acceptors, with some levels close enough to one of the bands to be fully ionized at room temperature. But, when a detector is biased more deeper defects can change the  $N_{eff}$ . Many of the defects induced by radiation are responsible for a change in the  $N_{eff}$  and hence for a change in the depletion voltage.

There is other effect in silicon due to irradiation that is call donor and acceptor removal, it happens when a dopant is removed from its interstitial position and thereby deactivated. After irradiation, silicon bulk shifts towards a different doping profile. An effect called double-junction can be present in irradiated silicon sensors, due to the activation of the defects in the bulk volume close to the two implants when the detector is biased, creating two separate junctions. Thus, the depletion process in an irradiated silicon sensor implies the contribution of two different space charge regions that merge in one once the sensor is fully depleted. However, one of this two regions can be dominant, and for example in FZ silicon it is known

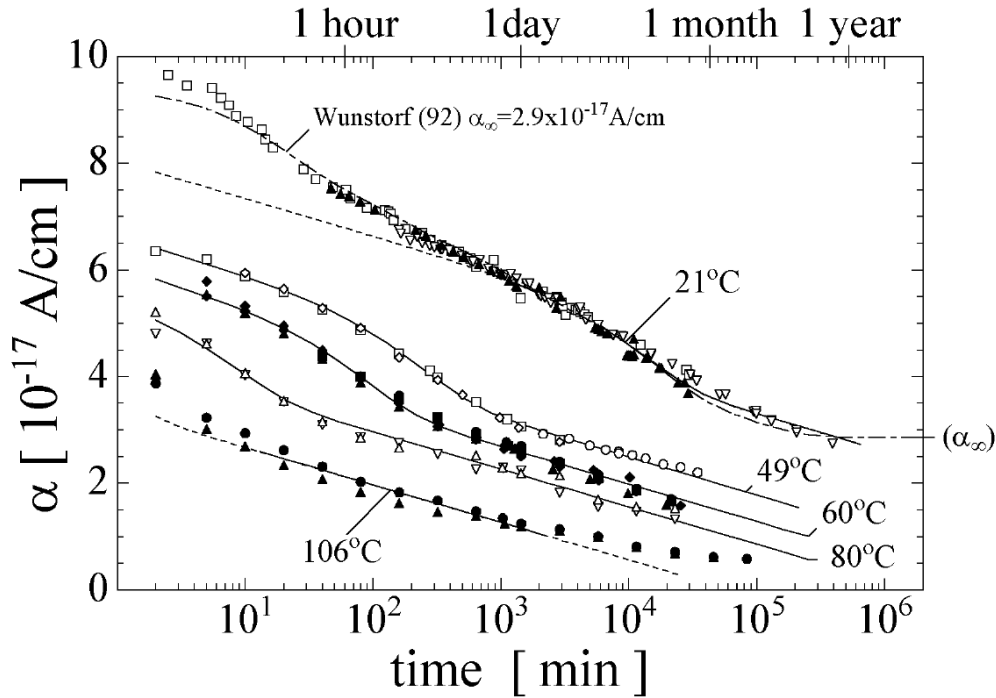


Figure 2.8: Alpha value as a function of the annealing time at different temperatures [34].

to undergo an almost complete space charge sign inversion. A model of this effect was developed by the Hamburg group [35] to describe the sensors evolution with irradiation, it can be seen in figure 2.9.

### 2.5.6 Charge Multiplication

In a very highly irradiated silicon sensors it is observed that the collected charge is higher than expected for the sensor thickness and irradiation doses, in some cases even higher than in unirradiated sensors. This is attributed to an avalanche multiplication process, very similar to the one used in the Avalanche Photo Diodes (APDs), resulting in a charge multiplication in the device. This process can be caused by a very high value of  $N_{eff}$  that causes a very high electric field in a small region which leads to impact ionization and thus compensate the charge lost by irradiation effect. Recent studies have shown this anomalously high collected charge in highly irradiated strip detectors [36, 37] and epitaxial diodes [24].

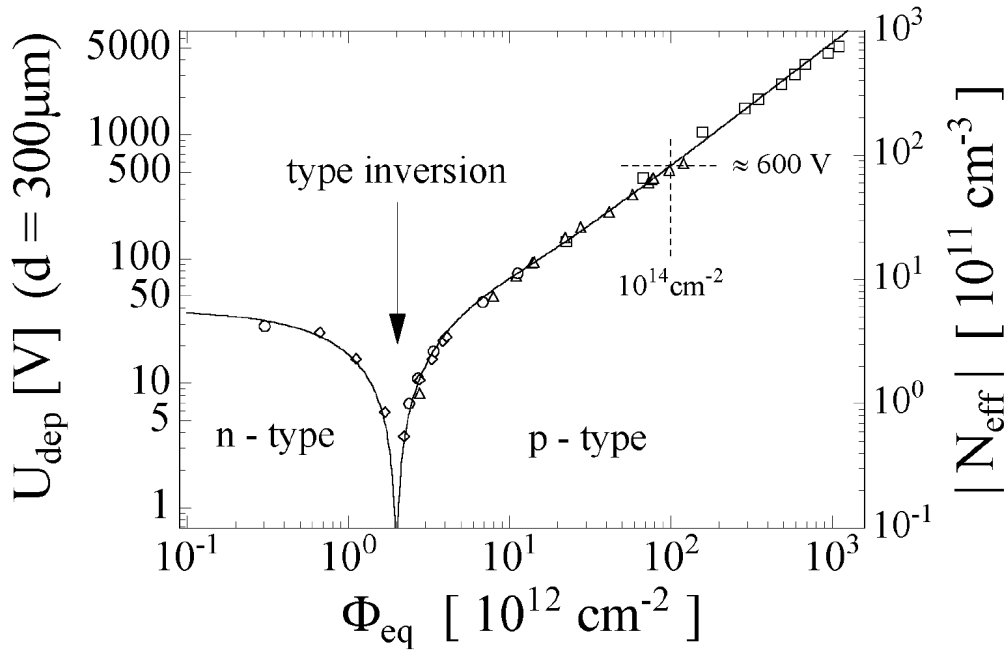


Figure 2.9: Change in the depletion voltage respectively the absolute effective doping concentration as measured immediately after irradiation for standard FZ p-on-n sensor[35].

### 2.5.7 Surface damage

The surface damage in silicon detectors is mostly caused due to the ionization of the oxide, it happens when defects are introduced in the passivation  $SiO_2$  layers of the detector. The main consequence of this is that electrons escape from the oxide but positive ions stay on it creating a positive space charge. A high local electric field can be generated as well causing premature breakdown and avalanche effects.

In order to minimize the impact of oxide damage in n-on-p detectors it is common to use p-stop or p-spray isolations. The p-stop isolation consists in a p-type silicon barrier surrounding the electrodes and the p-spray isolation is made adding an extra p-type layer between the passivation layers and the sensor bulk. The surface damage is more severe in segmented devices like microstrip and pixel detectors but it can be negligible in the non-segmented ones, like diodes.



## Chapter 3

# Experimental methods

In this chapter, the experimental arrangements used for the characterization of the devices under study are described. The different characterizations were done in several places: the Silicon Lab at Instituto de Física de Cantabria (IFCA) in Santander (Spain), the University of Hamburg at DESY campus (Germany) and the Solid State Detector (SSD) lab of the PH-DT group at CERN . Despite of the fact that the set-ups are placed in different facilities and they are slightly different, the techniques used are the same and measurements are compatible.

The characterization techniques used were:

- Electrical characterization. It is needed to determine the electrical properties of the devices, mainly reverse current and capacitance as a function of the voltage. These properties are important for determining the operational parameters for both fresh and irradiated devices and have an impact on the design and integration of the sensors into the full detector system.
- Laser characterization. It is used to measure the charge collected by the devices. A laser with a pulse duration of tens of picoseconds generates excess free carriers in the silicon, mimicking the effect of a ionizing particle.
- Radioactive source characterization. It is another way to measure the charge collected by the devices but in this case inducing charge with  $\beta$ -particles coming from a  $^{90}\text{Sr}$  radioactive source. The signal generated by the  $^{90}\text{Sr}$  in  $300\ \mu\text{m}$  the silicon is similar to the signal created by a minimum ionization particle.

- 
- Test beam characterization. The devices can be tested under more realistic operational condition in a test beam. In particular SPS H4 line at CERN was used for this propose. The devices can be tested with different particles (electrons, muons, pions) at different energies, from a few GeV till a hundreds GeV. Information like charge collection, spacial resolution, signal-to-noise and timing capabilities were studied here.

### **3.1 Electrical characterization: current-voltage and capacitance-voltage**

Electrical properties of the devices need to be measured for quality assurance and for extracting relevant informations from extensive macroscopic quantities. Reverse current as a function of the bias voltage, usually called IV characteristic and capacitance as a function of the bias voltage, usually called CV characteristic, are the two main properties to be measured. In particular, interesting parameters to be extracted from these characterization are: depletion voltage, reverse current at full depletion, capacitance at full depletion and break down voltage. Additionally, the power dissipation can be derived.

For the IV and CV characterization two experimental arrangements were used, one at Hamburg and the other one at CERN. The functionality of both were the same and in this section the set-up at CERN is going to be described in detail.

The main components of the set-up are shown in figure 3.1 and are: chiller, temperature controller, keithley 237 source-meter, Agilent HP E4980A LCR-meter, keithley 2410 source-meter, keithley 6487 picoAmper-meter, cold-chuck, probe holders, needles and microscope.

In addition, not shown in figure 3.1, the following equipment is used: a metallic box for electromagnetic isolation and light tightness, a vacuum pump to fix the detector on the cold-cluck, dry air in order to have very low humidity inside the box and a PC running with a user interface based on LabVIEW. The temperature range of the set-up goes from  $-30^{\circ}\text{C}$  to  $+150^{\circ}\text{C}$ .

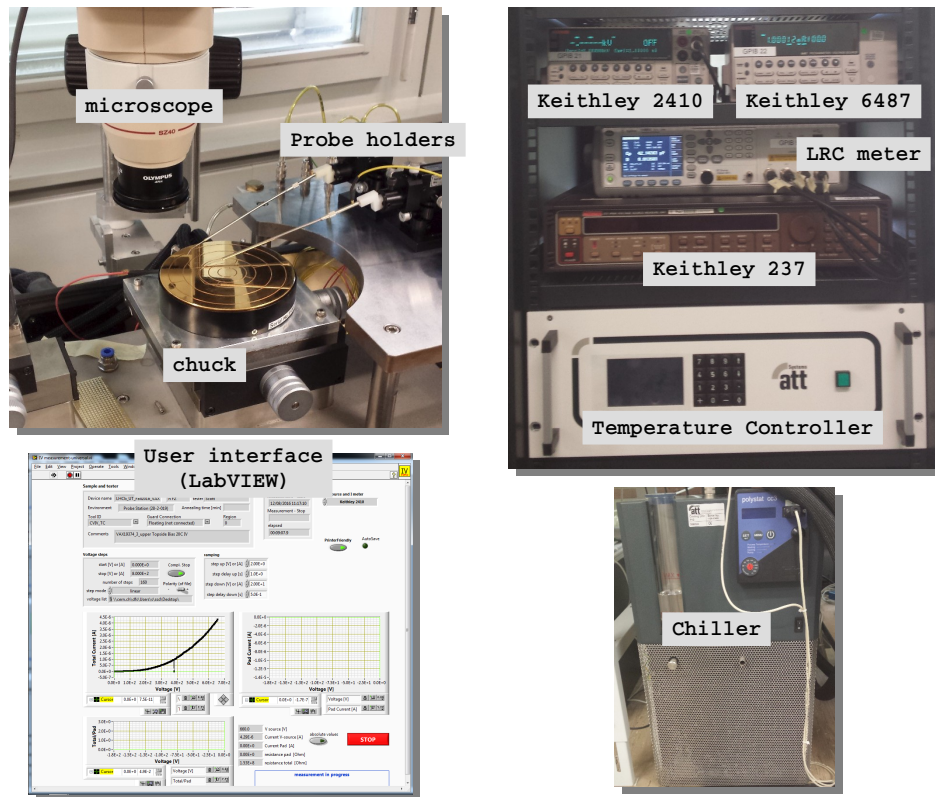


Figure 3.1: Main components of the IV/CV set-up used at CERN for the electrical characterization.

### 3.1.1 Current-Voltage characterization

A schematics of the current-voltage measurements is shown in figure 3.2. The reverse current as a function of the voltage is related to the active or depleted volume of the sensor and the number of minority carriers present in the bulk. The bigger contribution to the current comes from the presence of electron-hole pairs generation centres within the depleted region. These generation centres have energy levels located close to the middle of the bandgap and are able to generate e-h pairs just by thermal excitation. The whole leakage current presents a strong dependence with temperature. Figure 3.3 shows a typical IV curve for an unirradiated silicon diode and its dependence with the temperature can be clearly seen.

For the IV measurements, the sensor is placed on the chuck with two proposes: have a thermal control of the sensor’s temperature and to apply the bias voltage on the backplane of the sensor. The contact with the structures on the front (pad and guard ring) is realized by probe holders ending up with a needle. One of the probe holders is grounded through

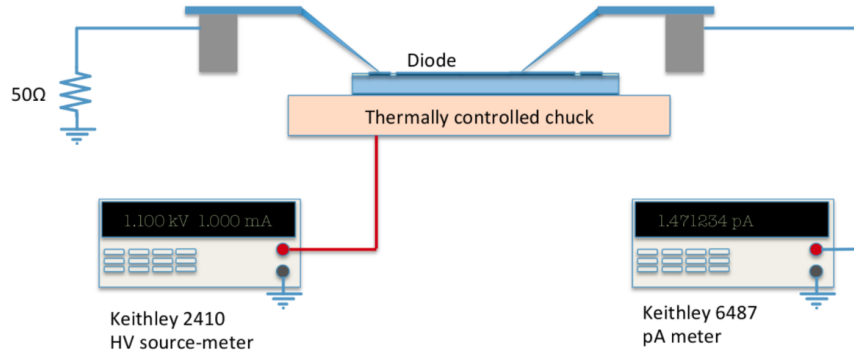


Figure 3.2: Schematic view of the IV set-up used during the measurements for this work [22]. Typically, the keithley 2410 is used to measure the total current while the keithley 6487 is used to measure the pad current (the dominated one).

a Keithley 6487 picoamperometer. The high voltage is applied to the chuck by a Keithley 2410 source measure unit, able to provide a bipolar voltage up to 1100 V and measuring the current with an accuracy of 100 pA at the same time. For the guard ring connection another probe is used directly connected on the common grounding of the two units (HV supply and picoamperometer). The chuck is thermally stabilized by means of thermoelectric elements which are cooled through a liquid circuit connected to a chiller unit. The set-up is mounted in a metallic box that can be tightly closed, dry air is flushed inside the box to avoid condensation problems. The whole system (voltage control, data acquisition, temperature control) is managed through a DAQ system written in LabView.

### 3.1.2 Capacitance-Voltage characterization

A schematics of the capacitance-voltage measurements is shown in figure 3.4. The main electronic test equipment for this characterization is the LCR meter that is used to measure the inductance (L), capacitance (C), and resistance (R) of an electronic component. The LCR meter used for the CV characterization was the HP E4980A from Agilent, able to measure capacitances with an accuracy of 1 femtofarad. The detector is subjected to an AC voltage source, usually a sinusoidally oscillating voltage, with tunable amplitude and period. For these measurements 1 V of amplitude was used. Depending on the complex impedance of the detector, the returning pulse will have a phase and amplitude shift, which will correspond to a real and an imaginary part of the detector's impedance. The meter must assume either

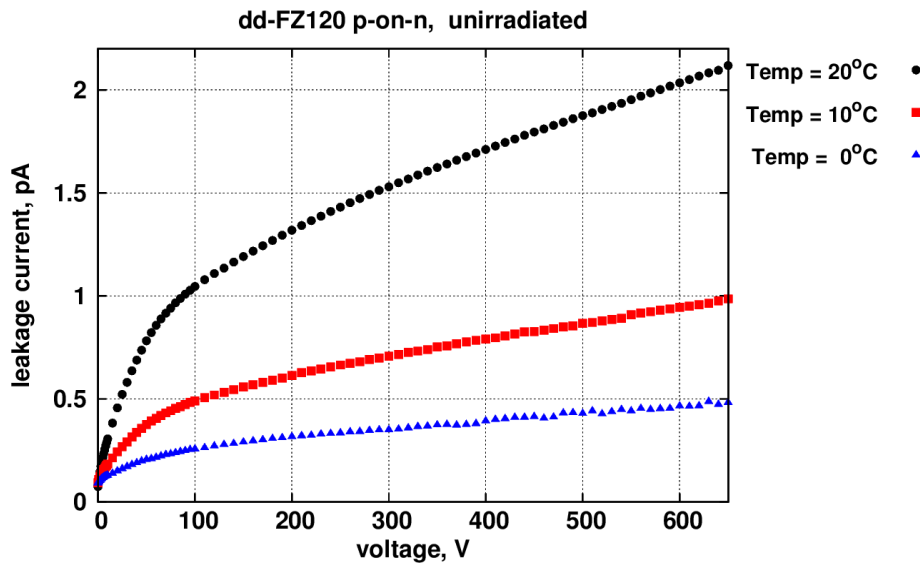


Figure 3.3: Current-voltage characteristic of an unirradiated silicon diode at different temperatures. In this case the IV characteristic of a deep-diffused float zone with a thickness of  $120 \mu\text{m}$  p-on-n is shown.

a parallel or a series model for these two elements. It is up to the user to provide a circuit model to the LCR meter represents best the detector.

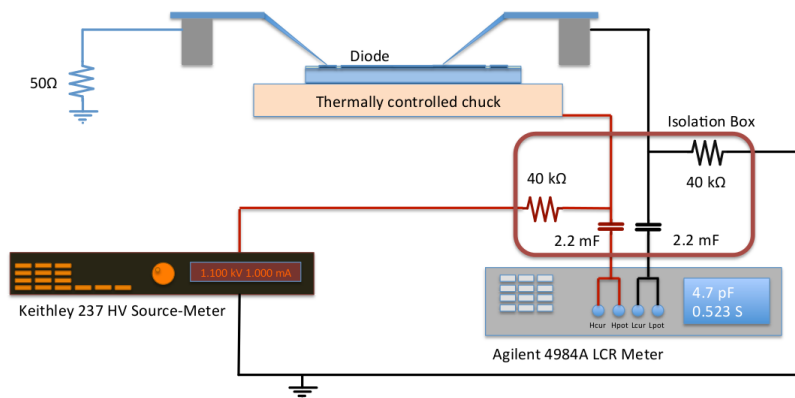


Figure 3.4: Schematic view of the CV set-up used for the measurements presented in this work [22].

Silicon diodes can be described by a capacitor ( $C$ ) in parallel with a resistor ( $R_p$ ) that accounts for the diode's depleted bulk. In addition, there is a serial resistor ( $R_s$ ) which represents the resistance of the undepleted detector bulk. The equivalent circuit of a reverse-biased

diode is shown in figure 3.5.

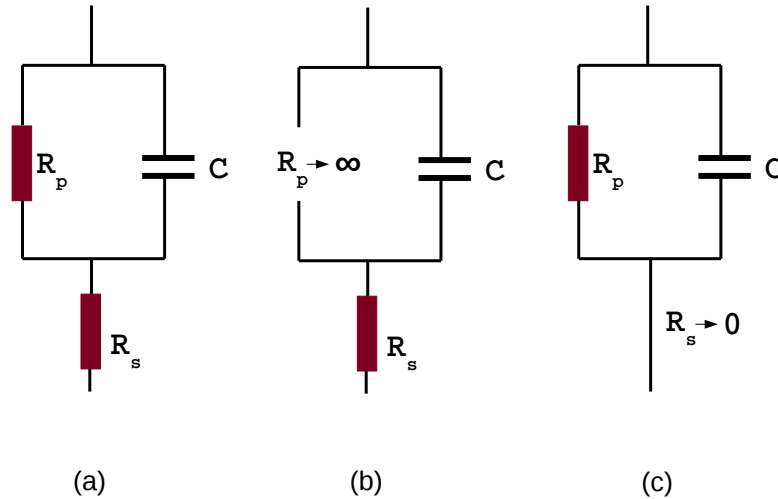


Figure 3.5: Equivalent circuit of a reverse-biased diode (a), serial mode simplification (b) and parallel mode simplification (c)

It is only possible to measure two parameters at once with a capacitance bridge. Therefore, the model has to be simplified. The serial mode simplification does not take into account the parallel resistance  $R_p$ , so the contribution of the depleted bulk region is neglected. The parallel mode simplification does not consider the series resistance  $R_s$ , which means that the contribution of the undepleted bulk region is neglected. Nevertheless, it is possible to convert from one mode to another if necessary.

For an unirradiated sensor both modes are equivalents because the reverse current is not high. Nevertheless, for irradiated sensors this is not valid any more and both resistance,  $R_p$  and  $R_s$ , are needed for a correct description of the sensor since the reverse current becomes relevant and the undepleted region is highly resistive. For low fluences the serial mode is a better approximation, but at high fluences where the reverse current is considerable, the parallel model becomes a better approximation and it was the one chosen for the measurements of this work.

The frequency of the oscillating voltage generated by the LCR meter has no effect on unirradiated detectors up to 100 kHz. However, the defects created by irradiation have emission capture times of microseconds with a strong temperature dependence. In this case frequency and temperature play an important role in the capacitance measurement and they need to be

fixed for further comparisons. A detail study of the effect of the frequency in the capacitance can be found in [38].

Figure 3.6 shows a typical CV curve for one silicon diode before and after neutron irradiation. Plotting the  $1/C^2$  against the bias voltage allows a rectification of the two regions corresponding respectively to the depleting and fully depleted bulk. The depletion voltage is obtained by the interception of two straight lines fitting the CV curve before and after depletion.

At full depletion, the thickness of the diode can be calculated by equation 3.1, where  $\varepsilon_0$  is the vacuum permittivity,  $\varepsilon$  is the silicon relative permittivity, Area is the pad's area, W is the pad's thickness, C is the measured pad's capacitance and V is the applied voltage. In addition, the effective dopant concentration ( $N_{eff}$ ) can be extracted using equation 3.2, where  $q_0$  is the electron's charge and  $V_{FD}$  the full depletion voltage.

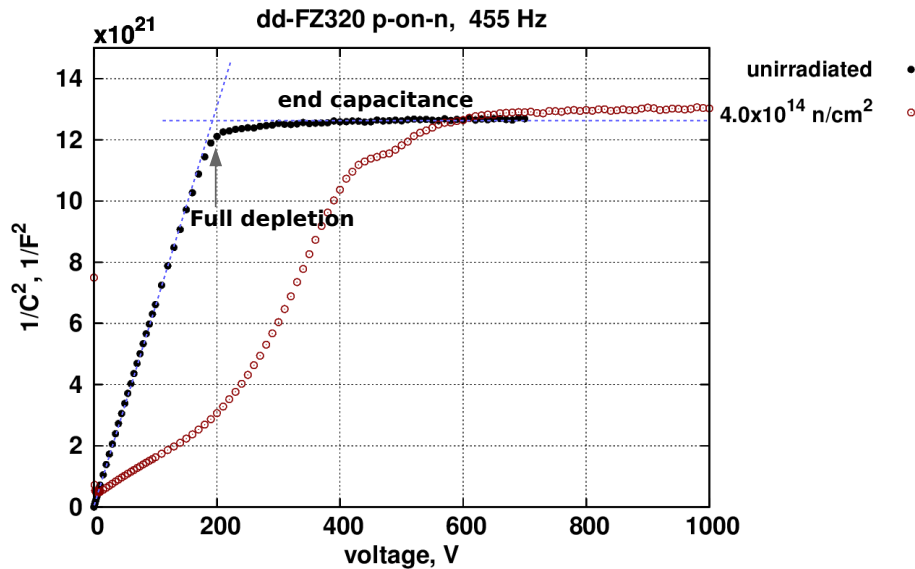


Figure 3.6: Capacitance-voltage characteristic of a silicon diode before and after neutron irradiation.

$$W(V) = \frac{\varepsilon_0 \times \varepsilon \times Area}{C(V)} \quad (3.1)$$

---


$$N_{eff} = \frac{2 \times \varepsilon_0 \times \varepsilon \times V_{FD}}{q_0 \times W (V_{FD})^2} \quad (3.2)$$

## 3.2 Laser characterization: Transient Current Technique

The transient current technique (TCT) is an important tool to study several features in the detectors like: signal formation, charge collection and trapping mechanisms. The basic principle of this technique is to use a laser pulse to generate excess carriers inside the detector, then these carriers will drift towards the respective electrodes under the influence of an applied bias voltage and finally the induced current signal is measured. A more detailed description of this technique can be found here [39].

Time resolved induced current can be calculated using Ramo's theorem [23], see equation 3.3. Where  $\vec{v} = v(\vec{E})$  is the drift velocity,  $\vec{E}$  is the electric field and  $\vec{E}_W$  the so-called weighting field. The electric field determines the charge trajectory and the velocity of the particle.

$$I(t) = -q\vec{v}\vec{E}_W \quad (3.3)$$

The light from a red laser (660 nm) is fully absorbed by the silicon after a few microns. In this case the contribution of one of the two charge carriers created is negligible, and it allows to observe the signal induced by only one type of charge carries, either electrons or holes. On the other hand, the light from an infrared laser (1060 nm) creates charge carriers all along the optical path, so in this case the induced current will have contributions from both charge carries. Figure 3.7 shows the charge carriers generated using different wavelength lasers. With the infrared laser, contributions from both charge carries can be seen in the induced signal. The electrons are around three times faster than the holes and their contributions appears at the beginning of the induced signal as a higher and narrower pulse, while the contribution of the holes appears later as a smaller and wider pulse. This can be observed in figure 3.8 where two TCT pulses with different laser wavelength are compared. In the one taken with infrared laser the contributions from the electrons and holes appear together, while in the one taken with red laser and front illumination, it is possible to observe only the contribution of the electrons (in a p-on-n diode). This is a powerful tool to study the dynamics of the different charge carriers generated inside the detector. Nevertheless, for this work was

only studies on the collected charge were required therefore, only the infrared laser was used.

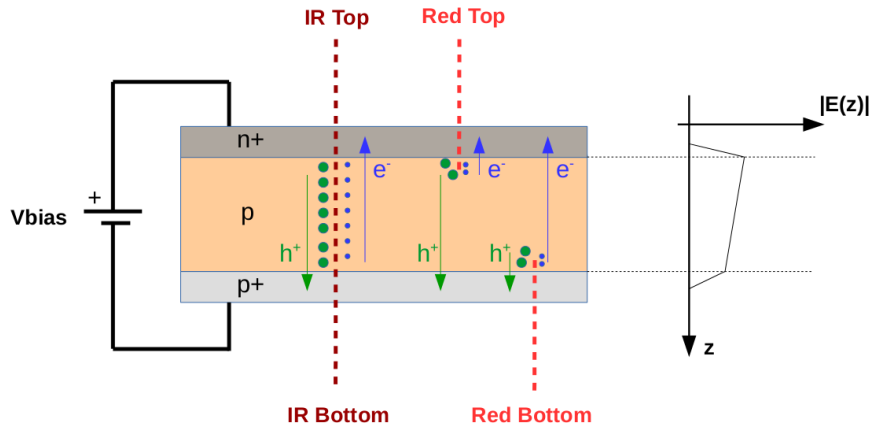


Figure 3.7: Location of the charge carriers generated with the two types of laser sources and light injection sides available in the set-up, IR ( 1064 nm ) and red ( 660 nm ).

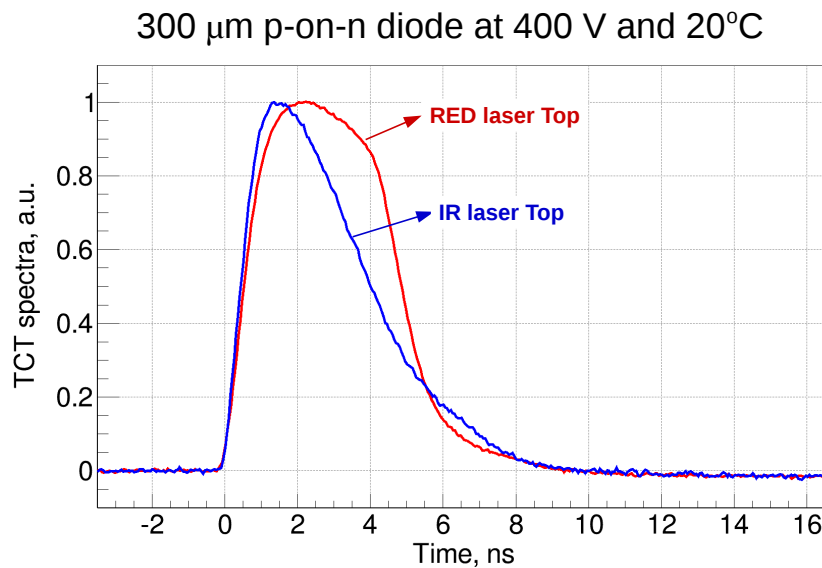


Figure 3.8: Comparison between two TCT pulses taken with IR laser and red laser in a fully depleted diode. The amplitude has been normalized to 1.

A schematic of a TCT set-up is shown in figure 3.9 and the main components of the set-up placed at CERN are shown in figure 3.10. For the measurements the detector is glued on a

pcb, see figure 3.11. Then, the pcb is mounted on a copper plate cooled by peltier element which is refrigerated by a Huber chiller unit working with a ethanol/water solution. A proportional–integral–derivative controller (PID controller) is used to stabilize the temperature using as a reference a PT1000 resistance glued on the PCB close to the sensor. With this system it is possible to reach temperatures down to  $-22^{\circ}\text{C}$  in the detector. A stage system allows movements in three axes. In Z (vertical coordinate), with a repeatability of  $\pm 1 \mu\text{m}$  help with the focus of the lasers and as well for the edge TCT measurements. In X and Y (horizontal coordinates), with a repeatability of  $\pm 1.75 \mu\text{m}$  can be used to perform scans over different regions of the detector.

The detector is inside a Faraday cage, that isolates the most delicate part of the set-up from electromagnetic perturbations coming from the environment, avoid light in the interior and flushing with dry air inside the cage it is possible to avoid condensation problems.

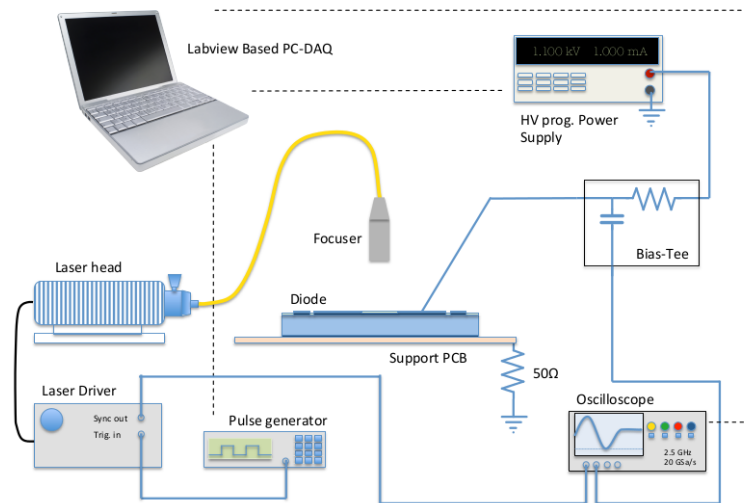


Figure 3.9: A schematic of a TCT set-up [22].

Laser lights are coming through optical fibers inside the Faraday cage. Two sources of laser can be selected, red 660 nm and infrared 1064 nm and their intensity can be manually regulated by means of two attenuators. In both cases, 10% of the light is sent to a reference diode for each laser source in order to measure their intensity. The remaining 90% of the red light is split in two, one for front illumination and the other for back illumination of the device. In the case of the infrared, the remaining 90% of the light is split in two, but in this case 50% is for the edge illumination, and the other 50% is divided again for front and back



Figure 3.10: Pictures of the main systems of the TCT set-up at CERN: optical, cooling, linear stage, electrical and readout.

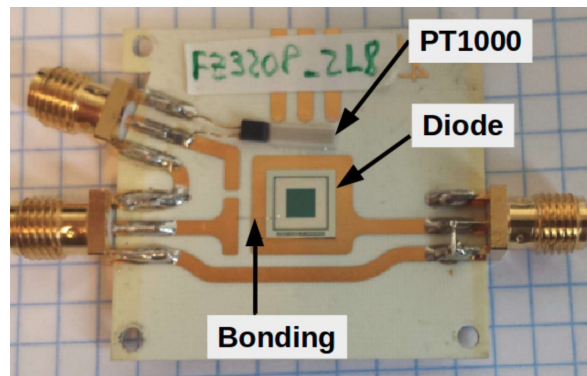


Figure 3.11: Diode glued on a pcb.

illumination of the device. For a better understanding of the optical system, in figure 3.12 can be seen its schematics. The laser controller is able to provide pulses with a duration of 250 ps (FWHM).

For the readout is used an Agilent DSO 9254 oscilloscope, with an analog bandwidth of 2.5 GHz. Two channels are used, one for the readout of the detector and the other one for the readout of the reference diode. Each measurement taken with the set-up represents

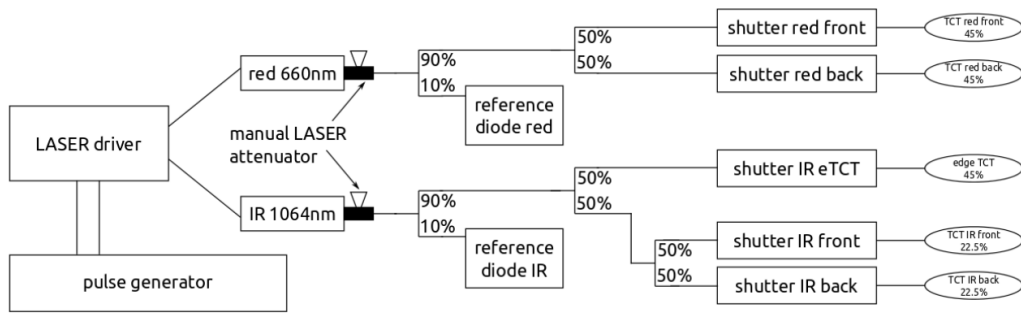


Figure 3.12: Schematic of the optical system in the TCT set-up at CERN.

the average of 256 samples in order to improve the signal-to-noise of the measurement. The diode's back-side is grounded and the front side is biased using a Keithley 2410 source-meter. The TCT signal is amplified by a CIVIDEC C2 broadband amplifier of 2 GHz and 40 dB of amplification [40], which has internally implemented a "bias tee" that provides the necessary decoupling of the signal from the high voltage. A PC running with a user interface based in LabVIEW is used to manage the set-up.

### 3.2.1 Adjustment of the laser intensity

In order to measure the total charge induced for the laser in the sensor the set-up was calibrated using a standard fully depleted reference diode of  $300 \mu\text{m}$  p-on-n, biased at 400 V and measured at  $20^\circ\text{C}$ . Thereby, we will assume that for a given amount of incident light, monitored by a reference diode, a fix amount of carriers are created in the silicon. This assumption implies that the absorption of the light by the silicon does not depend on its irradiation level.

There are two ways of changing the intensity of the laser in the set-up, one by software (usually the intensity is setted at 40% for the Red and 60% for the IR of their total intensity) and the other by means of two manual attenuators, that the user can manipulated according to his intensity requirements. For the calibration, the software intensity was set at the usual value of 60% and then at 95% in both cases to estimate the maximum intensity that can be reached with the lasers.

No amplifier was used, only a "bias tee" to avoid high voltage on the oscilloscope. The charge measured is expressed in minimum ionizing particles (MIPs) charge units, using the equivalence one MIP  $\simeq 3.5$  fC in a  $300 \mu\text{m}$  of silicon. The calibration plots can be seen in figure 3.13 and 3.14 for the IR laser, the one used for the measurements in this work.

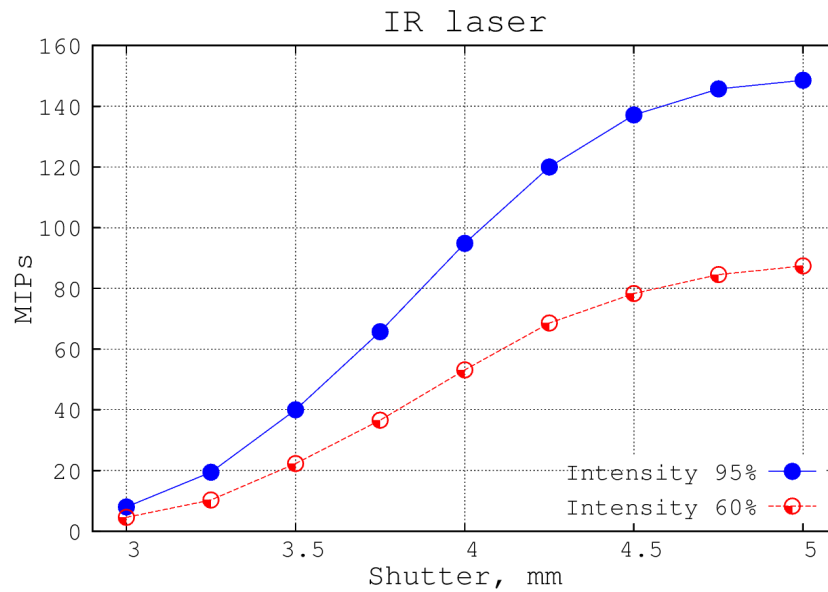


Figure 3.13: IR laser intensity as a function of the position of the manual attenuator for two different intensities.

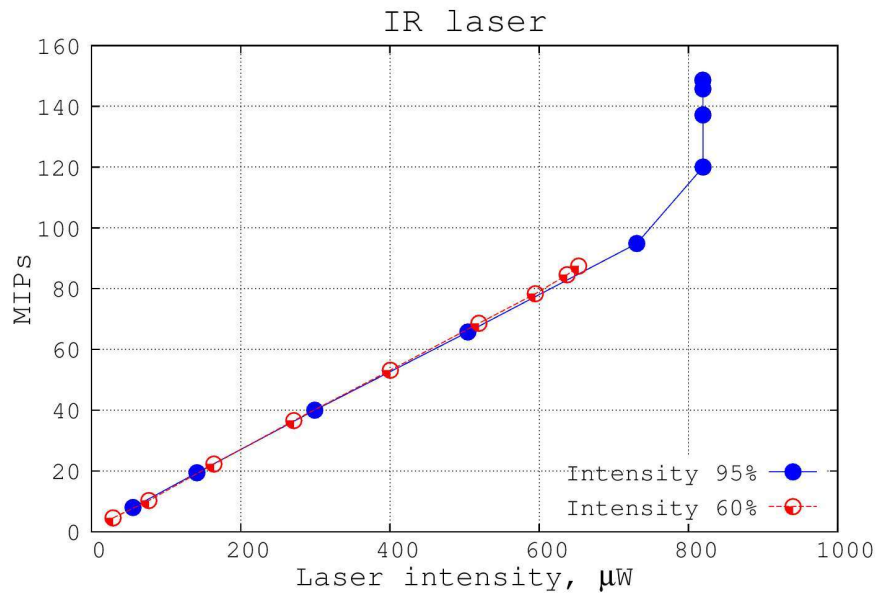


Figure 3.14: IR laser intensity as a function of the laser intensity measured in the reference diode. The signal of the reference diode saturates at  $800 \mu\text{W}$ , which receives 10% of the total intensity. See figure 3.12.

Likewise, the sensitivity of the TCT set-up was measured. Using the IR laser source at 60% or its intensity in the same diode, but in this case using a pre-amplification stage

(CIVIDEC C2), was possible to determinate that the set-up is not sensible to signals below  $\sim 1.5$  MIPs, that correspond to a pulse of about  $1 \mu\text{A}$  coming out of the sensor. This correspond to a shutter position of 2.5 mm, but the signal-to-noise of the measured signal is already very low as can be seen in figure 3.15, where it is compared the charge collected curve at two different laser intensities: 1.5 MIPs and 40 MIPs.

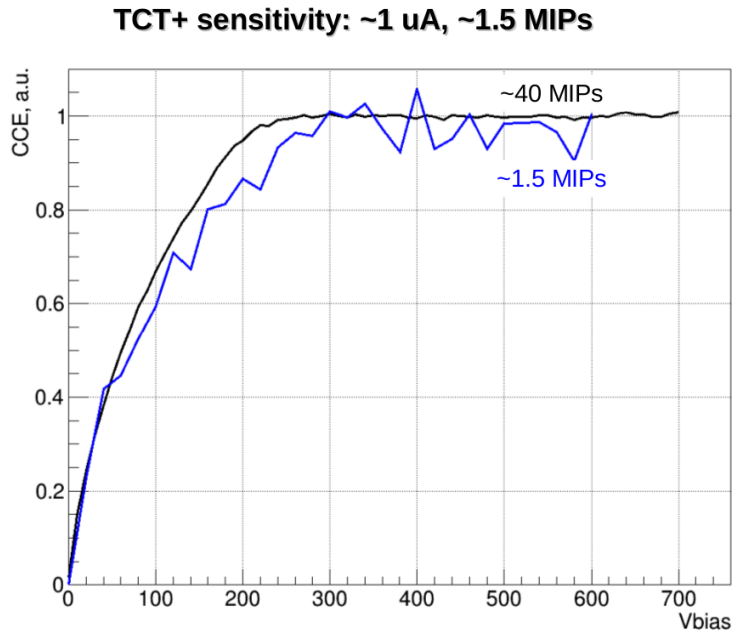


Figure 3.15: Charge collected with IR laser, top illumination at 60% of the intensity and a room temperature in a dd-FZ  $300 \mu\text{m}$  p-type silicon diode. It has been measured at two different shutter openings: 2.5 mm which correspond to laser intensity of around 1.5 MIPS and 3.8 mm which correspond to a laser intensity of about 40 MIPS.

### 3.3 Radioactive source characterization

With a radioactive source is possible to perform signal-to-noise studies, measurements of the charge collected and study Landau fluctuations in the energy deposits of charged particles in the sensors. In this work a  $^{90}\text{Sr}$  radioactive source was used. Strontium-90 is a radioactive isotope of strontium produced by nuclear fission, with a half-life of 28.8 years. It undergoes  $\beta^-$  decay into Yttrium-90 with a decay energy of 0.546 MeV.  $^{90}\text{Sr}$  can be considered a pure electron emitter. In Figure 3.16a the energy spectrum of the electrons emitted from the  $^{90}\text{Sr}/^{90}\text{Y}$  source is shown [41]. The response of a silicon detector to a  $^{90}\text{Sr}$  is considered

similar to the response to a Minimum Ionizing Particle (MIP). A MIP is a particle whose mean energy loss rate through matter is close to the minimum. This occurs when the kinetic energy of a particle is at least twice its rest mass. In the case of electrons can be considered as minimum ionizing particles when their kinetic energy is greater than 1 MeV. The absorption of the beta electron is described by the Bethe-Bloch process. Electrons cross the silicon depositing energy according to Bethe formula. Figure 3.16b shows the electron absorption in silicon [42].

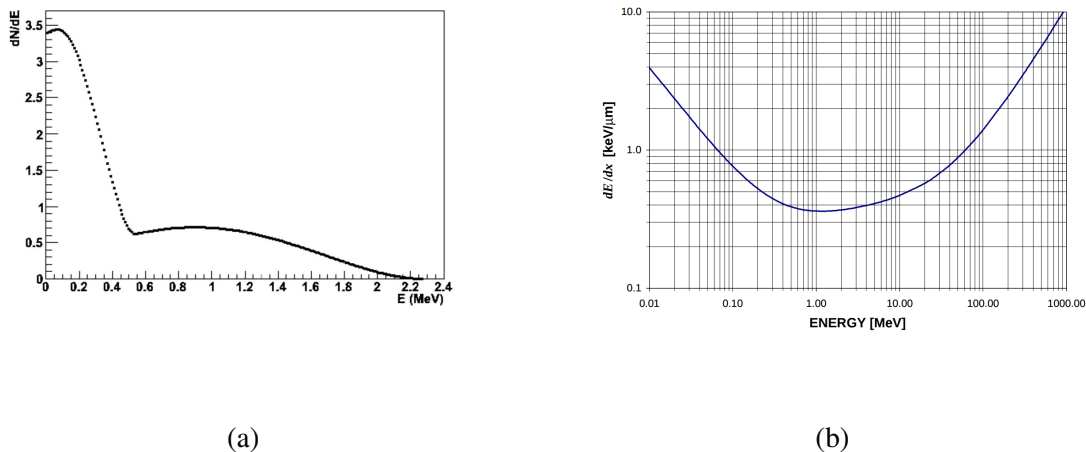


Figure 3.16: Energy spectrum of the electrons emitted from the  $^{90}\text{Sr}/^{90}\text{Y}$  source, as modelled in the GEANT simulation (a) [41]. Bethe-Bloch graph for beta electron absorption in silicon (b) [42].

### 3.3.1 Description of the set-up

As a part of this work, in order to perform radioactive source measurements in silicon pads, a new test station was developed at CERN. On this task I took full responsibility in terms of design, equipment acquisition, assembling and software development for the DAQ and data analysis. This work was granted by AIDA-2020, inside the WP 14: "Infrastructure for advanced calorimeters", task 14.3: "Test infrastructure for innovative calorimeters with semiconductor readout" [43]. The main objective of this new set-up is to determine signal characteristics in highly irradiated silicon sensors, in particular focused in energy-loss fluctuations (Landau fluctuations) in the energy deposits of charged particles. Studying these effect, and in particular the impact of radiation damage, requires the development of a dedicated test station. A test station was designed and built according to these requirements and it

is presented as a part of this work. The set-up can be operated at temperatures down to  $-70^{\circ}\text{C}$  with low humidity ( $\text{RH} < 5\%$ ) and with a very low noise readout system. Figure 3.17 shows the main components of the set-up that are listed below following the labels shown in the pictures.

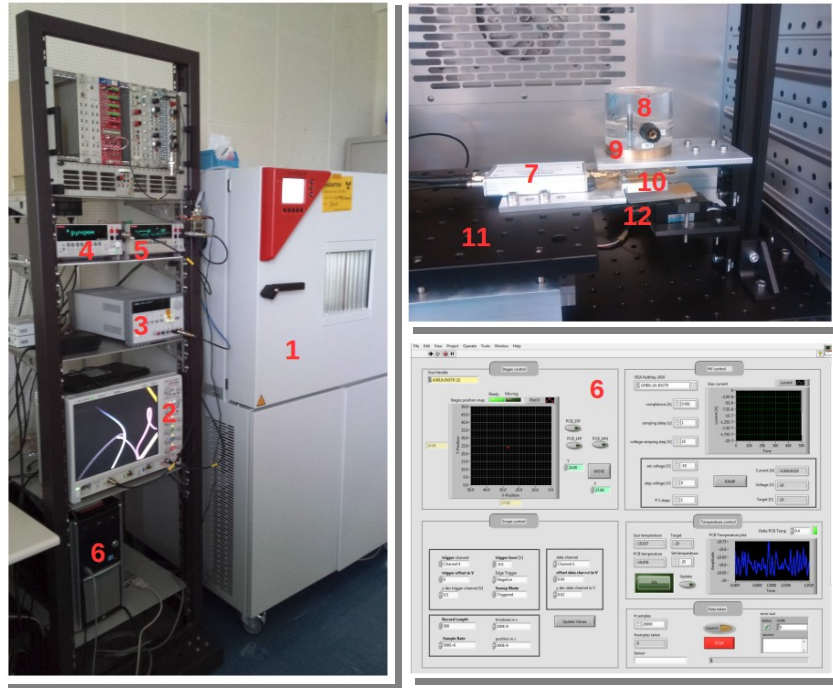


Figure 3.17: Main elements of the new test station. Left: Outside view with the electronics rack to the left and the climate chamber holding the sensor under test in the inside. Right top: Radioactive Source, amplifier and sample holder inside the climate chamber. Right bottom: GUI of the LabVIEW software controlling the system components and performing the data acquisition.

- Binder climatic chamber (1): can be set to temperatures between  $-70^{\circ}\text{C}$  and  $180^{\circ}\text{C}$ , keeping inside a low humidity atmosphere (below 5% RH) to avoid condensation problems.
- Agilent DSO 9254 oscilloscope, with an analog bandwidth of 2.5 GHz (2): two channels are used, one for the triggering and the other for the data acquisition.
- Low voltage power supply (3): up to 25 V for biasing the amplifiers (7) and photomultiplier (12)

- Digital multimeter (4): it reads a PT1000 resistance mounted in a pcb and placed close to the sensor that is used to obtain the correct value of the temperature in the sensor. Despite the temperature inside the climatic chamber being very stable and quickly settled, the cooling of the sensor towards ambient temperature needs more time and this extra reference in the sensor is required.
- High voltage power supply (5) for biasing the sensor and at the same time measure the reverse current. Keithley 2410 source that can go up to 1100 V is used.
- PC and GUI (6): A PC controls the different devices of the set up through a LabVIEW GUI customized for this test station.
- Amplifier (7): a Cx-L spectroscopic amplifier for large capacitive input load from CIVIDEC is used for the readout of the sensors. It is a very low noise charge amplifier that has been optimized in collaboration with the manufacturer for measuring highly irradiated sensors. Main characteristics of this amplifier are: ENC noise of  $300 + 10/C_L$  electrons (where  $C_L$  is the capacity load in pF), a Gain of 12 mV/fC and SNR at 4.3 pF of 17.5/fC [40].
- Strontium-90 radioactive source (8): this beta source is used for the measurements and characterization of the silicon sensors.
- Collimator (9): different size collimators from  $\varnothing 1$  mm to  $\varnothing 3$  mm can be used for controlling the trigger rate and the beam spot under the strontium-90 radioactive source.
- Support for the silicon sensor (10) is needed to fix its position inside the set-up and allow a good alignment between the radioactive source, the sensor and the photomultiplier. Moreover, the PCB with the sensor and the the PT1000, is connected directly to the amplifier by a sma adapter to minimize the noise.
- XY stages (11): special stages for the positioning of the sensor from Newport manufacturer are used. They can be operated at this very low temperature that is possible to reach inside the climatic chamber with a precision of few microns.
- Photomultiplier (PMT) (12): is needed for the triggering. The only electrons that will trigger the PMT, are those that traverse the detector and deposit enough energy in the scintillator to exceed the PMT threshold.

### 3.3.2 Data taking

For the data taking the trigger signal and the data signal are connected directly to two different channels of the oscilloscope. The trigger signal is coming from the photomultiplier and the threshold for the trigger is set adequately over the noise level. The acquisition rate depends on the collimator used and ranges from around 50 Hz (for the  $\varnothing 1$  mm) to around 200 Hz (for the  $\varnothing 3$  mm). In order to allow these high rates in the readout of the oscilloscope, the data is read directly from the internal ADC of the oscilloscope. The linear output range of the charge amplifier is from 0 V to 2 V, with a Gaussian pulse shape. The rise time is 80 ns and the FWHM 180 ns. The amplitude of the pulse is proportional to the charge measured with a gain of 12 mV/fC. For a further analysis of the signal one microsecond of the waveform (1024 points, about 1 ns resolution) is taken and stored in real time in to a binary datafile. Usually, for a proper analysis and parametrization of the charge deposition in the diode in every working point (voltage and temperature) are needed 20.000 waveforms. In figure 3.18 is shown the average pulse of 20.000 waveforms taken with a fully depleted unirradiated  $300 \mu\text{m}$  thickness diode.

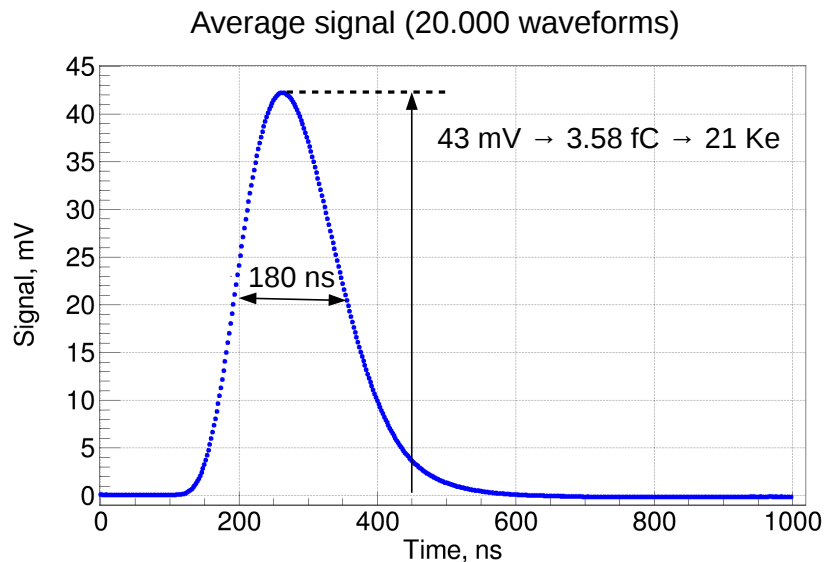


Figure 3.18: Average signal from 20.000 waveforms taken in an unirradiated dd-FZ  $320 \mu\text{m}$  diode with the  $^{90}\text{Sr}$  source. The measurements were done at  $20^\circ\text{C}$  and 400 V. The pulse amplitude is proportional to the charge collected (12 mV/fC).

### 3.3.3 Analysis

For the analysis a ROOT code was implemented [44]. From each waveform the amplitude of the pulse is computed, that is always delayed around 250 ns from the beginning of the waveform peaking time. For a proper estimation of the pulse amplitude the noise is computed in the first 100 ns of the waveform and a baseline correction is made. The histogram with the charge distribution is fitted using a convoluted Landau and Gaussian function. The Gaussian parameter of the distribution ( $G\sigma$ ) is not fixed to the measured electronic noise. It was observed that the Gaussian component of the charge distribution is higher than the contribution of the electronic noise which implies that there are more Gaussian components in the charge deposition. From the Landau fit are extracted the parameters needed to parametrize the charge distribution: the most probably value (MPV), and the width. The Landau maximum location need to be shifted due to the convolution of one symmetric and one asymmetric function [45]. The noise is evaluated in the first 100 ns of the waveform as the root mean square (RMS) of the waveform distribution. Mainly the noise depends on the input capacitance in the amplifier ( $300 + 30/pF$  electrons). Higher the capacitance higher the noise. To evaluate if there were some extra noise contributions in the data taking, the diode was moved out of the beam source-photomultiplier. As expected, the noise was the same when there was signal in the diode as when there was no signal, see figure 3.19. In figure 3.20 is shown how the fit is done in a fully depleted unirradiated  $300 \mu\text{m}$  thickness diode. The noise contribution is fitted in red and the charge distribution is fitted in blue with the convoluted Landau and Gaussian function.

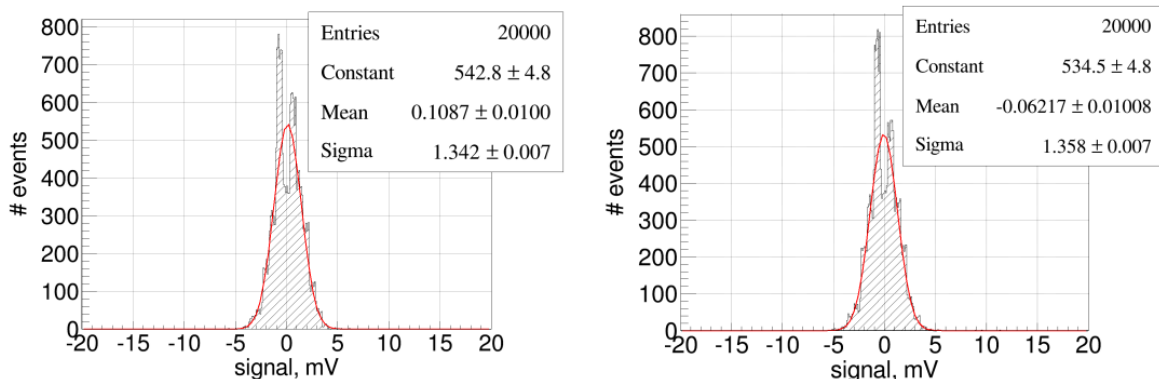


Figure 3.19: Noise distribution without signal in the diode (left). The  $^{90}\text{Sr}$  source is used only for triggering the photomultiplier. Noise distribution with signal in the diode (right). Normal configuration.

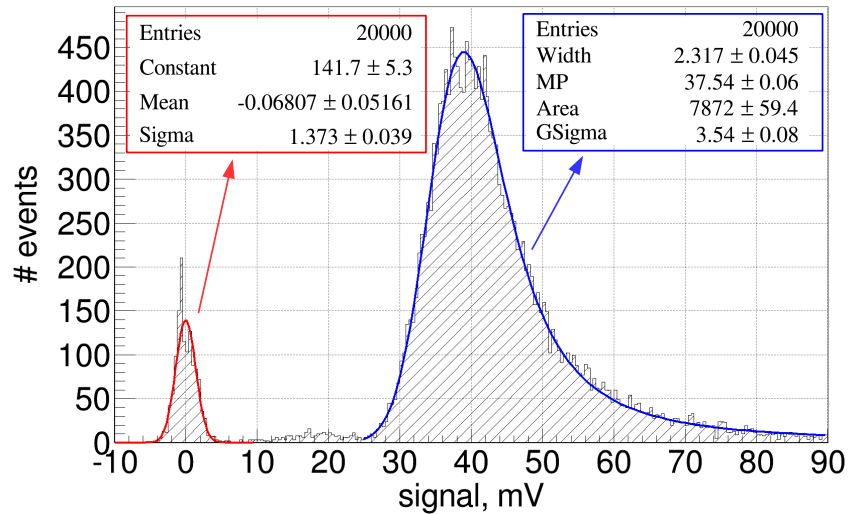


Figure 3.20: Fitting of the charge distribution using a convoluted Landau and Gaussian function. The Gaussian component of the charge (3.54) is higher than the single contribution of the electronic noise (1.37).

### 3.3.4 Oscilloscope and amplifier calibration

The oscilloscope and the charge amplifier were calibrated in order to ensure a proper conversion in the measurements from ADC to millivolts (oscilloscope step) and then from millivolts to electrons (amplifier step). For the oscilloscope pulses of a known amplitude were measured and compared with the amplitude measure in the internal ADC. The result of the calibration is shown in figure 3.21. For the amplifier a fast pulse generator was used with a tunable amplitude to provide rectangular pulses as an input. From each input pulse the charge was computed as the integral of the pulse and it was compared with the pulse amplitude given by the amplifier in the output. For each point several measurements were taken. The result of this calibration is shown in figure 3.22. The output is linear in the range used in this work as expected.

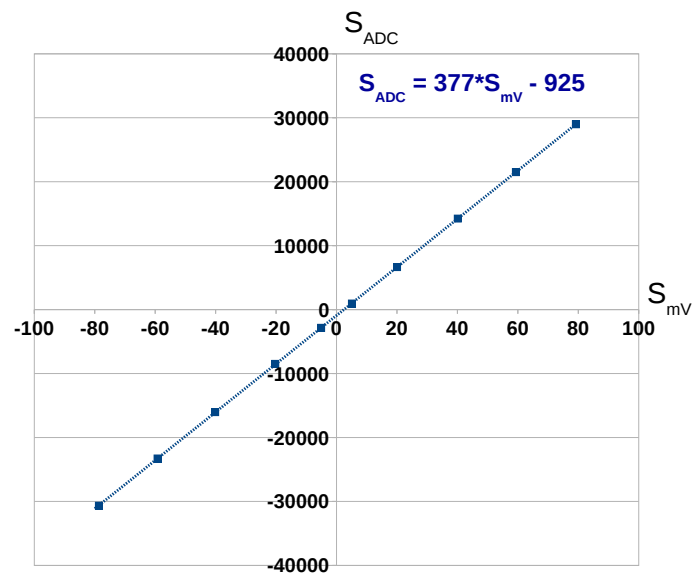


Figure 3.21: Calibration plot of the internal ACD of the oscilloscope.

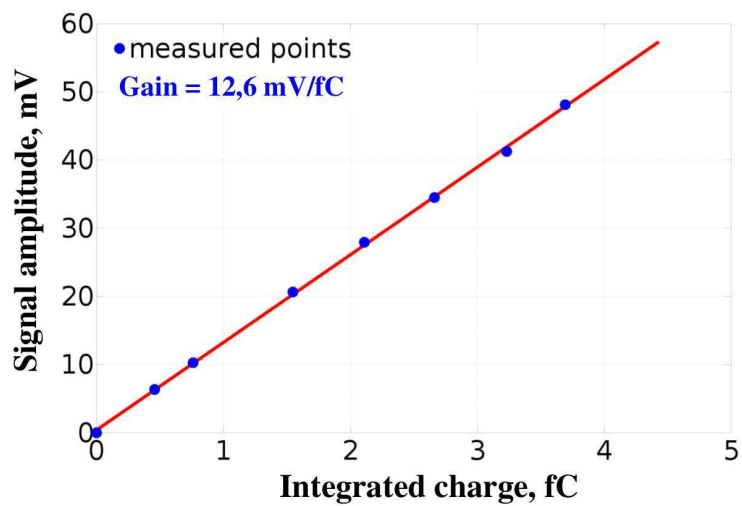


Figure 3.22: Calibration plot of the charge amplifier.

---

## 3.4 Test beam

Test beam facilities at CERN were used for this propose. Basically at CERN there are two main facilities prepared for beam test [46]:

- PS East Area, placed in Meyrin, that has 5 beam lines for a total length of 300 m. The main characteristics of this lines are:
  - Momentum between 1 GeV/c and 15 GeV/c
  - Particle type: electrons, hadrons and muons with a maximum intensity of  $2 \times 10^6$ . Particles per spill (typically used  $10^3$  -  $10^4$ )
  - Spill structure: the spill length is 400 ms and usually there is 1 spill every 33.6 s.
- SPS North Area, placed in Preveessin, which has 7 beam lines for a total length of 5.8 km. The SPS proton beam of 400/450 GeV/c is extracted to the North Area towards the three North Area primary targets T2, T4 and T6. Then, from these primary targets are extracted the the 7 beam lines available in this facility. A schematic of the different lines is shown in figure 3.23. The main characteristics of this lines are:
  - Momentum between 10 GeV/c and 400 GeV/c for H2, H4 and H8 lines and between 5 GeV/c and 200 GeV/c for H6 line.
  - Particle type: electrons, hadrons and muons with a maximum intensity of  $2 \times 10^8$ . Particles per spill
  - Spill structure: the spill length is 4.8 - 9.6 s with usually 1 spill every 14 - 48 s.

During this work four different test beam were performed, all of them in the SPS North Area facility, H2 line, in order to measure charge collection, spacial resolution, signal to noise and timing capabilities. The set-ups and the used particle beams will be described more in detail in the next chapter. In order to estimate the spacial resolution in one of the test beams done with silicon micro-strips, a telescope from the EUDET project was used in 2012.

- EUDET beam telescope

EUDET was a project supported by the European Union in the 6th Framework Programme structuring the European Research Area. The goal was to establish common

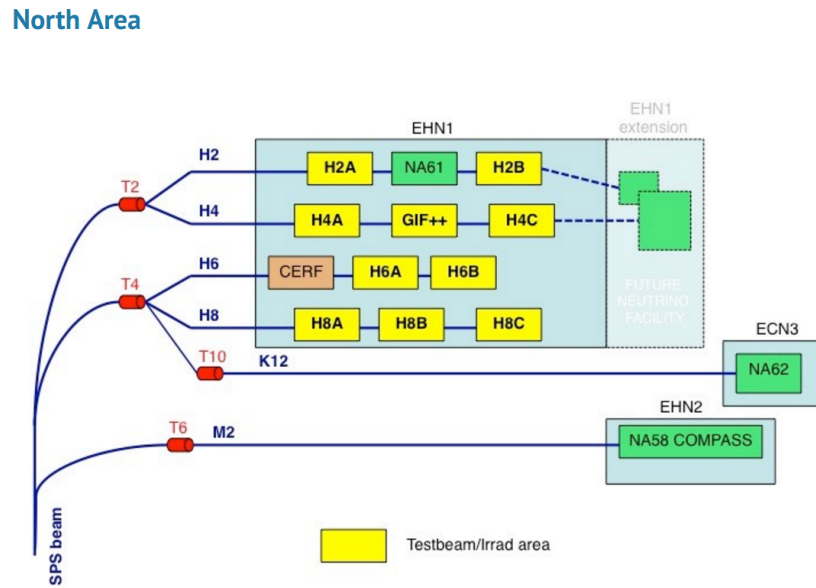


Figure 3.23: Schematic view of the different lines in the SPS North Area test beam facility [47].

European infrastructure for the research on advanced detector technologies for the International Linear Collider (ILC) [48].

DESY Advanced Telescope Using Readout Acceleration (DATURA) was the telescope used in the test beam. This telescope belongs to a series of telescopes driven by the community and the successive European-funded projects AIDA and now AIDA 2020 [43]. It is a Mimosa pixel telescope with six planes of MIMOSA26 sensors, see figure 3.24. It has precise and flexible mechanics and central DAQ components, triggering is controlled by a custom Trigger Logic Unit (TLU). The position resolution of the telescope is about  $4 \mu\text{m}$  in the best possible conditions (particle energy, scattering and distance between planes) [49]. The telescope is mounted on a movable support with step motors remotely controlled.

The TLU receives signals from scintillators in front of and behind the telescope, and generates triggers that it distributes to the telescope and any DUT. The four scintillators inputs can be combined in an arbitrary fashion (AND, OR, VETO) to generate the trigger signal, there is also an internal trigger generator for testing and pedestal runs. The overlap area between the four scintillators is about  $1 \text{ cm}^2$ . Several internal scalers allow monitoring of the running conditions. For each generated trigger a trigger counter is incremented, and a timestamp is stored in an internal buffer.



Figure 3.24: EUDET type beam telescope at DESY [50].

The sensitive elements equipping each plane of the telescope have to be highly granular and thin. Thus, CMOS pixel sensors were used to fulfill the EUDET telescope requirements in terms of spatial resolution, material budget, sensitive area dimensions and readout time. The telescope reference planes are equipped with  $18.4\ \mu\text{m}$  pitch sensors, called Mimosas26 [51]. Mimosas26 has an active area of  $224\ \text{mm}^2$  with integrated zero suppression. The matrix is organized in 576 rows and 1152 columns. At the bottom of the pixel array, each column is connected to an offset compensated discriminator to perform the analogue to digital conversion. Zero-suppression is then used to reduce the data rate. Mimosas26 is a fully digital sensor with binary readout. This architecture allows a fast readout frequency of about 10 k frames/s.

### 3.5 Irradiation facilities

One of the main objectives of this work was the characterization after neutron irradiation of silicon diodes. For this purpose an irradiation campaign was performed by using a nuclear reactor. The irradiation campaign consisted of several particle fluences of neutrons where the expected radiation fluences were very high, up to  $1.6 \times 10^{16}\ \text{neq}/\text{cm}^2$ . The neutron irradiation

facility used was the Reactor Center at Jozef Stefan Institute in Ljubljana (Slovenia) [52]. It is a TRIGA Mark II research reactor. Depending on the reactor power, the particle flux (neutrons) varies between  $2 \times 10^9 n/cm^2s$  and  $2 \times 10^{12} n/cm^2s$  with a continuous energy spectrum. About 1/3 of the flux is composed of fast neutrons (above 0.1 MeV). The neutron energy spectrum extends up to 10 MeV and a hardness factor for normalization was obtained by Žontar [53]. The fluence accuracy is assured to be within 10% [39].



## Chapter 4

# Radiation tolerance assessment of deep diffused float zone and epitaxial diodes

The basic parameters for the High Granularity Calorimeter (HGCAL) sensors design are based on results obtained for the CMS Phase-II Tracker R&D [54, 55] and complemented by further dedicated measurements using neutron fluences up to  $1.6 \times 10^{16} \text{ n}_{eq}/\text{cm}^2$  that will be presented in this chapter. At the High Luminosity Large Hadron Collider (HL-LHC) the silicon sensors of the HGCAL will be exposed to hadron fluences ranging from about  $2.0 \times 10^{14} \text{ n}_{eq}/\text{cm}^2$  to about  $1.0 \times 10^{16} \text{ n}_{eq}/\text{cm}^2$  as it is shown in figure 4.1. The main difference between the tracker system and the HGCAL is that whereas in the tracker the fluence is dominated by charged hadrons for a radius up to about 20 cm, in the case of the HGCAL it is neutrons that dominate. A dedicated campaign was done in this work to determine if the performance of the sensors is affected differently by neutrons. This is the first time that a radiation hardness study is done after a pure neutron irradiation on these devices up to a fluence of  $1.6 \times 10^{16} \text{ n}_{eq}/\text{cm}^2$ . The results are presented in this chapter.

## 4.1 Devices under investigation and irradiation fluences

The diodes under investigation are deep-diffused float-zone (dd-FZ) and epitaxial (Epi) silicon pads of different active thickness produced by Hamamatsu [56] within the framework of the CMS tracker upgrade campaign [57, 58]. This manufacturer was selected for the good quality and capability to produce the amount of sensors needed for a large scale production,

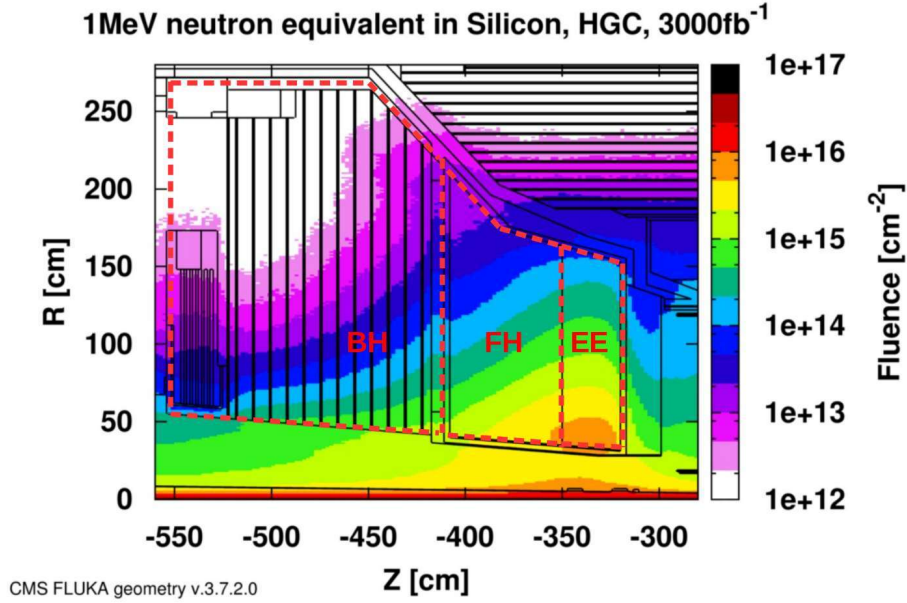


Figure 4.1: Equivalent 1 MeV neutron fluence for Phase-II endcap calorimetry at HL-LHC [13].

although other producers are being considered for the mass production phase. Part of these diodes have already been object of different studies in previous thesis works [29, 59]. This study includes both p-on-n and n-on-p sensors, with active thickness of 320, 200, 100 and 50  $\mu\text{m}$  and an area of 25  $\text{mm}^2$ . On the top side of the detector there is a square opening on the metallization of 9  $\text{mm}^2$  to allow top laser illumination, the metallic contact pad and the guard ring for isolation, on the back side there is a metallic grid. See figure 4.2 where there is a picture of the top side in the left and of the back plane in the right. In figure 4.3 a detailed schematic of the diodes is shown.

The diodes were irradiated up to a fluence of  $1.6 \times 10^{16} \text{ n}_{eq}/\text{cm}^2$  at the Triga reactor in Ljubljana (Slovenia) [60]. The reactor provides high neutron fluxes. About 1/3 of the flux is composed by fast neutrons above 0.1 MeV. Table 4.1 shows the different fluence ranges investigated for each type of diode in accordance with figure 4.1 and planned position in the HGCAL. In order to cover the full fluence range expected in the HGCAL and to understand irradiations performed in several exposure steps, four diodes have been irradiated twice. For the dd-FZ 320  $\mu\text{m}$  and dd-FZ 200  $\mu\text{m}$  two diodes have been re-irradiated after the first measurement to reach the next higher fluence given in table 4.1 (one diode from lowest to middle

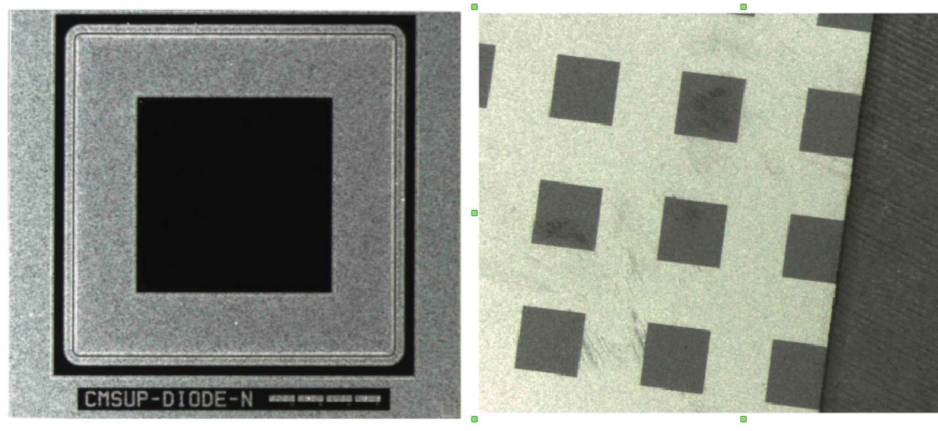


Figure 4.2: Front side (left) and back plane (right) of one p-on-n diode [58].

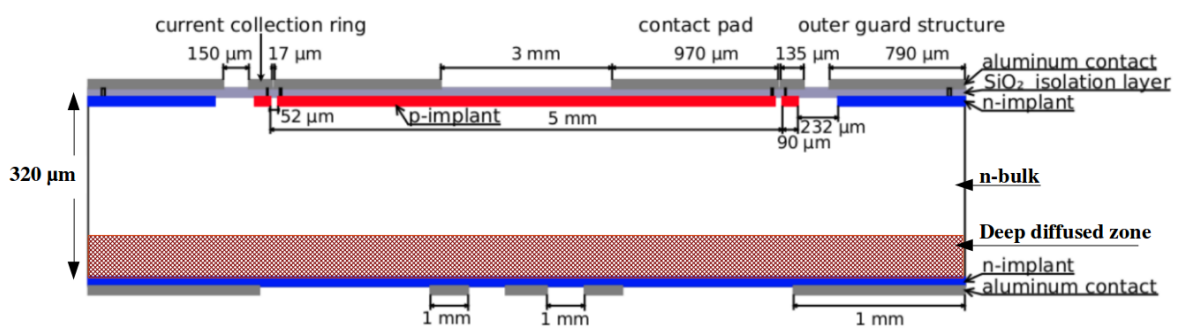


Figure 4.3: Schematic (not to scale) of the diodes studied in this work. In this case is shown a dd-FZ p-on-n diode [29].

and one diode from middle to highest fluence). The corresponding measurement results are included in the data analyses and have not been found to differ significantly from identical diodes irradiated in a single irradiation step.

Type, thickness	Fluences, $n_{eq}/\text{cm}^2$		
dd-FZ 320 $\mu\text{m}$	$4.0 \times 10^{14}$ (2)	$6.0 \times 10^{14}$ (3)	$9.0 \times 10^{14}$ (1)
dd-FZ 200 $\mu\text{m}$	$1.5 \times 10^{15}$ (2)	$2.5 \times 10^{15}$ (3)	$4.0 \times 10^{15}$ (1)
dd-FZ 120 $\mu\text{m}$	$6.25 \times 10^{15}$ (2)	$1.0 \times 10^{16}$ (1)	$1.6 \times 10^{16}$ (1)
Epi 100 $\mu\text{m}$	$6.25 \times 10^{15}$ (2)	$1.0 \times 10^{16}$ (2)	-
Epi 50 $\mu\text{m}$	-	$1.0 \times 10^{16}$ (2)	$1.6 \times 10^{16}$ (2)

Table 4.1: Summary of sensor types and irradiation fluences covered in this work. The number of diodes measured at the given fluence is indicated in brackets. Silicon sensor arrangement in table 1.2.

After the irradiation the following properties were measured in the different set-ups: reverse current (IV), capacitance (CV), charge collection efficiency (CCE) with an infrared laser and minimum ionizing particle (MIP) sensitivity with radioactive source. Their timing response was measured on a dedicated test beam. The most relevant results of the characterization have already been published in [61, 62]. The operation temperature of the HGCal silicon sensors will be below  $-30^\circ\text{C}$ , at a bias voltage between 600 V and 800 V. In order to compare results with the study carried out for the CMS tracker upgrade with proton irradiation and now extended to this neutron irradiation, most of the measurements were done at  $-20^\circ\text{C}$ . At the same time, it makes the operation in some of the set-ups easier, as some of them can not go down to  $-30^\circ\text{C}$ . Moreover, the extrapolation of the results at  $-30^\circ\text{C}$  is well understood, see section 4.2, figure 4.10. All measurements were done after an annealing of 10 min at  $60^\circ\text{C}$ , mainly for two reasons: right after irradiation the properties of the silicon diodes can change very quick within the first steps of annealing, and during the live time of the detector in the HL-LHC this annealing is expected. Thus, the measurements are done in a more realistic scenario.

## 4.2 Current-voltage characterization: bulk damage and power consumption

The motivation of the current-voltage (IV) characterization is to evaluate the bulk damage and measure the power consumption of the sensors after neutron irradiation. Thus, it is possible to estimate the power contribution coming from the reverse current of sensors in the calorimeter at the end of their life.

The IV measurements were performed at  $-20\text{ }^{\circ}\text{C}$  except for the non-irradiated diodes, which were measured at room temperature ( $20\text{ }^{\circ}\text{C}$ ). The bias voltages applied reached 1000 V in steps of 10 V with the exception of the  $50\text{ }\mu\text{m}$  epitaxial diodes biased up to 400 V. The bias voltage was applied at the back side and the guard ring was connected to ground, see figures 4.2 and 4.3. Figures 4.4, 4.5, 4.6 and 4.7 summarize all the IV measurements done for the irradiated diodes; the unirradiated diodes are excluded in these plots.

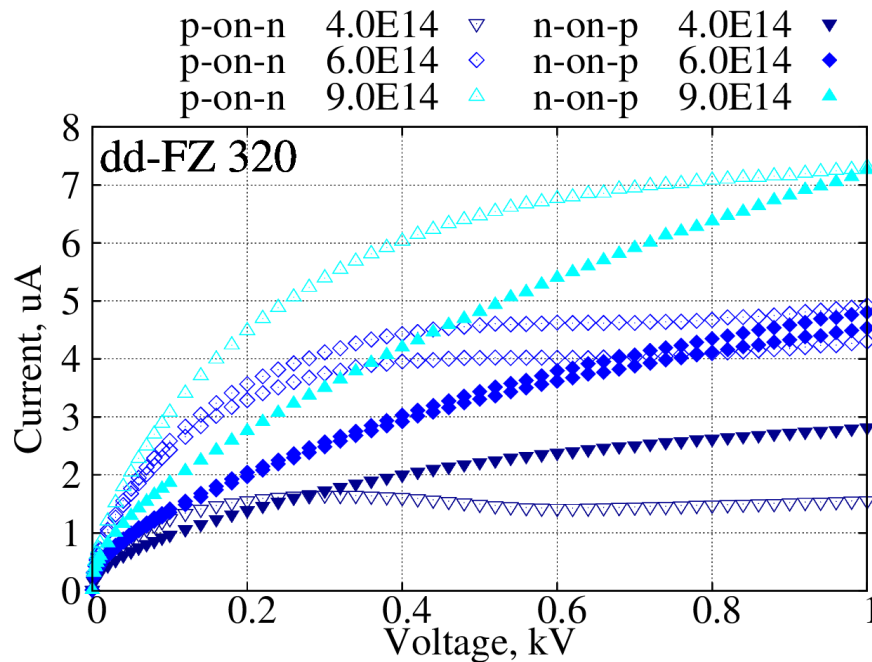


Figure 4.4: IV measurements for all the irradiated dd-FZ  $320\text{ }\mu\text{m}$  diodes at  $-20\text{ }^{\circ}\text{C}$ .

At the highest fluences, the reverse current as a function of the voltage increases continuously and does not reach a plateau below 1 kV. Only in the case of dd-FZ 320 p-on-n a plateau is observed which is not visible on the dd-FZ 320 n-on-p and can be an indication of under depletion in the n-on-p diodes (see figure 4.4). For the rest of the thicknesses, both bulk types

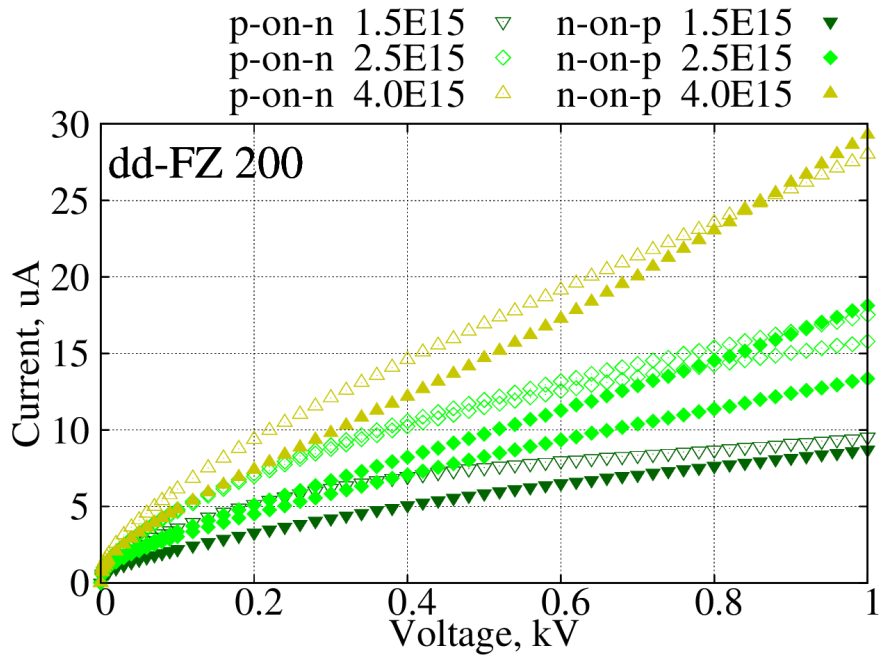


Figure 4.5: IV measurements for all the irradiated dd-FZ 200  $\mu\text{m}$  diodes at  $-20^\circ\text{C}$ .

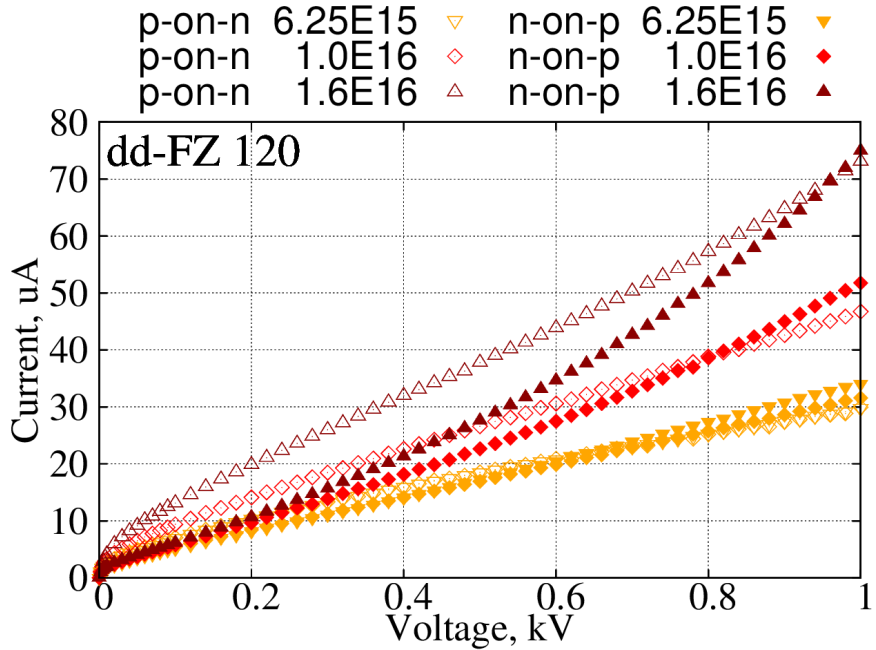


Figure 4.6: IV measurements for all the irradiated dd-FZ 120  $\mu\text{m}$  diodes at  $-20^\circ\text{C}$ .

behave the same. The reverse current ranges from a few  $\mu\text{A}$  to about  $70 \mu\text{A}$  after irradiation. Notice that a change in the slope of the epitaxial diodes at high voltage is observed, figure 4.7. This exponential effect can be an indication of some amplification mechanisms.

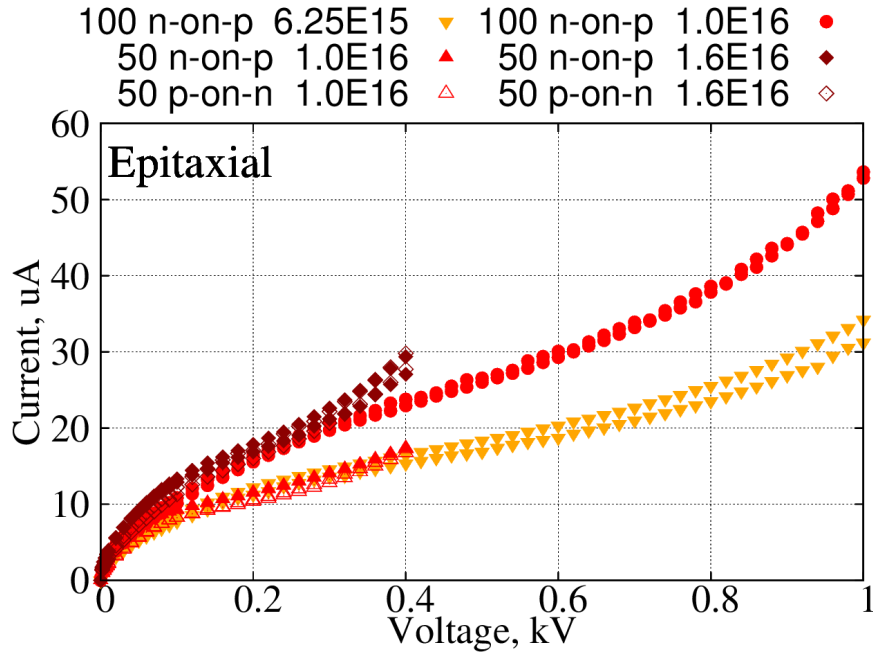


Figure 4.7: IV measurements for all the irradiated epitaxial diodes at  $-20^{\circ}\text{C}$ .

As was mentioned in chapter 2, the reverse current increases linearly with particle fluence. The proportionality factor is called alpha ( $\alpha$ ) and is given by equation 4.1 [34].

$$\Delta I = \alpha \Phi_{eq} V \quad (4.1)$$

The current-related radiation damage can be compared for different detector geometries if the increment of the reverse current measured after irradiation ( $\Delta I$ ) is normalized by the depleted volume of the diode ( $V$ ). If this normalized value of the reverse current is plotted as a function of the fluence ( $\Phi_{eq}$ ) according to equation 4.1, it is possible to compare these results with the alpha value that can be found in the literature [34]. Figure 4.8 and 4.9 show how the reverse current normalized by the volume of the diodes scales with the fluence. The results are shown at  $-20^{\circ}\text{C}$  and at two different bias voltages 600 V and 800 V. These results are compared with the alpha value taken from [34] and scaled according to the temperature dependence described in [33]. The agreement between the reference alpha value ( $9.0 \times 10^{-19} \text{ A/cm}$ ) and the alpha value calculated from the reverse current at 600 V and at 800 V as a function of fluence is within 15%. The epitaxial 100  $\mu\text{m}$  n-on-p were plotted but they were not considered for the fit. It can be seen that the current for the Epi 100 n-on-p diodes after irradiation is higher than the dd-FZ ones at 600 V and 800 V. This can be due to

some amplification mechanisms or an over-depletion in the subtract at high bias voltage.

There is an uncertainty in this way of determining the current related radiation damage. In the calculation, it is considered the volume of the unirradiated diodes fully depleted and is expected to be the same in the irradiated ones. But this is not the case as in most of them it is not possible to calculate the full depletion voltage, and therefore knowing if at 600 V or 800 V it is under depleted or fully depleted. If the diode is under depleted at a given bias voltage, the normalized current calculated is being underestimated. On the other hand, if the bias voltage selected is higher than the full depletion voltage, the normalized current calculated is being overestimated. This explains why the value at 800 V is higher than the value at 600 V.

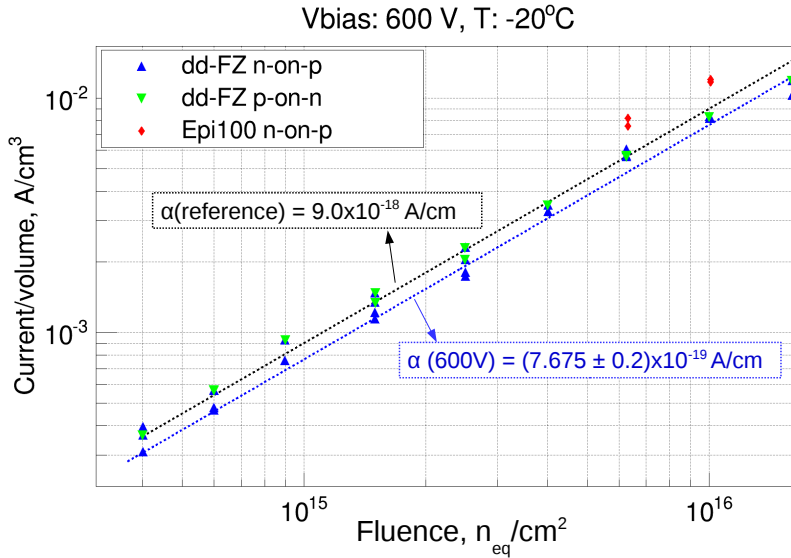


Figure 4.8: Reverse currents, as a function of neutron fluence, measured at  $-20^{\circ}\text{C}$  and 600 V. Epi 100  $\mu\text{m}$  n-on-p diodes are included in the plot but they were not considered for the fit.

Using equation 2.15 it is possible to scale reverse currents to the operational temperature of the calorimeter [33]. In order to validate this relation, bulk currents of different diodes were measured at different temperatures. In figure 4.10, the bulk current is plotted as a function of the temperature. The bias voltage used was 600 V and the bulk current was normalized to the value of the bulk current at  $-20^{\circ}\text{C}$  for all the sensors in order to compare them. It is possible to see how for different thickness and different levels of irradiations the points are in agreement with equation 2.15, plotted in dashed line. This is a clear indication that the

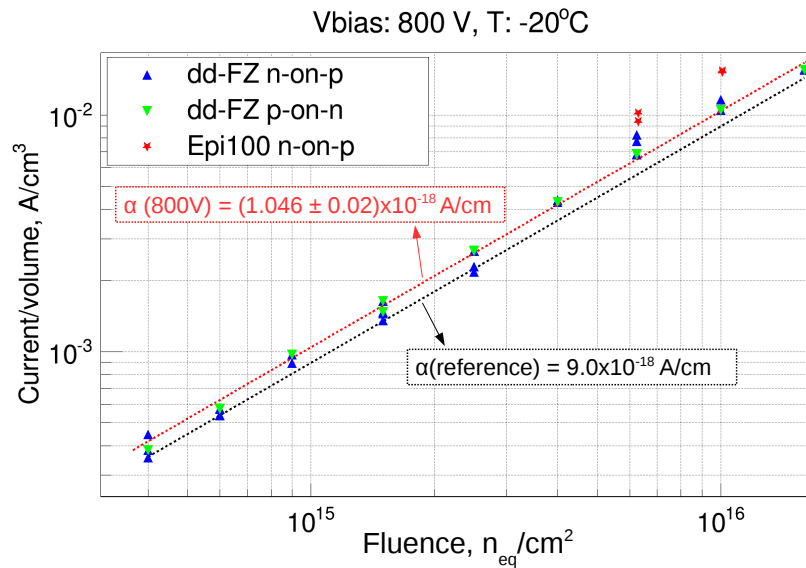


Figure 4.9: Reverse currents, as a function of neutron fluence, measured at  $-20^{\circ}\text{C}$  and 800 V. Epi 100  $\mu\text{m}$  n-on-p diodes are included in the plot but they were not considered for the fit.

reverse current is generated in the bulk of the diodes, otherwise it will scale in a different way with temperature. The values introduced in the equation were 1.21 eV for the effective energy ( $E_{eff}$ ) and  $8.6173 \times 10^{-5} \text{ eV/K}^{-1}$  for Boltzmann constant ( $K_b$ ).

The total power contribution coming from the reverse current of the diodes at the end of live, can be easily estimated taking into account some simplifications:

1. Assuming an operating bias voltage of 600 V.
2. At 600 V the average reverse current for the three different thicknesses at the end of live is about  $10 \mu\text{A}$ . This has been calculated taking into account only the dd-FZ diodes and reverse current at the nominal fluences expected. See figures 4.4, 4.5 and 4.19. In this way each diode will consume  $6 \times 10^{-3} \text{ W}$ .
3. Each diode has an area of  $25 \text{ mm}^2$  and the silicon diodes in the calorimeter will cover a total area of  $600 \text{ m}^2$ . This implies that each diode, in average, will contribute with around  $4.2 \times 10^{-6}\%$  of the power. In other words, it will be needed  $2.4 \times 10^7$  diodes to cover the full area.
4. According to figure 4.10, the reverse current at  $-30^{\circ}\text{C}$  will be lower than the values

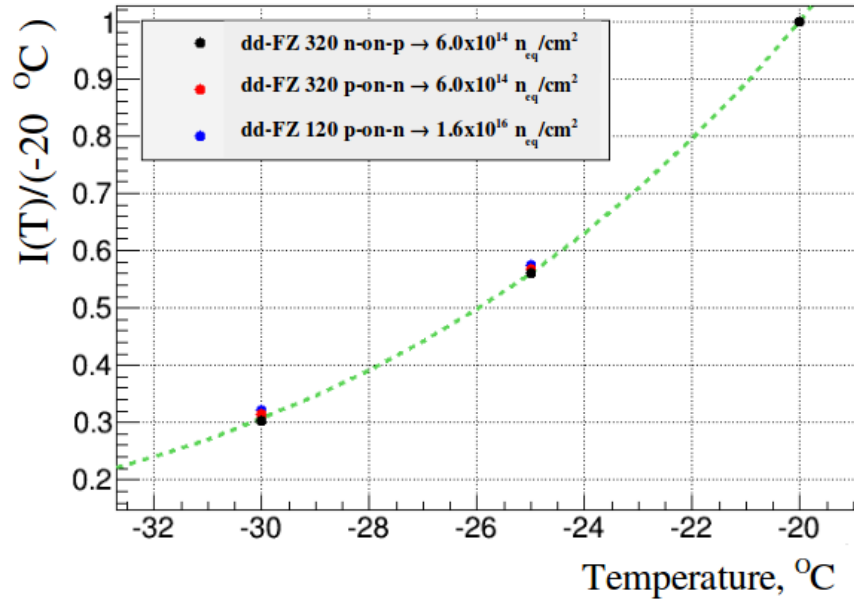


Figure 4.10: Measurements of the bulk current as a function of the temperature and normalized to the value of the current at  $-20\text{ °C}$ . The bias voltages was 600 V. Reference value is plotted in dashed line extracte from equation 2.15

measured at  $-20\text{ °C}$ . Thus, a factor of 0.3 needs to be applied (0.17 if the final operating temperature is  $-35\text{ °C}$ ).

Considering these points, the diodes power consumption in the calorimeter will be:

$$P_{diodes} = 0.3 \times 2.4 \times 10^7 \times 6 \times 10^{-3} \text{ W} = 43.2 \text{ kW} \quad (\text{at } -30\text{ °C}) \quad (4.2)$$

$$P_{diodes} = 0.17 \times 2.4 \times 10^7 \times 6 \times 10^{-3} \text{ W} = 24.5 \text{ kW} \quad (\text{at } -35\text{ °C}) \quad (4.3)$$

### 4.3 Capacitance-voltage characterization: thickness study

The main motivation of the capacitance-voltage (CV) characterization is to determinate the full depletion voltage, end capacitance ( $C_{end}$ ) and measure the active thickness of each type of diode. This work is easily done with the unirradiated diodes, but with the irradiated ones

it becomes more complicated and the method used for the unirradiated diodes can not be applied.

The CV measurements were performed at two different frequencies: 455 Hz and 1 MHz. Bias voltage and temperature were the same as for IV measurements. The bias voltage was applied from the back side of the diode and the guard ring was connected to ground in order to estimate properly the capacitance of the diodes. The circuit model used to determine the capacitance was a parallel RC circuit, see section 3.1.2. Figures 4.11, 4.12, 4.13, 4.14 and 4.15 summarize all the CV measurements done for these diodes at 455 Hz.

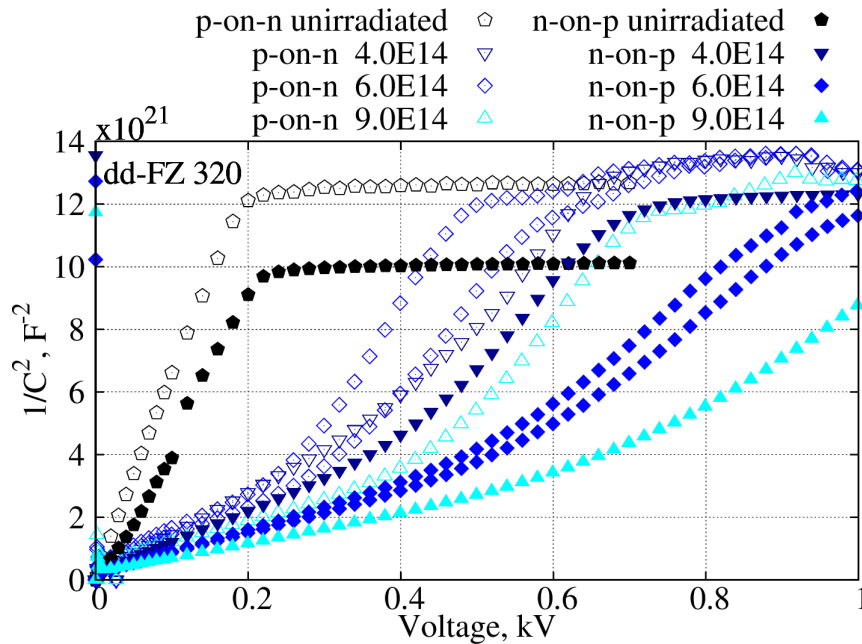


Figure 4.11: CV measurements for all dd-FZ 320  $\mu\text{m}$  diodes at  $-20^\circ\text{C}$  and 455 Hz

From the CV characterization it is possible to make a similar analysis that with the IV characterization. Only in the case of dd-FZ 320 p-on-n a plateau is observed after irradiation, see figure 4.11. Moreover, at a fixed voltage (e.g. 600 V) the capacitance of the n-on-p irradiated diodes is much higher than on the p-on-n, that could mean that the active volume is smaller and the charge collection capability would be reduced. For the rest of the thicknesses there are no big differences. Only on the epitaxial diodes the full depletion is visible in the plots, see figures 4.14 and 4.15. The increase of the capacitance above 300 V in the irradiated 50  $\mu\text{m}$  p-on-n epitaxial diodes happens only when the guard ring is floating; when it is connected to ground this effect disappears, see figure 4.15.

As mentioned before, full depletion voltage, and end capacitance are ones of the most

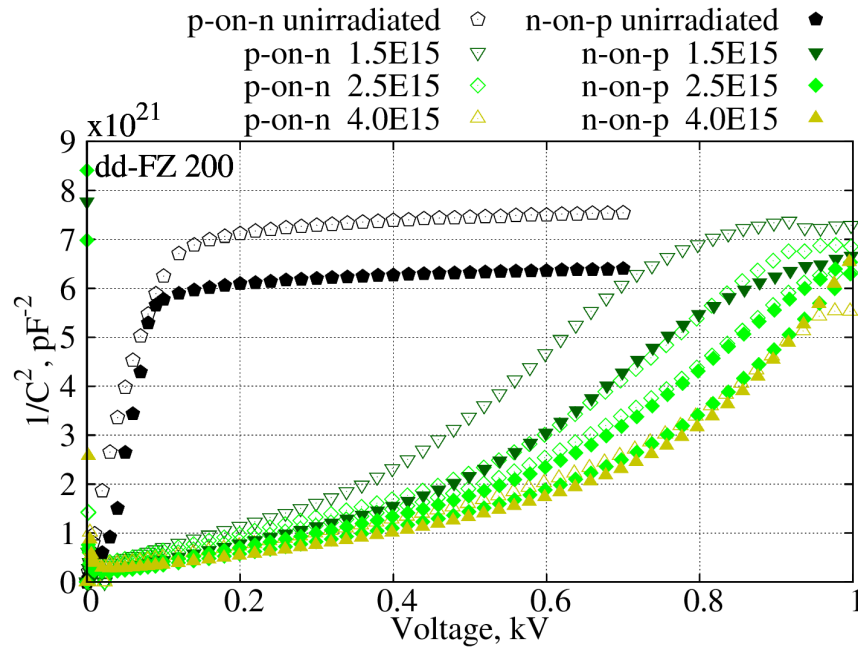


Figure 4.12: CV measurements for all dd-FZ 200  $\mu\text{m}$  diodes at  $-20^\circ\text{C}$  and 455 Hz

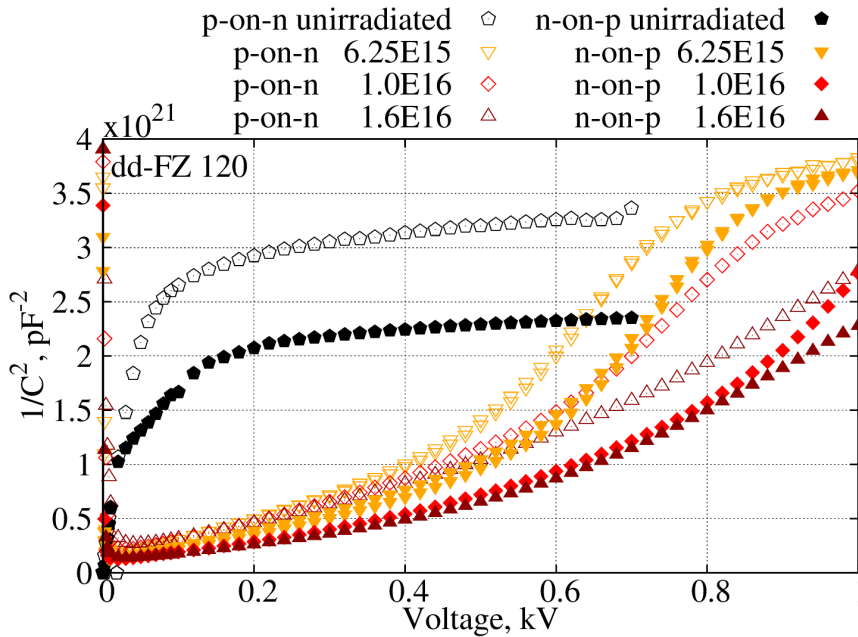


Figure 4.13: CV measurements for all dd-FZ 120  $\mu\text{m}$  diodes at  $-20^\circ\text{C}$  and 455 Hz

important parameters that can be extracted from the CV characterization. Measured  $C_{end}$  ranged between 10 pF for the thicker diodes to 50 pF for the epitaxial 50  $\mu\text{m}$ . The full depletion voltage and the  $C_{end}$  increased with the fluence. Another important parameter that

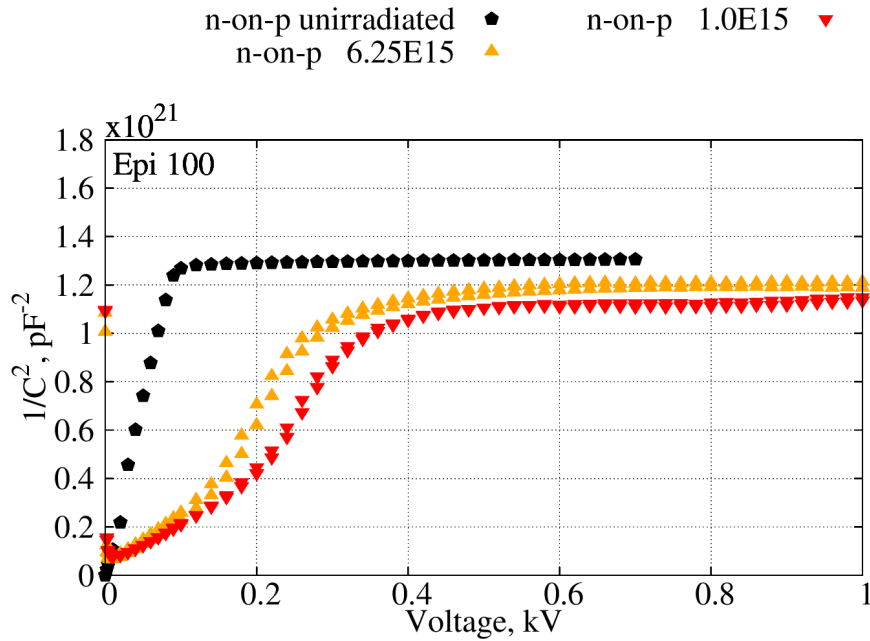


Figure 4.14: CV measurements for all epitaxial 100  $\mu\text{m}$  diodes at  $-20^\circ\text{C}$  and 455 Hz

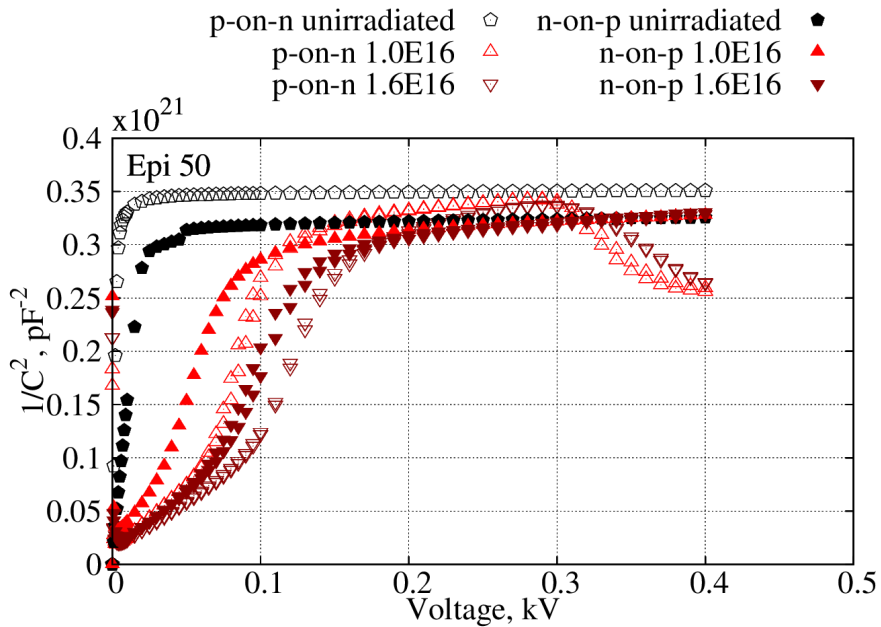


Figure 4.15: CV measurements for all epitaxial 50  $\mu\text{m}$  diodes at  $-20^\circ\text{C}$  and 455 Hz

can be extracted from the CV curve is the active thickness of the diodes, more relevant for the dd-FZ ones. At full depletion, the thickness of the diodes can be calculated by equation 3.1. The values of the full depletion voltage and the thickness calculated using this equation for the unirradiated diodes are summarized in table 4.2.

$$W(V) = \frac{\varepsilon_0 \varepsilon A}{C(V)} \quad (4.4)$$

<b>Bulk type</b>	<b>Nominal thickness (<math>\mu\text{m}</math>)</b>	<b>Full depletion (V)</b>	<b>Measured thickness (<math>\mu\text{m}</math>)</b>	<b><math>C_{\text{end}}</math> (pF)</b>
dd-FZ p-on-n	320	210	298	8.912
dd-FZ n-on-p	320	229	291	9.13
dd-FZ p-on-n	200	110	228	11.63
dd-FZ n-on-p	200	85	209	12.72
dd-FZ p-on-n	120	100	148	17.85
dd-FZ n-on-p	120	71	133	19.87
Epi n-on-p	100	100	95.8	27.70
Epi p-on-n	50	30	49.71	53.43
Epi n-on-p	50	35	47.81	55.55

Table 4.2: Pad sensors' main parameters before irradiation.

In order to study the homogeneity of the wafers used in this work, measurements performed in the scope of the HPK campaign for the CMS tracker upgrade were used [63]. These measurements were stored in a database accessible by all members of the campaign. The data can be read in XML or IEKP format and all tables and information available can be accessed in both formats. This CMS upgrade database is hosted at the University of Lyon. From this database were extracted all CV measurements done with dd-FZ diodes before irradiations at  $-20^\circ\text{C}$ , 455 Hz and with the guard ring connected to ground. More than 100 different measurements were found for this study. In figure 4.16, the  $C_{\text{end}}$  measured sorted by wafers are shown. Points with less diodes presents higher error bars. In table 4.3 the results organized by thickness and bulk type are summarized. The homogeneity of the dd-FZ wafers used in this work is good, within 5%.

<b>Bulk type</b>	<b>Nominal active thickness (<math>\mu\text{m}</math>)</b>	<b>Diodes measured</b>	<b>Mean <math>C_{\text{end}}</math> (pF)</b>	<b>RMS <math>C_{\text{end}}</math> (pF)</b>
dd-FZ p-on-n	320	32	8.78	0.20
dd-FZ n-on-p	320	18	9.05	0.14
dd-FZ p-on-n	200	26	11.76	0.15
dd-FZ n-on-p	200	18	12.66	0.42
dd-FZ p-on-n	120	13	17.89	0.6
dd-FZ n-on-p	120	10	19.68	0.1

Table 4.3: Homogeneity study results.

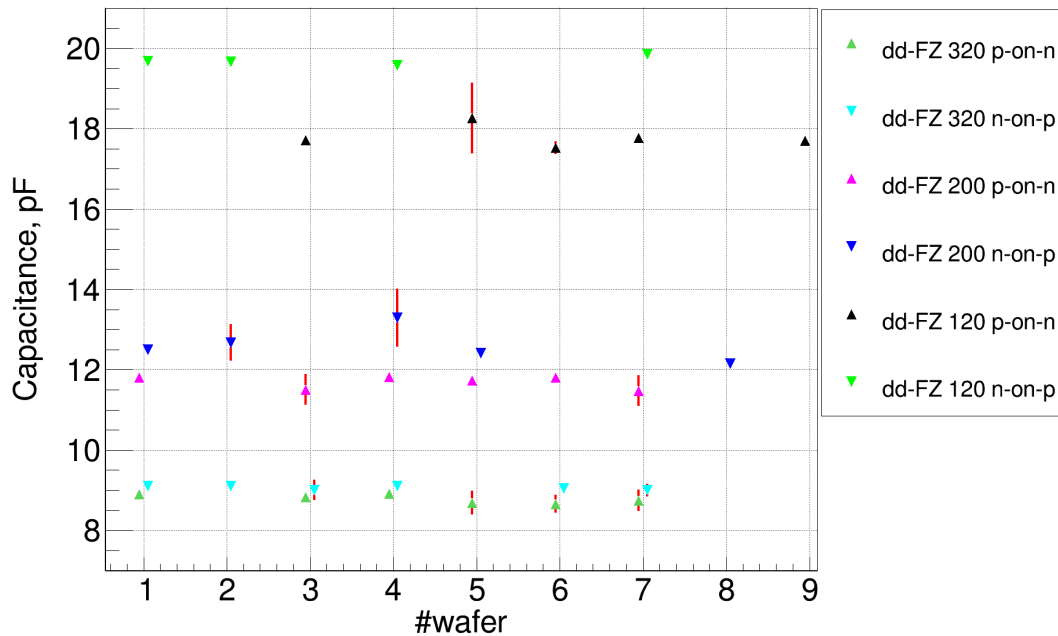


Figure 4.16: CV measurements for all the unirradiated diodes measured for the CMS tracker upgrade at  $-20^{\circ}\text{C}$  and 455 Hz. Data extracted from the CMS tracker upgrade database [63].

- It is observed that at the expected operating bias voltage of the diodes in the calorimeter (600 V), most of them will operate under depleted. This can be easily seen in all the CV curves of the irradiated diodes, where at 600 V the capacitance is still decreasing which means that the diode is not fully depleted yet. Focusing on the dd-FZ 300  $\mu\text{m}$  ones, figure 4.11, it can be seen that only the p-on-n diodes are fully depleted at around 700-800 V; but in the case of the n-on-p ones, only the one irradiated at the lowest fluence shows a similar behaviour, while the rest never reach full depletion in the measured bias voltage range. Comparing them at a given bias voltage (i.e. 600 V), it is observed that the capacitance of the n-on-p diodes is much higher than the capacitance of the p-on-n ones, which means that the depleted volume in the n-on-p diodes is smaller than in the p-on-n ones. This observation is in agreement with the IV measurements, figure 4.4 for the dd-FZ 300  $\mu\text{m}$  diodes. It is possible to see how, for all the fluences, the reverse current in the p-on-n diodes reaches a plateau, while for the n-on-p ones this only happens with the one irradiated at the lowest fluence, in the rest the reverse current keeps increasing.
- In the same way, cross checking the results of the IV and CV characterization for the 100  $\mu\text{m}$  epitaxial diodes, the amplification mechanism seems to be more feasible. In

---

the CV characterization, figure 4.14, it is observed that the capacitance (hence the volume) remains constant approximately over 400 V; while in the IV characterization, figure 4.7, it is observed a clear change in the slope of the curves from concave to convex at around 400 V. This exponential increase of the current over 400 V while the capacitance remains constant, could be explained by means of amplification mechanisms. Moreover, this is why at 600 V and 800 V the points for the epitaxial diodes in figures 4.8 and 4.9 respectively are fairly above the fit. This is a clear example of overestimation of the reverse current in the alpha value calculation.

## 4.4 Transient current technique: charge collection efficiency studies

In order to estimate the charge collected by the diodes after their anticipated lifetime ( $3000 \text{ fb}^{-1}$ ), the charge collection efficiency (CCE) before and after irradiation were compared. For this purpose the Transient Current Technique (TCT) is used. As was mention in the previous chapter, the principle of TCT measurements is to observe the signal created by drifting excess carriers in the silicon detector bulk after illumination with a pulsed laser. In this case, an infrared laser of 1060 nm with a pulse width of 250 ps was used. The diodes were illuminated from the top with an intensity equivalent to about 40 MIPs. It is assumed that the CCE at 40 MIPs is the same as the CCE at 1 MIP, see figure 4.41. The collection time of the carriers is a few nanoseconds. The pulses are amplified using a C2 broadband current amplifier (2 GHz, 40 dB) from CIVIDEC [40]. The amplified pulses are integrated in order to calculate the charge collected.

Measurements were done in steps of 10 V up to 1 kV (400 V for the 50  $\mu\text{m}$  thick devices) at  $-20^\circ\text{C}$ . All the dd-FZ diodes were measured after 10 min at  $60^\circ\text{C}$  of annealing, while the epitaxial diodes were measured after 30 min at  $60^\circ\text{C}$  of annealing. In this case, the guard ring was floating as it has no influence in these measurements because the charge is collected in a small region near to the central position of the diode, far away from possible influences of the edges.

After irradiation CCE, pulse duration and rise time decrease. Figures 4.17, 4.18, 4.19, 4.20 and 4.21 show the CCE for all the diodes. The reference value is the charge collected for the unirradiated diode at 400V, which is normalized to 1 and then the irradiated are scaled

using this value. Figures 4.22, 4.23, 4.24, 4.25 and 4.26 show the TCT transient waveform for all the diodes at a given voltage, 600 V (300 V for the 50  $\mu\text{m}$  thick devices).

Figure 4.27 and figure 4.28 show the charge collected per unit of length (in  $e^-/\mu\text{m}$ ) and the total charge (in  $\text{ke}^-$ ) respectively, extracted from the TCT measurements at 600 V (300 V for the epitaxial 50  $\mu\text{m}$ ) using the thickness given in table 4.2. The charge expected for each thickness before irradiation is plotted in dashed lines. This charge is normalized to the value that is expected to be collected with 1 MIP for each thickness and its value is  $73 e^-/\mu\text{m}$ . In figure 4.27 can be seen clearly that thinner sensors give more charge than thicker ones after high levels of radiation, which is why HGAL plans to use thin sensors at the highest eta region. The red arrow shows the tendency of the 300  $\mu\text{m}$  diodes at higher fluences and the green arrow the tendency of the 200  $\mu\text{m}$  at higher fluences.

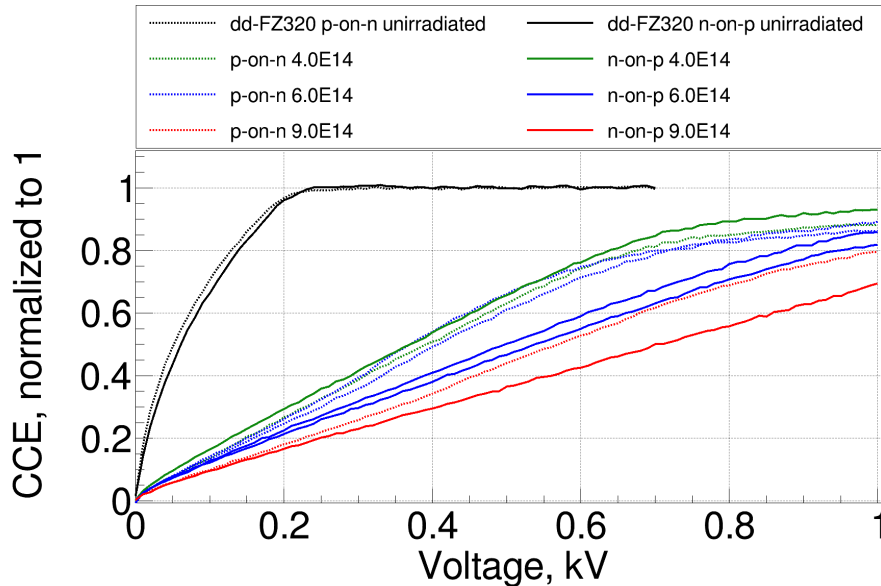


Figure 4.17: Charge collection efficiency for all the dd-FZ 320  $\mu\text{m}$  thickness diodes using an infrared laser and performed at  $-20^\circ\text{C}$ .

It can be observed that the collected charge decreases with the fluence, this result is shown in figures 4.27 and 4.28. With the exception of the dd-FZ 320 diodes, where the n-on-p diodes collect less charge than the p-on-n ones, both bulk types behave similarly. This difference was not expected and needs to be further investigated. A possible explanation is that this difference could be due to a smaller depletion volume in the n-on-p diodes, that would be in agreement with what it was discussed in the previous section 4.3. Nevertheless, it is important to remark that at the highest fluence, in the worst scenario, it is still possible to collect more than  $20 e^-/\mu\text{m}$  at 600 V (around  $30 e^-/\mu\text{m}$  at 800 V). A lower degradation of the Epi diodes

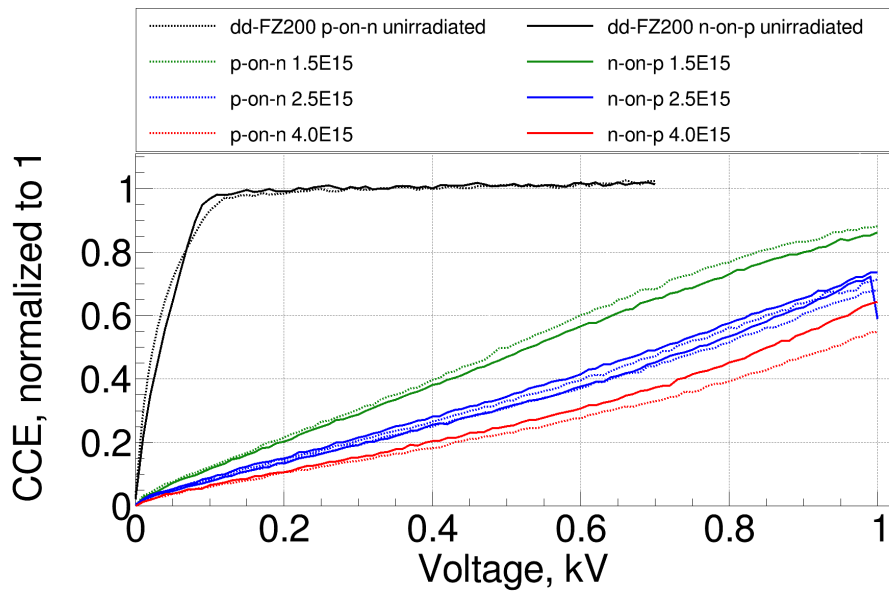


Figure 4.18: Charge collection efficiency for all the dd-FZ 200  $\mu\text{m}$  thickness diodes using an infrared laser and performed at  $-20^\circ\text{C}$ .

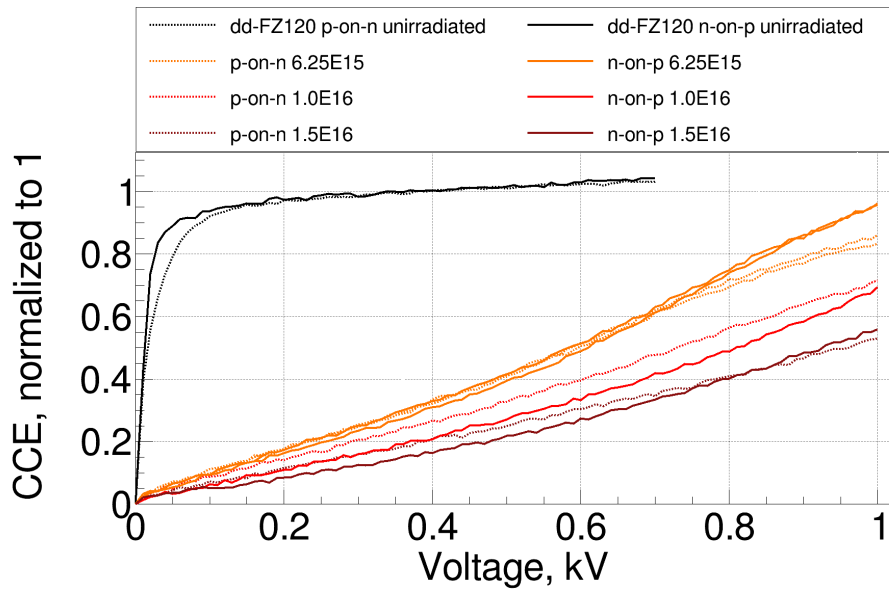


Figure 4.19: Charge collection efficiency measurements for all the dd-FZ 120  $\mu\text{m}$  thickness diodes using an infrared laser and performed at  $-20^\circ\text{C}$ .

in comparison with the dd-FZ is observed, in the worst case it is possible to collect more than  $50 e^-/\mu\text{m}$ . This could be, as was explained in the previous section 4.3, an indication of some amplification mechanisms. These results need to be cross-checked and a new irradiation with more epitaxial diodes is planned.

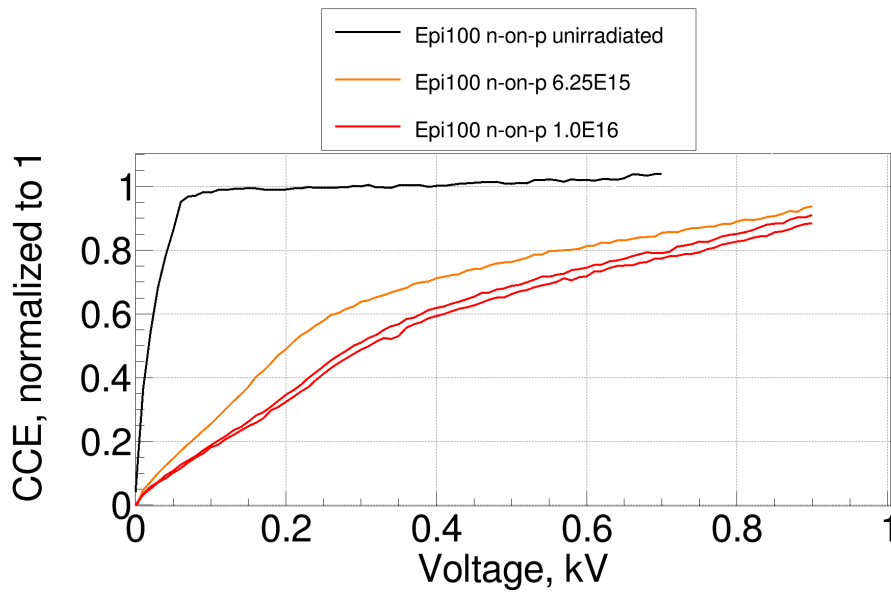


Figure 4.20: Charge collection efficiency measurements for all the Epitaxial 100  $\mu\text{m}$  thickness diodes using an infrared laser and performed at  $-20^\circ\text{C}$ .

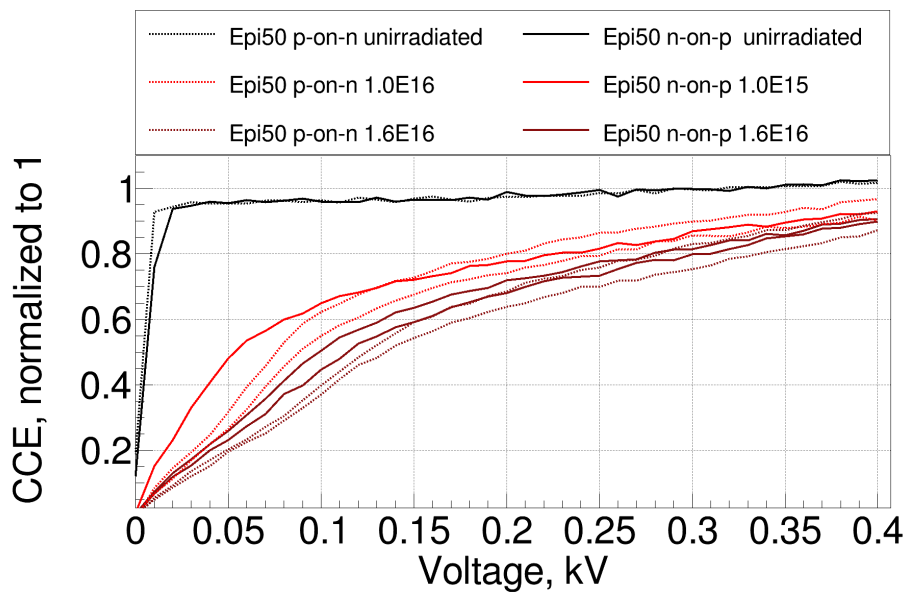


Figure 4.21: Charge collection efficiency measurements for all the Epitaxial 50  $\mu\text{m}$  thickness diodes using an infrared laser and performed at  $-20^\circ\text{C}$ .

#### 4.4.1 Study of the surface homogeneity

For the TCT characterization, several measurements were taken for each diode to avoid possible inhomogeneity over the surface. In the case of the dd-FZ, due to the deep diffuse volume

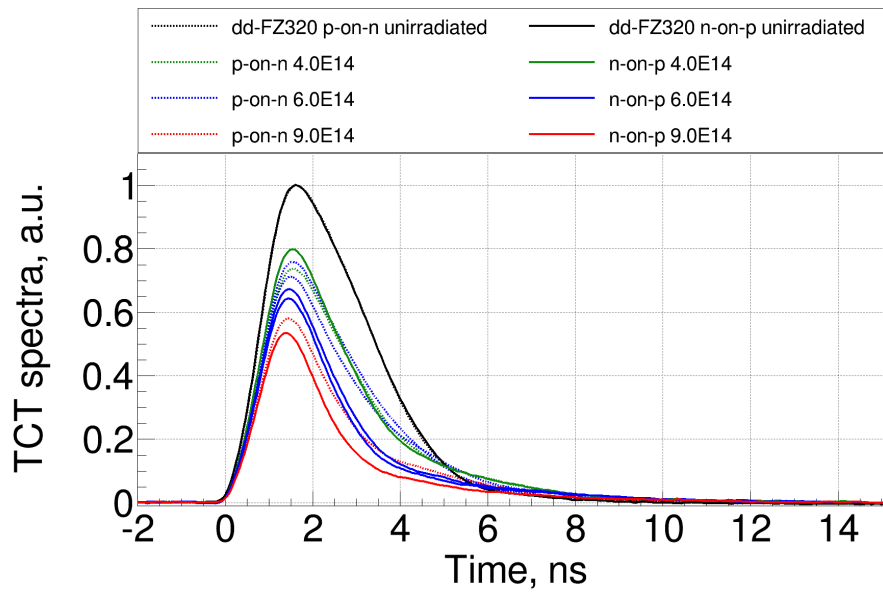


Figure 4.22: TCT spectra at 600 V for all the dd-FZ 320  $\mu\text{m}$  thickness diodes using an infrared laser and performed at  $-20^\circ\text{C}$ .

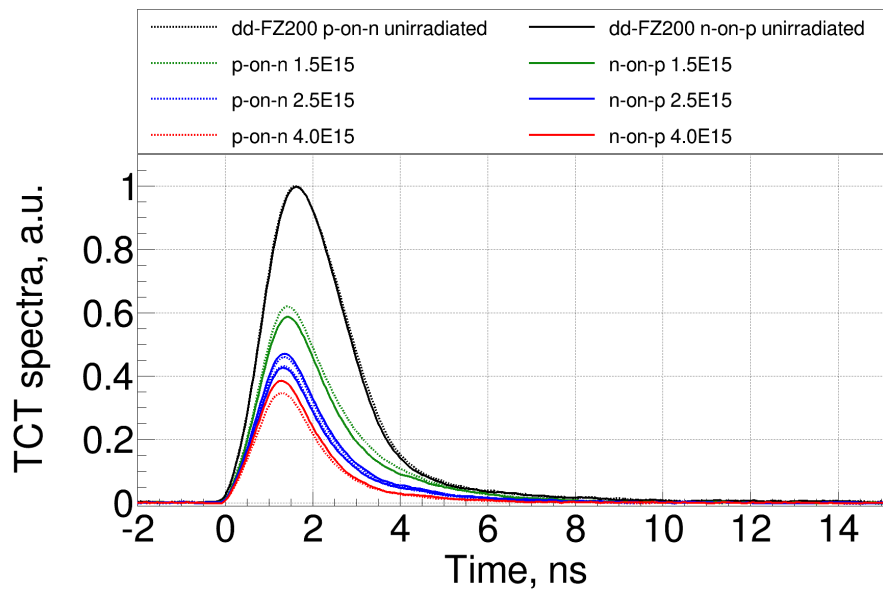


Figure 4.23: TCT spectra at 600 V for all the dd-FZ 200  $\mu\text{m}$  thickness diodes using an infrared laser and performed at  $-20^\circ\text{C}$ .

in the back side of the diodes, the metallic grid was not reachable from the top, see figure 4.29. The homogeneity on the surface of the diode was very good, and usually the illumination was done in several points around the center of the diodes. On the other hand, the metallic grid was reachable in the epitaxial diodes, see figure 4.30. The metallic grid reflects

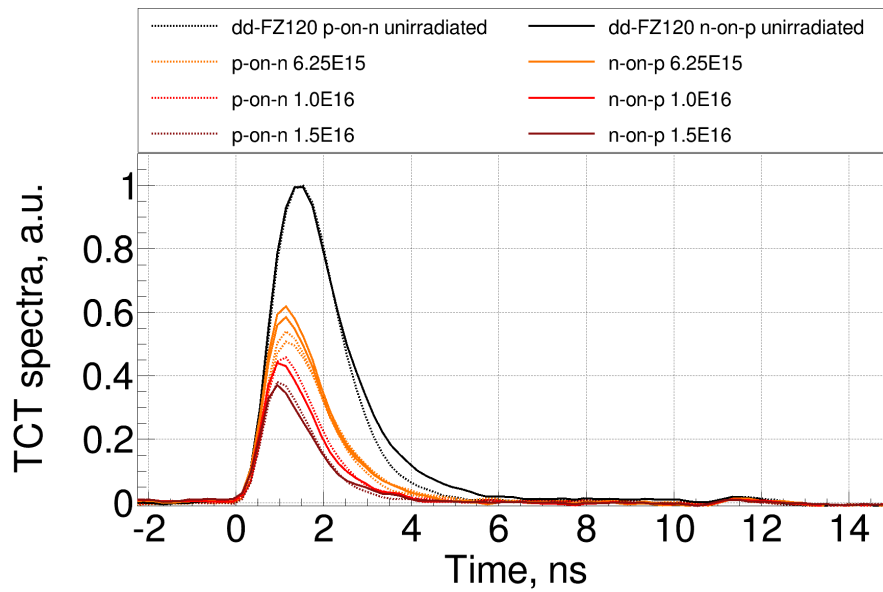


Figure 4.24: TCT spectra at 600 V for all the dd-FZ 120  $\mu\text{m}$  thickness diodes using an infrared laser and performed at  $-20^\circ\text{C}$ .

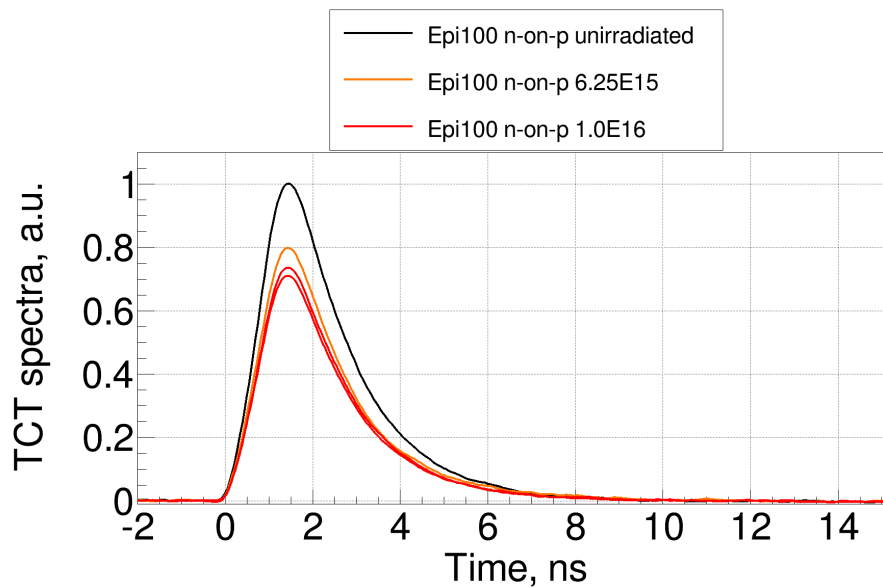


Figure 4.25: TCT spectra at 600 V for all the Epitaxial 100  $\mu\text{m}$  thickness diodes using an infrared laser and performed at  $-20^\circ\text{C}$ .

part of the light coming from the infrared laser increasing the signal in this part of the diode. For a proper TCT characterization, the illumination has to be done in the squares opening on the back plane of the diodes, see figure 4.2. In this part of the diode there are no reflections, thus the measurements are more realistic. The position of the square opening change from

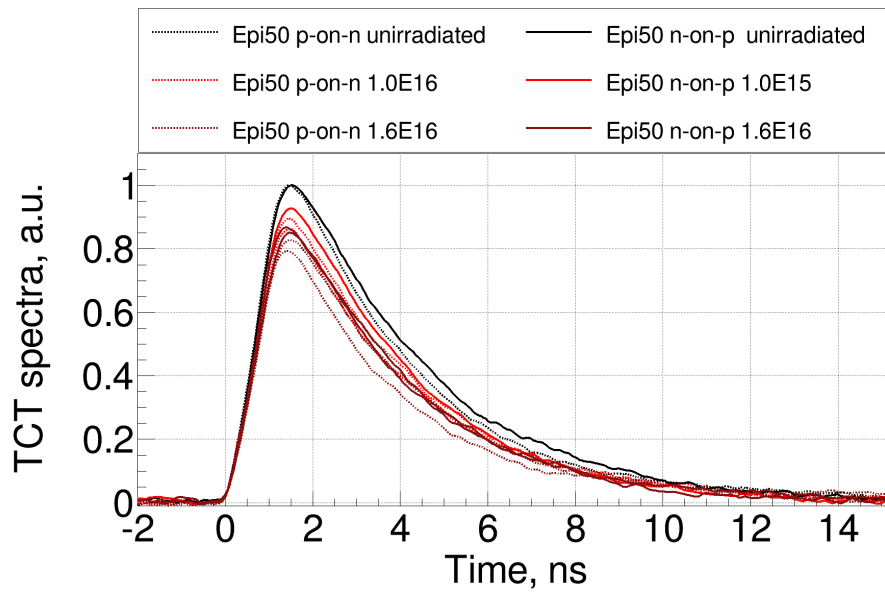


Figure 4.26: TCT spectra at 300 V for all the Epitaxial  $50 \mu\text{m}$  thickness diodes using an infrared laser and performed at  $-20^\circ\text{C}$ .

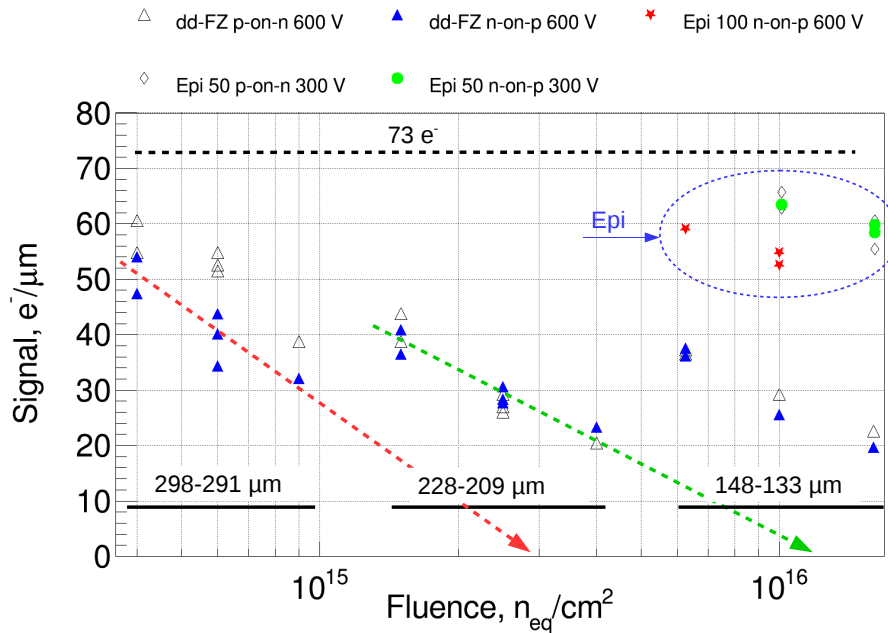


Figure 4.27: Signal ( $e^-/\mu\text{m}$ ) extracted from the TCT measurements for the different diodes at 600 V, 300 V for the  $50\text{-}\mu\text{m}$  epitaxial silicon.

one diode to another, so for every diode is needed to find them before starting with the TCT

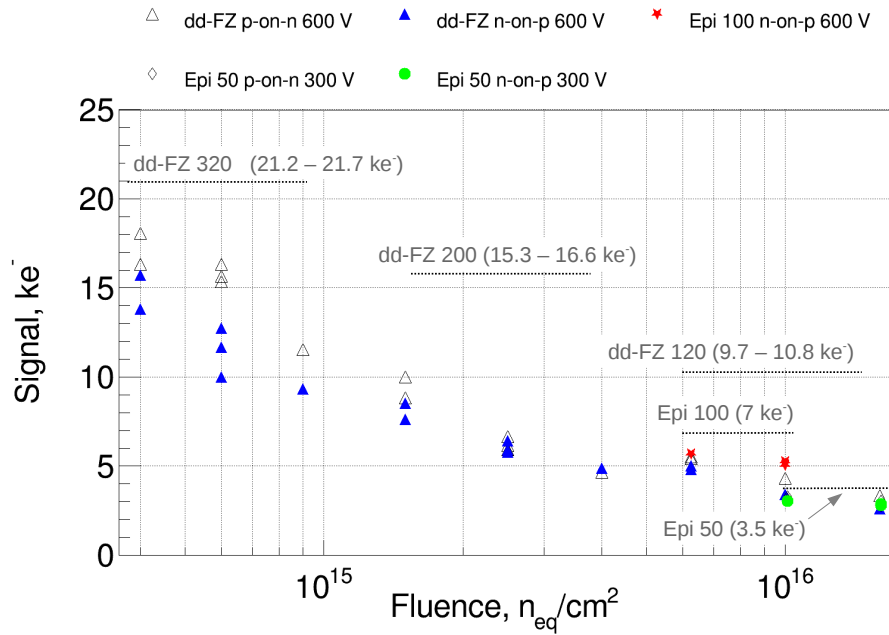


Figure 4.28: Signal (ke<sup>-</sup>) extracted from the TCT measurements for the different diodes at 600 V, 300 V for the 50- $\mu$ m epitaxial silicon. In dotted lines the charge expected for the unirradiated diode is shown. Inside brackets the charge expected for the n-on-p and p-on-n dd-FZ diodes respectively.

characterization.

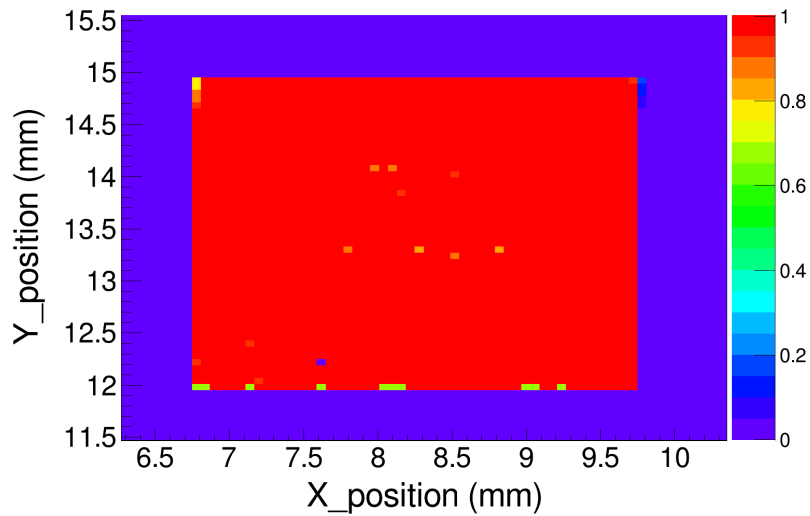


Figure 4.29: Surface scan with infrared laser top illumination on the dd-FZ diodes. An unirradiated 300  $\mu$ m n-on-p measured at 20°C is shown in this plot.

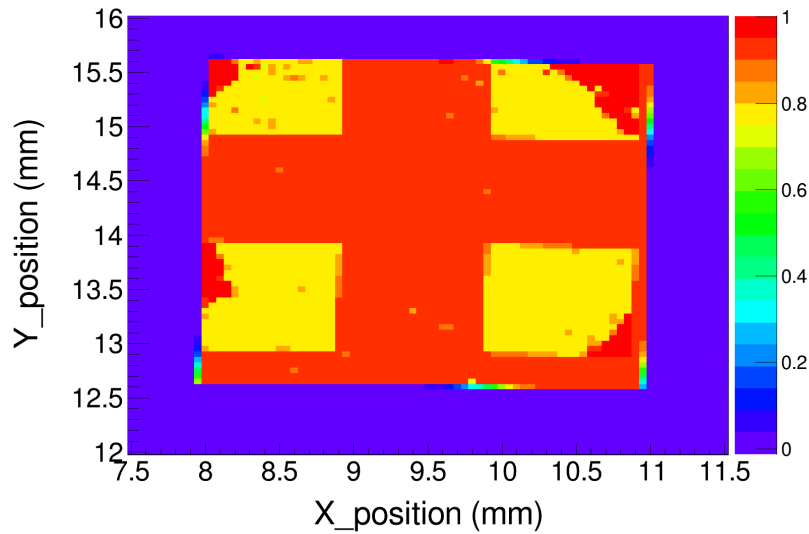


Figure 4.30: Surface scan with infrared laser top illumination on the epitaxial diodes. An unirradiated  $100\ \mu\text{m}$  n-on-p measured at  $20^\circ\text{C}$  is shown in this plot.

#### 4.4.2 Reproducibility of the measurements

A study of the reproducibility of the TCT measurements in the set-up has been performed. The dd-FZ  $200\ \mu\text{m}$  thickness diodes were used for this propose. The results of this study are shown in figure 4.31. IR laser and top illuminations was used. One first set of measurements were done with the n-on-p (red continuous lines) and p-on-n (magenta dotted lines). Two measurements were taken per diode at different coordinates and no differences were observed. After this first set of measurements, all the diodes were unmounted from the pcbs. Then weeks later they were glued and wire-bonded again on the the pcbs and the same set of measurements were repeated. The power of the laser remained the same. The new measurements with the n-on-p are plotted in blue lines while the p-on-n in green dotted lines. Again two measurements were taken per diode. No differences were observed between these new measurements and the ones performed weeks before. Notice that for the fluence of  $2.5 \times 10^{15}\ \text{n}_{eq}/\text{cm}^2$  there are measurements from two diodes (two different group of lines) while for the rest there is only one diode per fluence.

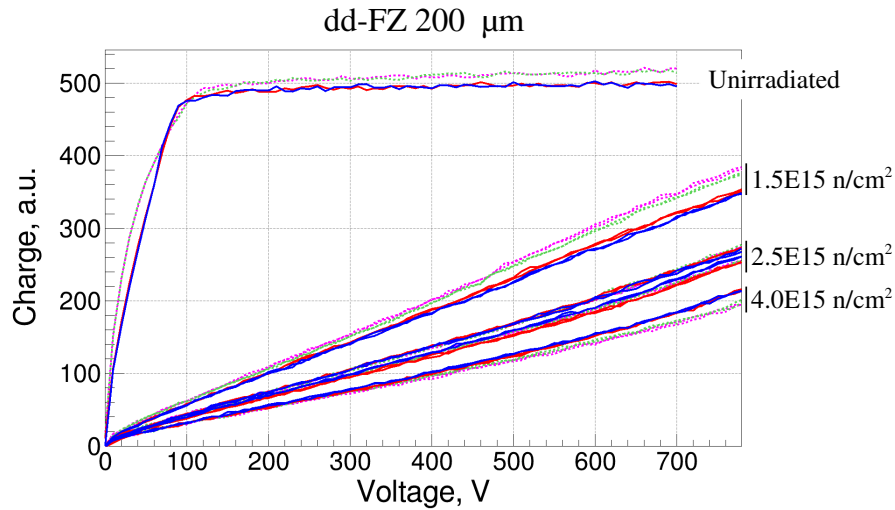


Figure 4.31: Reproducibility of the TCT measurements using IR laser top illumination. Two set of measurements were done with weeks of difference with the dd-FZ 200  $\mu\text{m}$  diodes (dotted lines p-on-n, continuous lines n-on-p). Green and blue taken weeks after the red and magenta.

#### 4.4.3 Thickness measurement using edge-TCT technique

Other interesting result that was obtained during the TCT characterization was the measurement of the thickness of one unirradiated dd-FZ 320 n-on-p  $\mu\text{m}$  diode using the edge-TCT technique [39]. In this measurement the diode was illuminated from one side and while keeping fix the horizontal coordinates (X and Y) the the vertical coordinate (Z) was moving in steps of 2  $\mu\text{m}$  from the bottom to the top. The diode was fully depleted (biased at 700 V) and measured at room temperature. In figure 4.32 the charge collected as a function of the Z coordinate is shown. When the IR laser illuminates outside of the depleted volume the charge collected is zero while inside the depleted volume the charge collected is maximum. The FWHM of the resulting pulse gives the depleted thickness of the diode. The results (287  $\mu\text{m}$ ) is in agreement with the one obtained in the CV characterization (291  $\mu\text{m}$ ), see table 4.2.

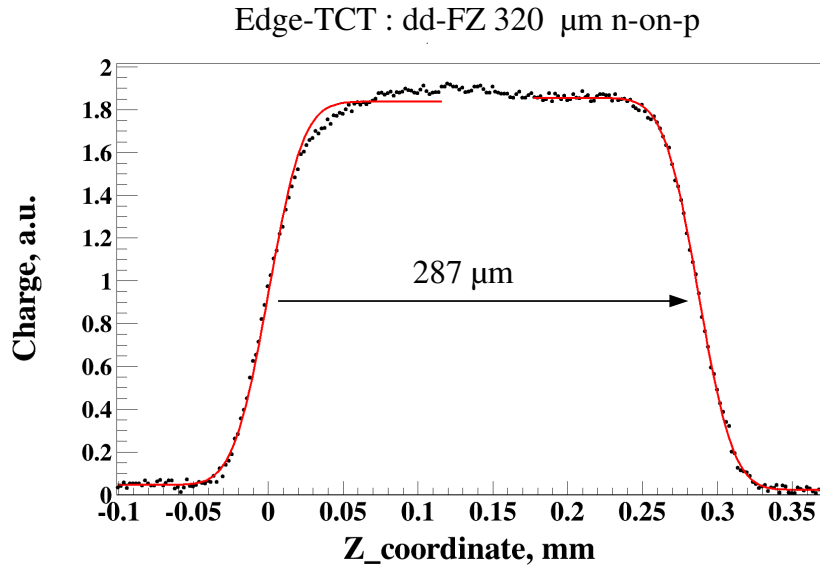


Figure 4.32: Edge-TCT measurement done in a fully depleted unirradiated dd-FZ 320 n-on-p  $\mu\text{m}$  diode. It is possible to extract the depleted thickness of the diodes, 287  $\mu\text{m}$  in this case.

## 4.5 Radioactive source characterization

The purpose of the radioactive source characterization is to evaluate with MIPs the parameters of the Landau distribution after irradiation. Measurements were conducted using a  $^{90}\text{Sr}$  source and performed at two different temperatures,  $-20^\circ\text{C}$  and  $-30^\circ\text{C}$ . No significant difference was observed. The sensors were measured at different bias voltages from 0 V to 1 kV (400 V for the 50  $\mu\text{m}$  Epi). As mentioned in the previous chapter, a photomultiplier was used in conjunction with a scintillator to detect the electrons; and the signal was measured with a Cx-L spectroscopic amplifier from CIVIDEC [40], see section 3.3.1. It was not possible to measure the irradiated p-on-n diodes due to the high noise that appeared during the biasing. This problem did not affect the unirradiated n-on-p and p-on-n or the irradiated n-on-p. However, at the highest fluences:  $1.0 \times 10^{16} \text{ n}_{eq}/\text{cm}^2$  and  $1.6 \times 10^{16} \text{ n}_{eq}/\text{cm}^2$ , the signal was very low and it was complicated to distinguish it from the noise efficiently.

A convoluted Landau and Gaussian fitting function was used. The Gaussian parameter of the distribution (Gsigma) was not fixed to the measured electronic noise [64]. The rest of

the parameters were extracted from the Landau function: most probable value (MPV) and width of the Landau. The Gaussian contribution in the charge depositions was higher than the measured electronic noise, given in tables 4.4 and 4.5, which implies that there are more Gaussian components that are not coming from the electronic noise, see section 3.3.3.

Figures 4.33 and 4.34 shown the charge distribution of all the unirradiated diodes tested at 400 V and  $-20^{\circ}\text{C}$  ( $-30^{\circ}\text{C}$  for the epitaxial). The histograms were normalized in order to compare them, the area of the langau function is 1 in all the cases. In table 4.4 are shown the main parameters after the fitting in the same conditions. As was expected, for the thicker diodes the MPV and the width are higher than for the thinner ones, while the noise is higher for the thinner ones as they have a higher capacitance.

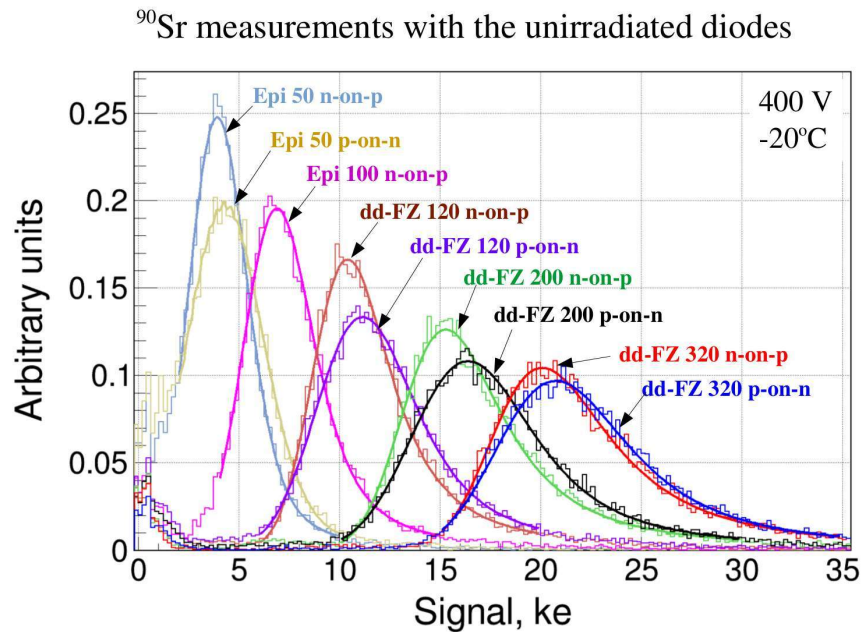


Figure 4.33: Charge distribution measured with  $^{90}\text{Sr}$  for all the unirradiated diodes at 400 V and  $-20^{\circ}\text{C}$  ( $-30^{\circ}\text{C}$  for the epitaxial). Normalized distributions.

The MPV measured for these sensors must be proportional to the thicknesses calculated from the CV characterization. These values are shown in table 4.4, where all the diodes are fully depleted at 400 V. In figure 4.35 are compared the ratios between the thicknesses and charge collected with the radioactive source. As a reference was taken the thicker diode dd-FZ 320  $\mu\text{m}$  p-on-n. There is a good agreement between the two ratios.

Results for the irradiated diodes are shown in figures 4.36, 4.37, 4.38, 4.39 and 4.40 for the 320, 200, 120, 100 and 50  $\mu\text{m}$  n-on-p diodes respectively. The charge distribution

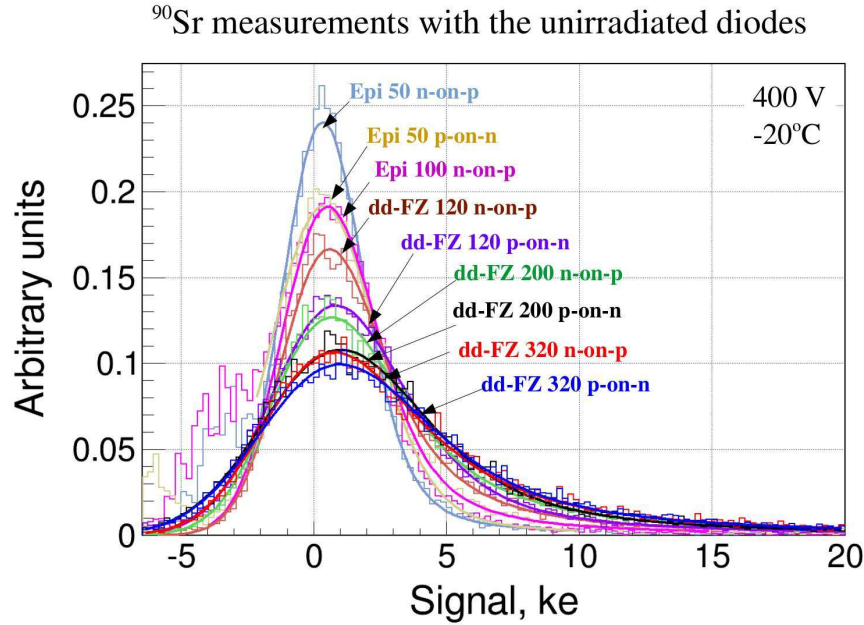


Figure 4.34: Charge distribution measured with <sup>90</sup>Sr for all the unirradiated diodes at 400 V and  $-20^{\circ}\text{C}$  ( $-30^{\circ}\text{C}$  for the epitaxial). For a better comparison all distribution were normalized and shifted to MPV = 0.

Type	Thickness, $\mu\text{m}$	MPV, $e^-$	Width, $e^-$	Noise, $e^-$	SNR
dd-FZ p-on-n	298	19920	1346	669	29.7
dd-FZ n-on-p	291	19480	1396	671	29
dd-FZ p-on-n	228	15530	1047	678	22.9
dd-FZ n-on-p	209	14700	1071	681	21.6
dd-FZ p-on-n	148	1043	802	687	15.2
dd-FZ n-on-p	143	9892	744	689	14.4
Epi n-on-p	96	6376	468	817	7.8
Epi p-on-n	50	3845	195	929	4.1
Epi n-on-p	48	3538	245	916	3.9

Table 4.4: Most probable value (MPV), width of the Landau fitting function, Gaussian noise and signal-to-noise ratio (SNR) for all the unirradiated diodes at 400 V and  $-20^{\circ}\text{C}$  ( $-30^{\circ}\text{C}$  for the epitaxial).

(fitted with a Landau-Gaussian convolution) at 600 V (300 V for the 50  $\mu\text{m}$  ones) and  $-20^{\circ}\text{C}$  ( $-30^{\circ}\text{C}$  for the epitaxial) is shown. The two main changes observed after irradiation are the reduction of the Landau MPV and the narrowing of the Landau width with fluence. The MPV

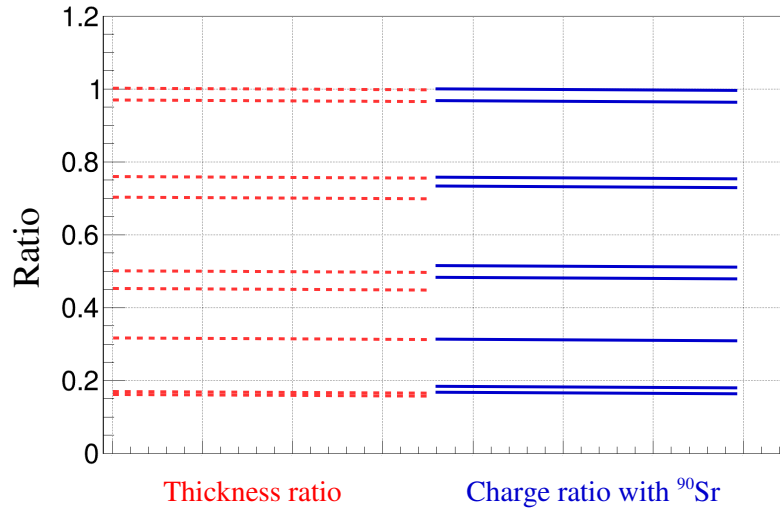


Figure 4.35: Comparison between the thickness ratio (see table 4.2) and the charger ratio measured with the  $^{90}\text{Sr}$  (MPV) for the unirradiated diodes. The charge scales with the thickness. The thicker diode was taken as reference (dd-FZ 320  $\mu\text{m}$  p-on-n).

and width of the fitting are shown in table 4.5.

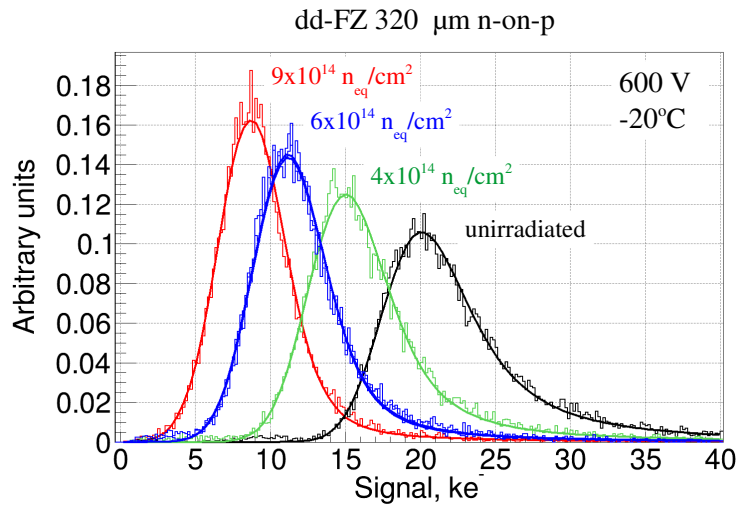


Figure 4.36: Charge distribution measured with  $^{90}\text{Sr}$  for all dd-FZ 320  $\mu\text{m}$  n-on-p diodes at 600 V and  $-20^\circ\text{C}$ . Normalized distributions.

Type	fluence, $\mu\text{m}$	MPV, $e^-$	Width, $e^-$	Noise, $e^-$	SNR
dd-FZ 320	$4.0 \times 10^{14}$	14220	795	1080	13.1
	$6.0 \times 10^{14}$	10480	496	1190	8.8
	$6.0 \times 10^{14}$	10470	538	1180	8.9
	$9.0 \times 10^{14}$	8140	315	1160	7
dd-FZ 200	$1.5 \times 10^{15}$	7240	316	1370	5.3
	$2.5 \times 10^{15}$	5500	231	1480	3.7
	$2.5 \times 10^{15}$	5950	226	1460	4.1
	$4.0 \times 10^{15}$	4910	170	1700	2.9
dd-FZ 120	$6.25 \times 10^{15}$	4720	310	2020	2.3
	$6.25 \times 10^{15}$	4780	305	2110	2.3
	$1.0 \times 10^{16}$	3600	200	2060	1.8
	$1.6 \times 10^{16}$	3170	132	2020	1.6
Epi 100	$6.25 \times 10^{15}$	5280	341	1520	3.5
	$1.0 \times 10^{16}$	5150	282	1710	3.0
	$1.6 \times 10^{16}$	5140	251	1730	3.0
Epi 50	$1.0 \times 10^{16}$	3770	260	1450	2.6
	$1.6 \times 10^{16}$	4040	194	1730	2.3
	$1.6 \times 10^{16}$	4000	231	1730	2.3

Table 4.5: Most probable value (MPV) and width of the landau fitting function for all the irradiated n-on-p diodes at 600 V (300 V for the 50  $\mu\text{m}$  ones) and  $-20^\circ\text{C}$  ( $-30^\circ\text{C}$  for the epitaxial).

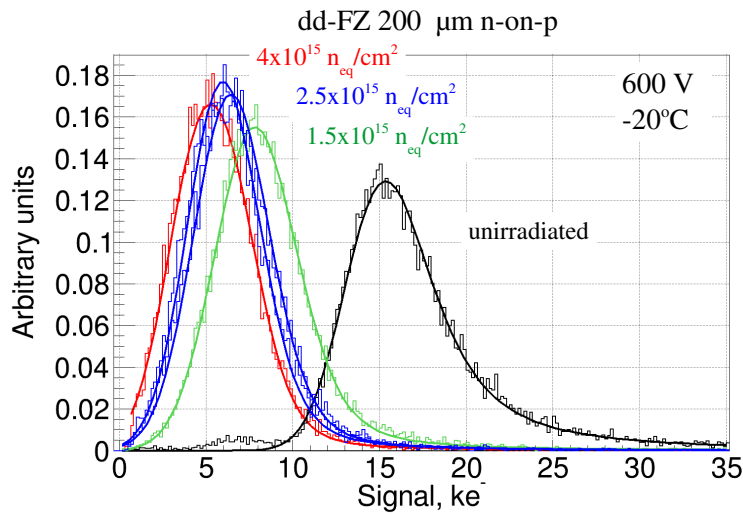


Figure 4.37: Charge distribution measured with  $^{90}\text{Sr}$  for all dd-FZ 200  $\mu\text{m}$  n-on-p diodes at 600 V and  $-20^\circ\text{C}$ . Normalized distributions.

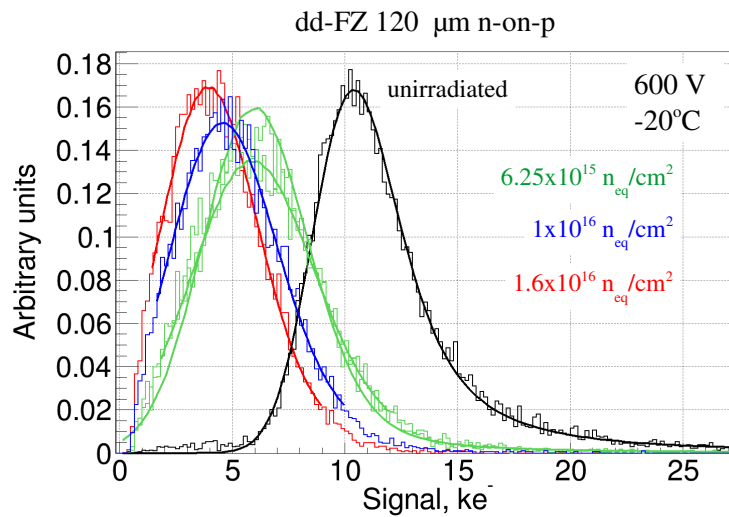


Figure 4.38: Charge distribution measured with  $^{90}\text{Sr}$  for all dd-FZ 120  $\mu\text{m}$  n-on-p diodes at 600 V and  $-20^\circ\text{C}$ . Normalized distributions.

It is possible to compare the CCE measured with the  $^{90}\text{Sr}$  source (1 MIP) at  $-20^\circ\text{C}$  with the CCE measured with the IR laser (about 40 MIPs) at  $-20^\circ\text{C}$ . Figure 4.41 shows that there is a good agreement between the laser and the  $^{90}\text{Sr}$  source measurements with the exception

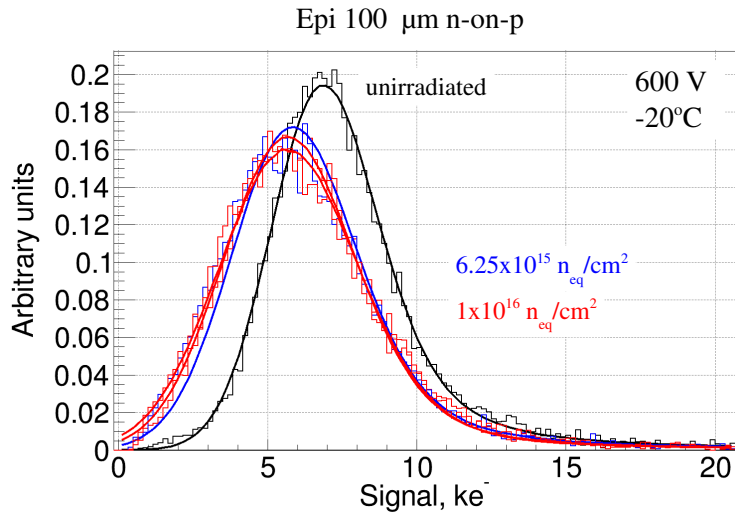


Figure 4.39: Charge distribution measured with  $^{90}\text{Sr}$  for all Epi  $100\ \mu\text{m}$  n-on-p diodes at 600 V and  $-30^\circ\text{C}$ . Normalized distributions.

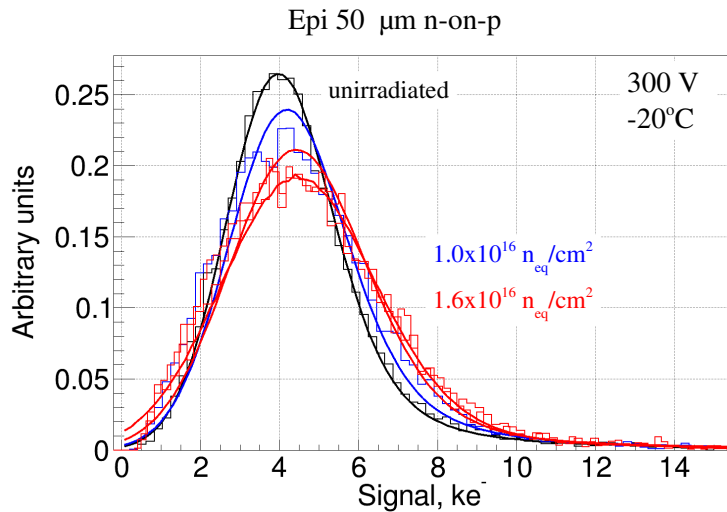


Figure 4.40: Charge distribution measured with  $^{90}\text{Sr}$  for all Epi  $50\ \mu\text{m}$  n-on-p diodes at 300 V and  $-30^\circ\text{C}$ . Normalized distributions.

of the highly irradiated diodes, where the laser signal is slightly smaller. This could be due to the fact that irradiation changes the properties of the silicon and the absorption, reflection and refraction index in highly irradiated diodes may not be the same as in the non irradiated

ones. The signal for the unirradiated diodes was set with the measurements done with the  $^{90}\text{Sr}$  source, unlike in figure 4.28, where the reference value of  $73\text{ e}^-/\mu\text{m}$  was used.

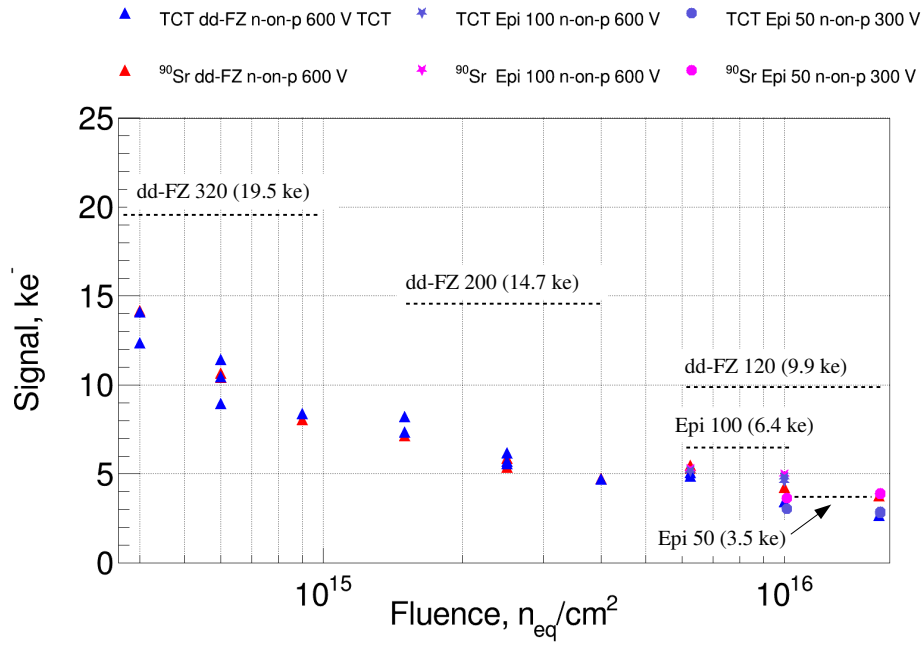


Figure 4.41: Comparison between the signal ( $\text{ke}^-$ ) extracted from the TCT and the  $^{90}\text{Sr}$  measurements for the different diodes at 600 V, 300 V for the 50- $\mu\text{m}$  epitaxial silicon.

Summarizing, all unirradiated diodes were measured with the  $^{90}\text{Sr}$  with a signal-to-noise ratio (SNR) between 18, for the thicker diodes, and 5, for the thinner ones. The SNR decreases with irradiation making it difficult to get a signal from the highly irradiated diodes. The signal measured in the unirradiated diodes with the  $^{90}\text{Sr}$  source (MPV) was in between about  $20\text{ ke}^-$  (for the dd-FZ 320 p-on-n) and about  $3.5\text{ ke}^-$  (for the Epi 50 p-on-n). As it was previously stated, the highly irradiated diodes presented a very low SNR. In particular for the irradiated 50- $\mu\text{m}$  ones, the SNR was between 2 and 3. Nevertheless, the measurements done are in agreement with the TCT measurements, as shown in figure 4.41.



## Chapter 5

# Timing performance of deep diffused Float Zone diodes

## 5.1 Introduction

For understanding the timing capability of deep-diffused float-zone (dd-FZ) diodes several test beams were carried out at the SPS H2 line at CERN [46]. The first one was done in July 2015 only with the unirradiated dd-FZ diodes, and then the study was completed with two more, in April and June 2016, in which the dd-FZ irradiated diodes were included. The epitaxial diodes were not included in none of them. The set-ups used with the unirradiated and irradiated diodes differ a bit, mainly due to the cooling needed in the last case. The diodes have been exposed to high energy muons and electrons during the test beams in order to study timing capabilities when traversed by multiple simultaneous minimum ionizing particles (MIPs).

As mention in the introduction, the dramatic increase of the pileup per beam crossings in the experiments at the HL-LHC will make the even reconstruction a very challenging task. With a event pileup up to 200 per beam crossing, current detectors will show limitations in the reliance on purely spatial information to resolve interactions [13, 65] and associate particles to vertices. In addition, the calorimeter performance in terms of energy measurement and particle identification, will be deteriorated by the random overlap of energy deposits from neutral particles, which can not be associated via a track to any vertex. Thus, precision time measurement of the energy deposits could provide an additional mean to resolve interactions

---

by exploiting the spread in the time domain of the collision vertices predicted to be about 150 ps RMS, within the 25 ns bunch crossing structure of the colliding beams at the HL-LHC [66].

## 5.2 Experimental arrangements

- The set-up for the unirradiated dd-FZ diodes test beam done in July 2015 is shown in figure 5.1. Two silicon sensors of each thickness and polarity were measured at the same time. Micro Channel Plates (MCP), viewing a Cherenkov radiator, were used as a time reference providing a precise timing reference of about 20 ps. A scintillator counter of  $2 \times 2 \text{ cm}^2$  was used for the trigger. A set of wire chambers were used to estimate the impact position of the particles on the diodes with a resolution of about one millimeter. Several absorber sheets of lead with different thicknesses were placed between the MCP and the set of diodes to investigate its multi-MIPs response. The electrical signals coming from the diodes were amplified by a C2 broadband current amplifier (2 GHz, 40 dB) from CIVIDEC [40]. The readout of the diodes was done with a CAEN V1742 fast digitizer (5GS/s) with an analogue bandwidth of 500 MHz. The time-pickoff algorithm was applied off-line, there was not timing discriminator included in the set-up. The signals from MCP and the event trigger were also fed to the same digitizer unit in order to remove trigger jitter off-line. The intrinsic timing jitter of the digitizer was about 5 ps.

For the majority of the measurements 150 GeV muons and 50 GeV electrons were used. The beam particles were usually a few thousand per spill. Each spill lasted about 2.5 seconds and was repeated approximately every 30 second. The FWHM of the beam was about 1 cm in horizontal and vertical directions. Despite the fact that both bulk types were tested in this test beam, only for the n-on-p was collected enough data. The diodes were biased at 600 V and tested at room temperature.

- For the test beams with the irradiated diodes performed in April and June 2016, the same infrastructure was used as with the unirradiated test beam, with the only exception of the MCP for reference; in this case, the unirradiated diodes were used as a time reference. The main changes in the set-up were due to the fact that the irradiated diodes need to be measured at temperatures below  $-20^\circ\text{C}$ .

The set-up was placed inside a cold box. This box, called Vienna box [68], was origi-

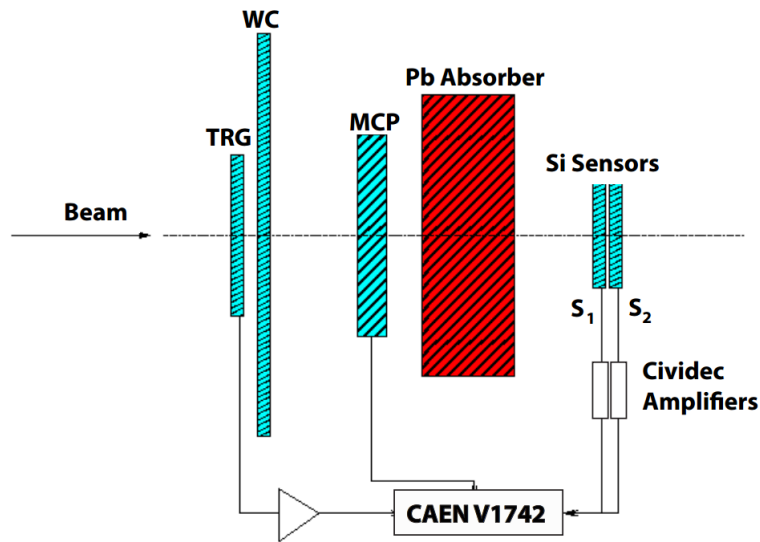


Figure 5.1: The schematic of the layout displays the main components and the readout scheme [67].

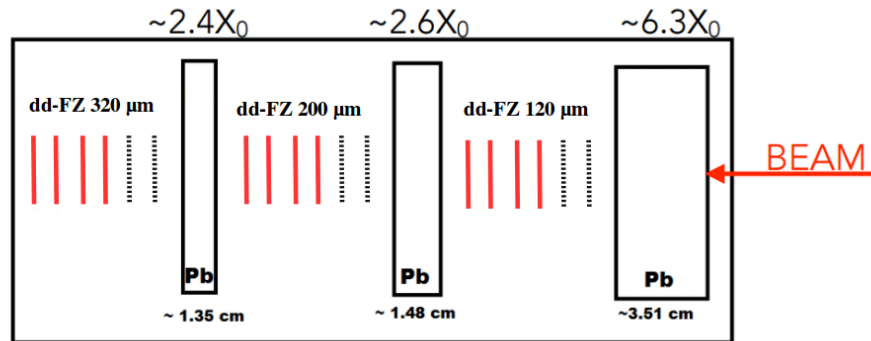


Figure 5.2: Schematic of the set-up. Three set of six diodes each, were placed inside the box at the same time. The unirradiated diodes are represented in black dotted lines and the irradiated in red lines. Three set of Pb absorber were placed in front of each set.

nal designed as a CMS long-term module test chamber in the test beams. The chamber provides both temperature and humidity control and additionally shields the interior from light. Using this box it was possible to cold down the diodes down to  $-30^{\circ}\text{C}$ . The set-up had a limited flexibility due to time constraint (up to 5 hours for a full thermal cycle). For this reason, the set-up was optimized for holding inside the maximum number of diodes at the same time to minimize cooling cycles. One set of six diodes of the same thickness and same polarity was measured at the same time. Each set consisted of

---

two unirradiated diodes used as a time reference followed by four irradiated diodes in increasing order of fluence. Inside the box were placed three sets, in this order: first the dd-FZ 120, followed by the dd-FZ 200 and ending the dd-FZ 320. In front of each set was placed a Pb absorber of different radiation length in order to produce large signals in the furthest diodes. An schematic of the set-up is shown in figure 5.2, and one set of diodes and the cold box are shown in figure 5.3. The diodes were glued in the same pcb used for the TCT measurements in the lab, see figure 3.11.

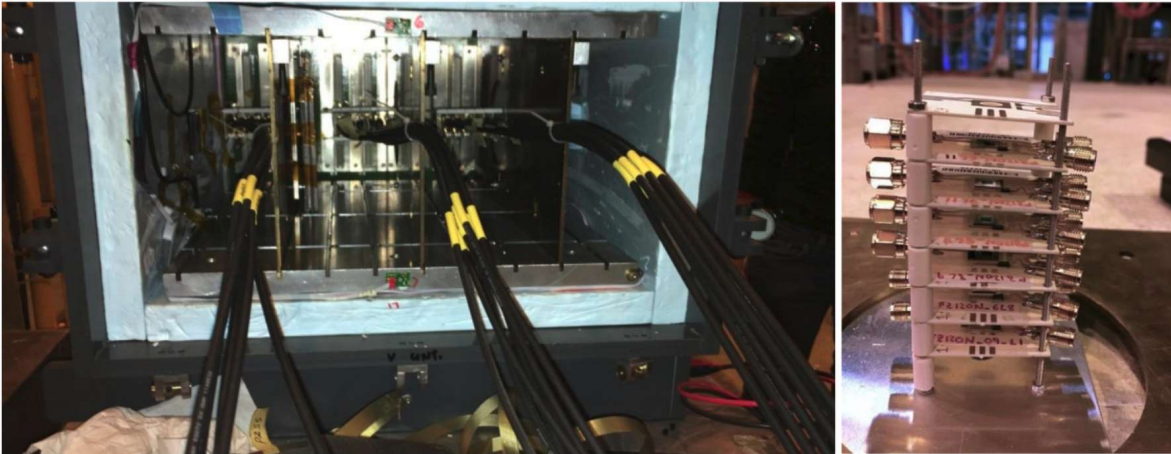


Figure 5.3: Cold box with the three sets of diodes inside (left). One set of diodes mounted in a plate ready to be placed inside the box (right). The distance between diodes was 1 cm.

## 5.3 Analysis

### 5.3.1 MIP calibration

The response of the three different thicknesses to a single MIP was measured in the first test beam. A 50 GeV electron beam without the lead plate absorber was used to perform this characterization. These results were found to be in agreement with the ones obtained using a 150 GeV muon beam for the 200  $\mu\text{m}$  diodes. Events were selected with a signal from the MCP and from the second diode. The condition of having a signal in the second diode ensured that most tracks passed through the first diode whose response was being measured. The signal distribution from the first diode included contributions from zero (electronic noise) and single-track (one MIP) event, as well as from a small number of events with three charged tracks (three MIPs) where a photon emitted by the interacting initial electron produce an

electron-positron pair. This spectrum was modeled with a linear sum of a Gaussian and two Landau distributions convolved with a Gaussian distribution, representing contributions from one MIP and three MIPs. The most probable value of the Landau distribution establishes the MIP measurement. The precision of the measurement was limited by the amount of data and by the systematic uncertainties related to the noise correlation between the two sensors. The MIP response of the three thicknesses is compared in figure 5.4. The signal strength scales nearly linearly with the depletion zone depth, as expected. The MPV (solid black squares) for a MIP for each diode is compared as well as for the signal-to-noise ratios (open red circles). The signal-to-noise ratio measured here is much lower than the one measured with the  $^{90}\text{Sr}$  source in the previous chapter due to the fact that the amplifiers used are different.

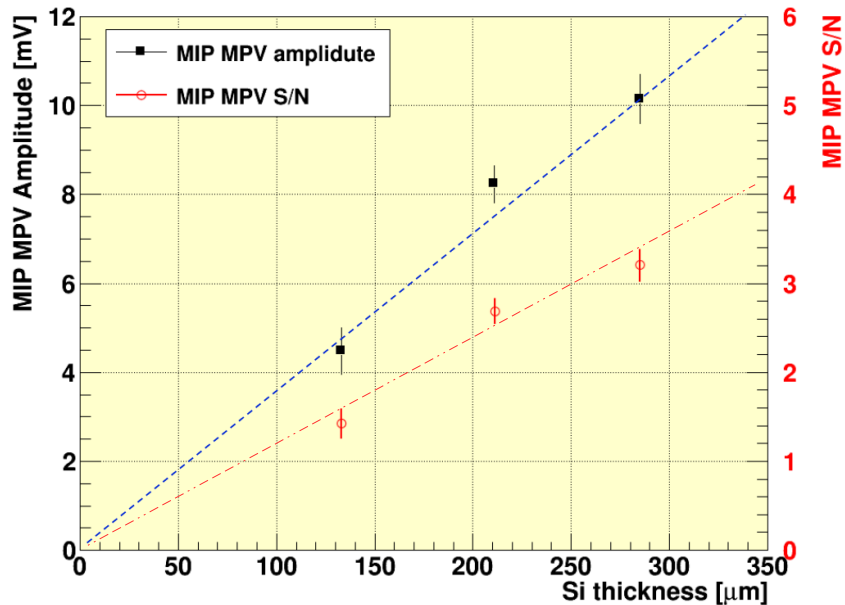


Figure 5.4: Comparison of the diodes response to MIPs as a function of their thickness. In red circles, the signal-to-noise ratio for single MIP are given (right scale) [67].

With the irradiated diodes the response to a single MIP was not possible to be measured during the test beam. The low amount of data collected in this configuration and the low SNR at this working point made very difficult this task. However, in order to estimate the signal amplitude in MIPs for the irradiated diodes, an extrapolation from the response measured with the unirradiated in the first beam test was done. For this extrapolation the signal degra-

---

ation, in terms of amplitude, measured in the TCT characterization was used, see figures 4.17, 4.18 and 4.19.

### 5.3.2 Multi MIP Signal study

In order to evaluate the linearity of the response of the diodes to multiple MIPs, lead absorber were placed in front of the diodes, producing electromagnetic showers. In the case of the first test beam with the unirradiated diodes, two radiation lengths of lead were placed with a 50 GeV electron beam. The diodes were biased at 600 V and measured at room temperature. In the case of the irradiated a 100 GeV and 150 GeV electron beam with lead plates as absorber of different radiation lengths were used. All diodes were tested at temperatures close to  $-30^{\circ}\text{C}$  and a bias voltage of 600 V.

Once separated single-MIP response from the background, the next step was to measure the diodes response to multiple MIPs. It was considered a signal from one to N tracks simultaneously passing through the diodes, where N is small enough to distinguish signals from different track multiplicities.

In the absence of independent information providing the number of charged particles passing through the sensor, this study was particularly well-suited for the set-up used. Thus, it was analyzed the spectrum containing events with different track multiplicities. The observed spectrum was modeled with an analytic function and then the linearity of the response was evaluated from the parameters of this function. This procedure was also validated with a GEANT4 simulation.

The signal distribution was fitted with an analytic function with multiple components, see figure 5.5. Each component comprised a Landau distribution to describe ionization loss by a charged particle in a thin silicon layer convolved with a Gaussian distribution to model electronics noise.  $N + 1$  components were added linearly to describe a spectrum with track multiplicities ranging from one to N. The pedestal component of the distribution (no charged particle going through the sensor) was modeled by a Gaussian distribution, and its width was used to constrain the Gaussian component in the MIPs signals. The only constraint in the fitting procedure was that the widths of the individual distributions were limited to a range. All other parameters were left free in the minimization process.

As a result the signal strength scales nearly linearly with the depletion zone depth, as

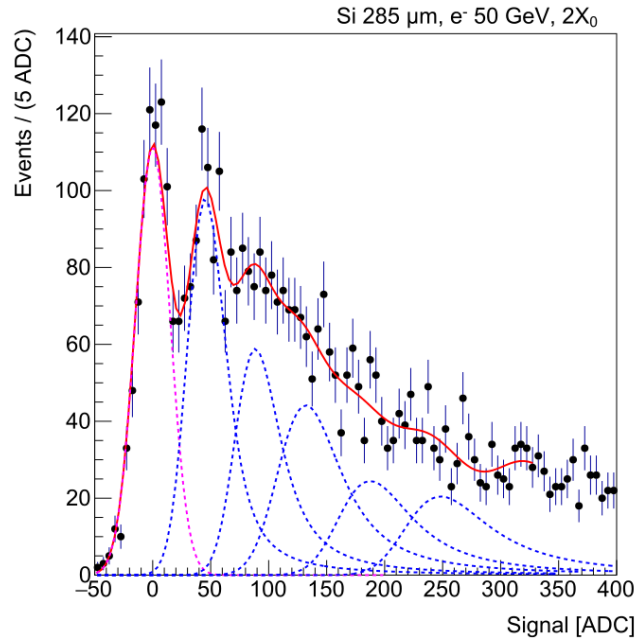


Figure 5.5: Reconstructed multi-MIP signal from the beam data [67]. The pedestal distributions are indicated by red dotted lines and centred at zero. The error bars are statistical only.

expected. The linearity of response to multiple charged tracks as a function of tracks multiplicities is within 3 % to 4 %.

### 5.3.3 Timing resolution

Timing resolution is defined as the Gaussian RMS width of the distribution of the time difference between the signals from the reference sensor and the diode under test. The pickoff time in the signals coming from the diodes was defined as the time when the pulse reaches its 50% of amplitude. This constant fraction discrimination method is one of the most efficient and versatile method available [69]. The pickoff time method is a constant fraction algorithm to suppress the time-walk related systematics, it assumes that the leading edge shape of the pulse waveforms is always the same. The algorithm looks for a pulse in the data stream and fits the pulse peak to a Gaussian function; pulse waveforms are required to have at least a duration of 100 ps. The pulse time is defined by the time at which the pulse waveform reaches half of its amplitude. All this process is done offline. An Example of single pulse shapes from two 200- $\mu\text{m}$  thick unirradiated diodes for the same event are shown in figure 5.6, where

the 50% of the peak value is indicated.

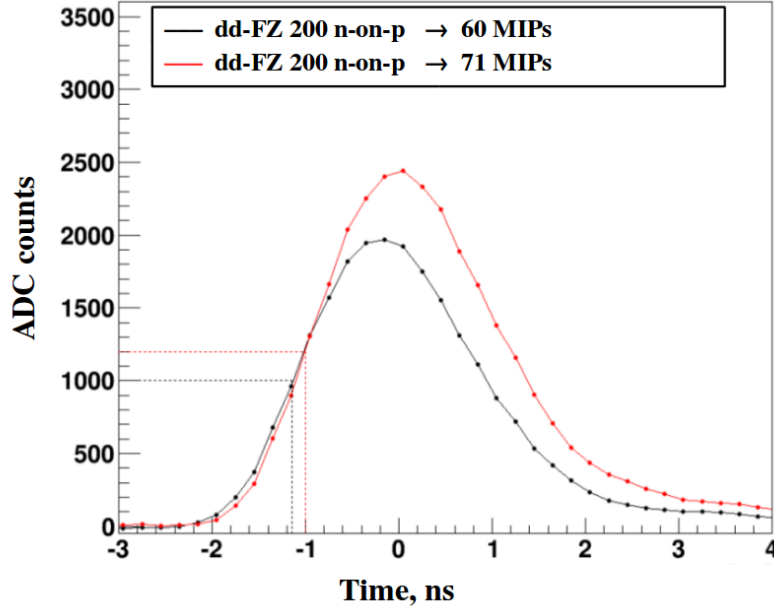


Figure 5.6: Examples of single pulse shapes from two diodes for the same event. 50% of the peak value is indicated by dotted lines and is used in all the timing measurements discussed in this chapter. The pick of the pulses is set at  $t = 0$  [67].

The time resolution is given by equation 5.1, where  $\sigma_{noise}$  is the noise and  $|\frac{dS}{dt}|$  is the slope of the leading edge of the signal. Assuming that the leading edge shape is constant, the slope should be proportional to the ratio of the pulse amplitude ( $S_{max}$ ) over the rise time (RT). Thus, the way of improving the time resolution is by having a higher signal-to-noise ratio (SNR) or a lower rise time in the signals.

$$\sigma_{time} \propto \frac{\sigma_{noise}}{|\frac{dS}{dt}|} \propto \frac{RT}{S_{max}} \sigma_{noise} \propto \frac{RT}{SNR} \quad (5.1)$$

The average pulse shapes from the three different thickness unirradiated diodes are shown in figure 5.7; the leading edge of the normalized pulsed is very similar for the three different thicknesses. Likewise, the duration of the three waveforms is similar, with a trailing edge possible determined by carrier diffusion. This similar pulse duration could be the result of a bandwidth-limited waveform shape.

The rise-time calculated from 10% to 90% of the pulse amplitude was measure to be 1.14 ns, 1.15 ns and 1.17 ns for the 120  $\mu\text{m}$ , 200  $\mu\text{m}$  and 320  $\mu\text{m}$  unirradiated diodes respectively.

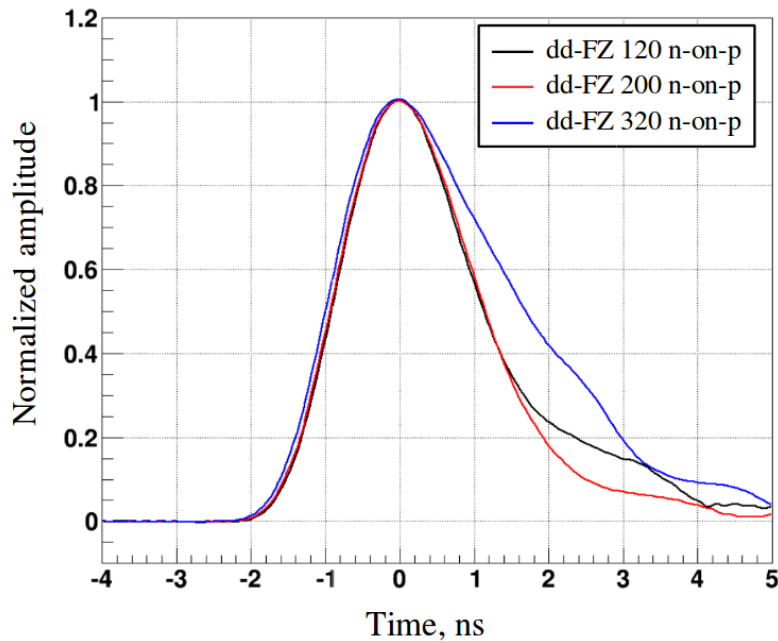


Figure 5.7: The average pulse-shapes from different thickness diodes. The amplitude is normalized to 1 for comparison and the pick of the pulses is set at  $t = 0$  [67].

In general was observed that pulse shapes are faster for lower thickness and at higher fluence. This result was confirm with the laser measurement in the TCT characterization, see figure 5.8. In figure 5.9 it is possible to observe that the pulse shape remain almost the same in the working range of temperatures. The measurements performed with IR laser using a  $300 \mu\text{m}$  unirradiated diode, show that at lower temperatures the pulses become narrower and faster (lower rise time). But the differences are almost negligible in terms of rise time.

The time performance was evaluated in three different configurations:

1. Using the two same thickness diodes without considering the MCP. This configuration was the only one used in the case of the irradiated diodes as the MCP were not included in the set-up. In this case the timing resolution is evaluated as a function of the effective signal strength, defined in equation 5.2. It can be seen, for the unirradiated and irradiated diodes, that the timing performance improves with increasing signal strength and that for equal S/N the timing performance of the three different thicknesses and irradiation fluences is similar.

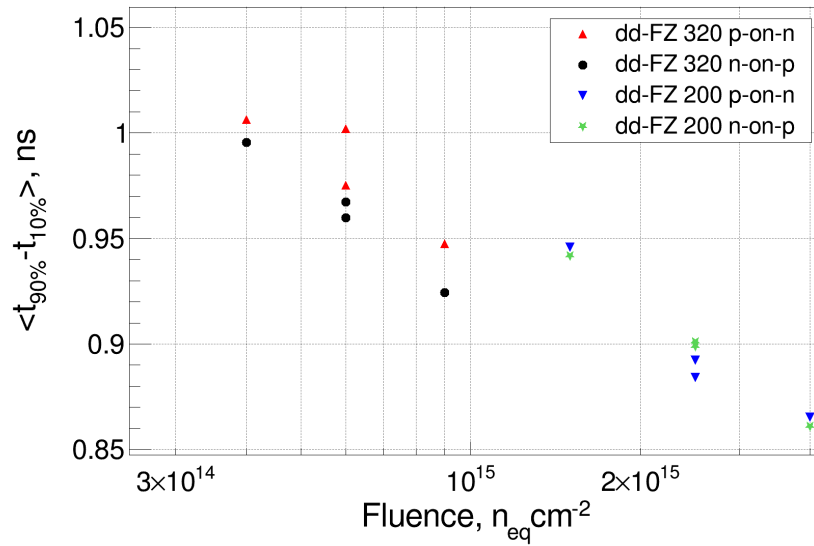


Figure 5.8: Rise time measured with IR laser for the irradiated diodes. It is observed that the higher the fluence the lower the rise time becomes.

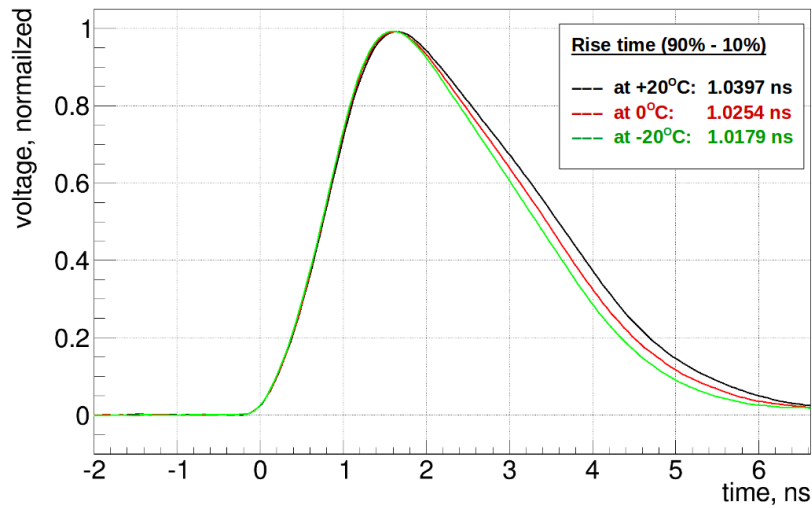


Figure 5.9: Rise time as a function of the temperature. Measurements done with IR laser with the unirradiated dd-FZ 320 p-on-n at 600 V. All pulses have been rescaled in order to compare them.

$$S_{eff} = \frac{S_1 S_2}{\sqrt{S_1^2 + S_2^2}} \quad (5.2)$$

In order to quantify the timing resolution of the two-diodes system a fit to a function form was used, see equation 5.3. In the equation  $A$  represents the noise and  $C$  represents the constant terms. The two terms on the right side of equation 5.3 are summed in quadrature as symbolized by  $\oplus$ , and the  $\frac{1}{\sqrt{2}}$  factor accounts for the two independent diodes as the time dispersion measured is the quadratic sum of two independent time dispersion.

$$\frac{\sigma(t_1 - t_2)}{\sqrt{2}} = \frac{A}{\sqrt{2}S_{eff}} \oplus C \quad (5.3)$$

In figure 5.10 the timing resolution is shown as a function of the effective signal strength in units of MIPs and the effective signal-to-noise ratio. As mention above the the timing performance improves with increasing signal strength and for equal SNR the timing performance of the three sensor types is similar. In this case, the time resolution reaches 10 ns.

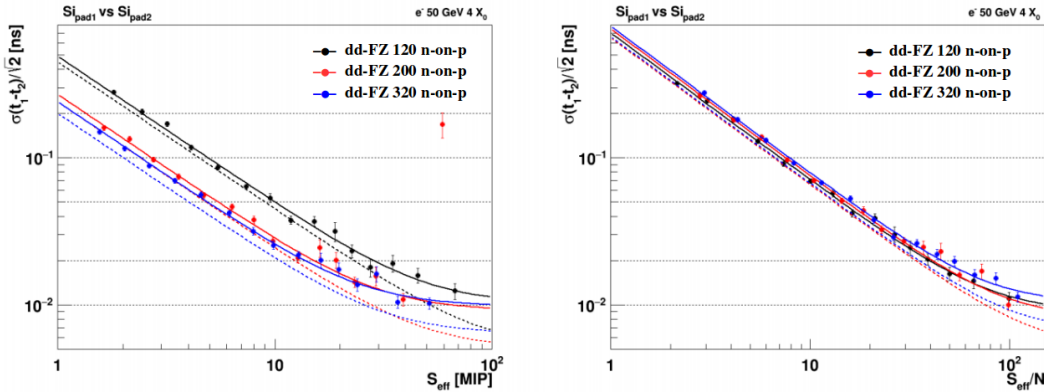


Figure 5.10: The timing resolution based on two diodes as a function of the effective signal (left) and as a function of the signal-to-noise ration (right). Toy simulation results are plotted in dotted lines [67].

Very similar timing resolution was observed measuring time difference between an unirradiated and irradiated diode of the same bulk type. Timing resolution as a function of the signal-to-noise ration does not depend on the fluence. The timing resolution of the unirradiated diodes at a given signal-to-noise can be obtained with the irradiated diodes when are operated in the same signal-to-noise point (large signals). There were no differences observe between the different thicknesses and the bulk types neither. In figure 5.11 is shown the timing resolution as a function of the signal-to-noise ratio of the dd-FZ 320  $\mu\text{m}$  irradiated diodes, the ones with more statistics. Very similar timing resolution (about 15 ps ) was measured for large signals.

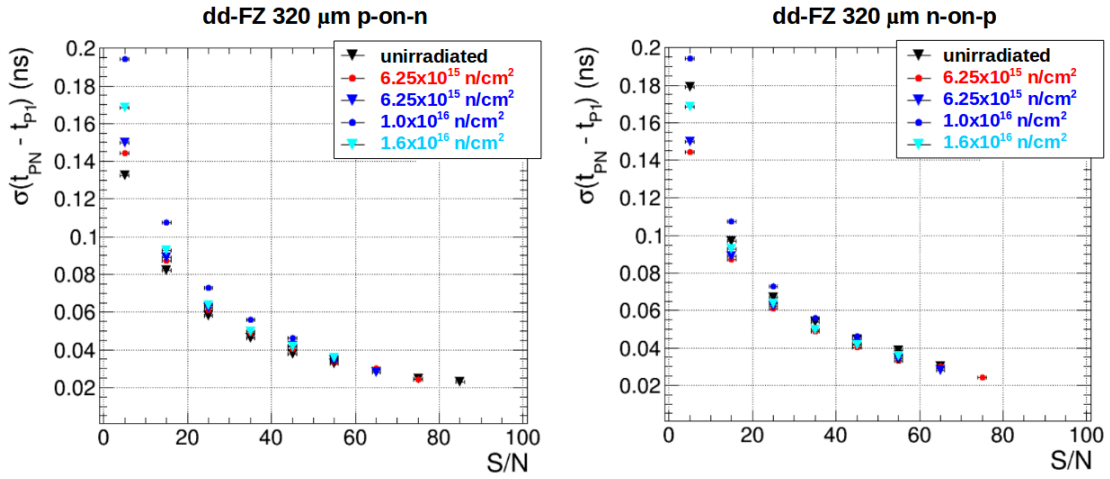


Figure 5.11: Time resolution as a function of the S/N for the irradiated dd-FZ 320  $\mu\text{m}$ . The p-on-n diodes were measured in April (left) and the n-on-p in June. In both cases  $V_{\text{bias}}$  was 600 V, and the timing resolution large signals is about 20 ps (15 ps for one single diode).  $\sigma(t_{pN} - t_{p1})$  is the time resolution between the first unirradiated diode uses as a time reference and the remaining five diodes of the set (N from 2,...,6) [70].

2. In the second configuration one of the two diodes was used together with the MCP. By replacing one of the diodes with a MCP, the timing resolution varied from 18 to 24 ps reflecting the limiting performance of the MCP as shown in figure 5.12. The timing resolution of the MCP was estimated to be 21 ps. This was done only in the first test beam with the unirradiated diodes. In equation 5.4 shows the fit function used in this test.

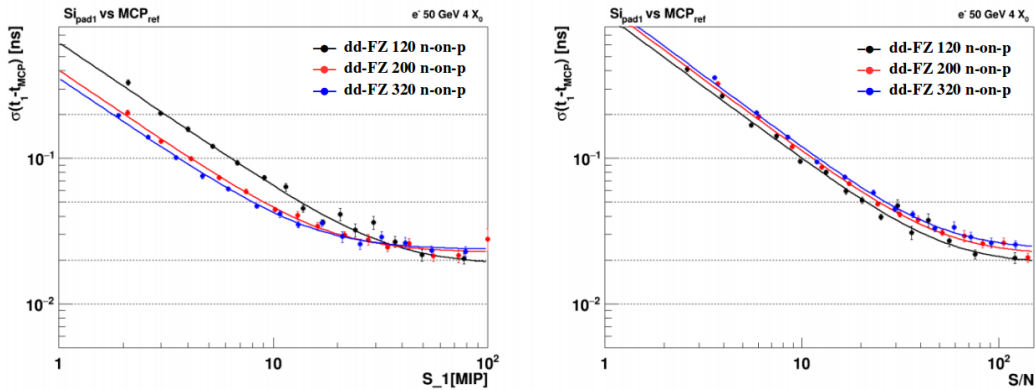


Figure 5.12: The timing resolution between the signal of the first diode and the MCP as a function of the effective signal (left) and as a function of the signal-to-noise ratio (right) [67].

$$\sigma(t_1 - t_{MCP}) = \frac{A}{S_1} \oplus C \quad (5.4)$$

3. In the third configuration the average signal ( $S_{mean} = \frac{1}{2}(S_1 + S_2)$ ) of the two diodes was used together with the signal from the MCP as in the previous one. In this case the timing resolution of the system was dominated by the MCP as in the previous test obtaining very similar results, see figure 5.13. However, the comparison of the noise terms reveal the potential power and the higher level of performance of the independent timing measurements from the silicon sensors. In equation 5.5 shows the fit function used in this test. This test was done only in the first test beam with the unirradiated diodes.

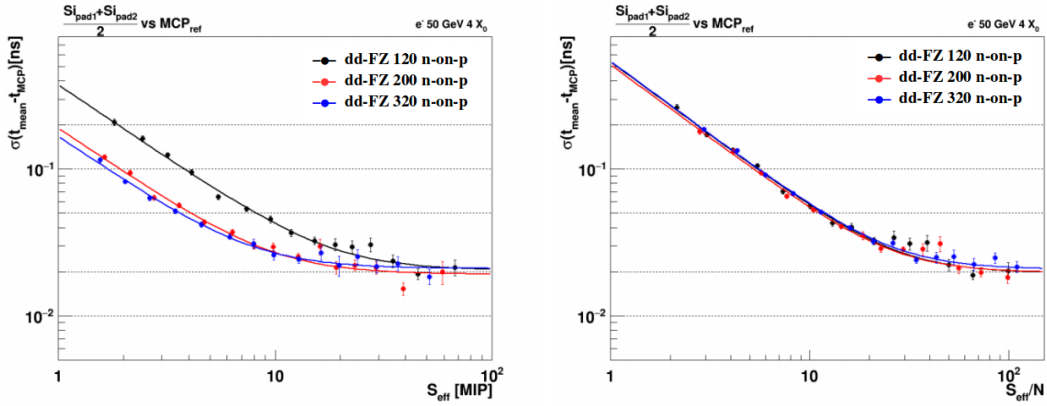


Figure 5.13: The timing resolution between the mean signal of the two diodes and the MCP as a function of the effective signal (left) and as a function of the signal-to-noise ratio (right) [67].

$$\sigma(t_{mean} - t_{MCP}) = \frac{A}{2S_{eff}} \oplus C \quad (5.5)$$



## Chapter 6

# Two-dimensional position-sensitive microstrip sensor with resistive electrodes

Many devices have been developed during the last decades in order to measure two coordinates of an ionizing event. Some examples are the double-sided microstrip detectors and the drift detectors, that used the double-sided processing resulting in different pulse shapes that complicate the signal readouts [20], or the pixel detectors that implement a complex read-out system with a large number of electronic channels to have both coordinates with enough spatial resolution. In this chapter a different approach is studied to provide a single-sided detector 2D position sensitive and with a limited number of readout channel [17]. This technology integrates in a common microstrip single-sided detector resistive coupling electrodes and a double read out system for each strip, which allows to obtain two coordinates of an ionizing even, making use of the resistive charge division method and just doubling the number of channels.

These novel 2D position-sensitive microstrip sensors were already studied and characterized in previous works [18, 71] but their tracking performance has never been assessed so far. For this thesis, the sensors were characterized with a  $^{90}\text{Sr}$  radioactive source to measure their signal-to-noise ratio and they were tested in a test-beam at the SPS North Area facility at CERN in order to measure their spacial resolution. The results are presented in this chapter.

---

## 6.1 Concept: Resistive charge division in microstrips sensors

The resistive charge division method has been frequently used in gaseous detectors with resistive anodes [72, 73] and studied for silicon pad detectors [74], but it has never been implemented in actual semiconductor microstrip detectors. The basic characteristics of the charge-division concept for resistive electrodes was formulated for the first time by Radeka in 1974 [75]. One of the main conclusions of this study was the fact that the position resolution (assuming a readout electronics with optimal shaping time) is determined only by the electrode capacitance and not by the electrode resistance.

A standard microstrip sensor is only sensitive to one coordinate, which is given by the position of the impact in the direction perpendicular to the strips. A hit can induce signal in different strips due to capacitive charge sharing [76]. The position of the hit is determined by the charge weighted center of gravity of these strips. The digital resolution in the position measurement ( $\sigma$ ) is given in terms of the pitch ( $p$ ) or distance between strips in equation 6.1.

$$\sigma = \frac{p}{\sqrt{12}} \quad (6.1)$$

The prototypes have resistive electrodes instead of metallic electrodes. Polycrystalline silicon is used as resistive material, and the hit position along the strip length is determined from the signal attenuation along the resistive electrode strip, see figure 6.1. The aluminium pads are connected each one to a channel of the read-out electronics (two for each strip). When an ionizing particle crosses the detector, different signals ( $S_1$  and  $S_2$ ) are read by the opposite electronic channels. The X coordinate of the event can be reconstructed using the center of gravity method, whereas the Y coordinate is reconstructed comparing the signal amplitudes at the ends of strips. This original approach decouples the resistive electrodes from the detector diode structure (determining the charge collection) through a coupling capacitance (gray layer in figure 6.1). Like this, it is easy to manufacture AC coupled  $p^+$ -on-n or  $n^+$ -on-p detectors, more convenient for the case of high radiation environments.

In a conventional microstrip detector the metal contacts of the strips extend over almost all the length of the implants and are connected each one to a read-out channel. When an ionizing particle crosses the detector, the propagation of the induced signal along the coupling electrode does not suffer significant attenuation, i.e., the signal amplitude does not depend on the particle impinging point along the electrode direction. When using, instead

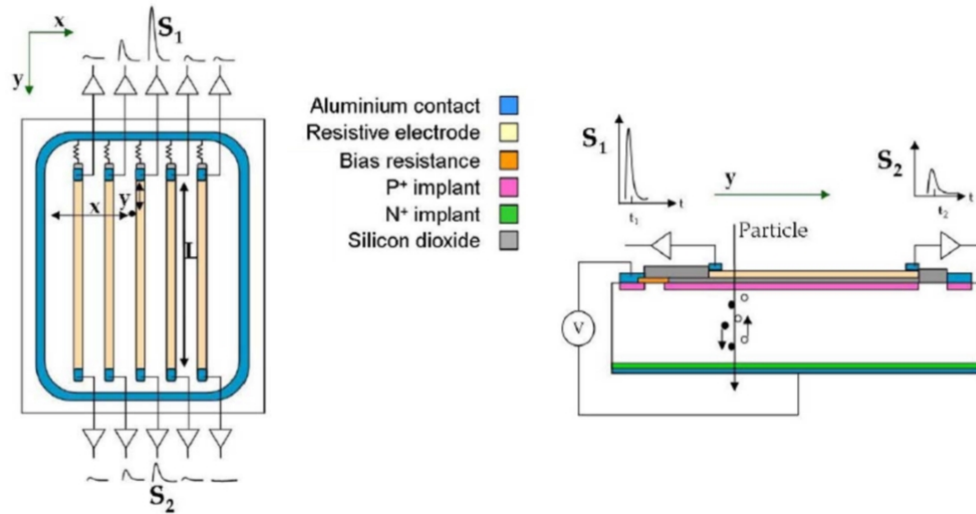


Figure 6.1: Schematic top view of the novel detector (left). Lateral cross-section of the central strip, not to scale (right). In blue are represented metallic contacts and in yellow are the resistive electrodes visible in both pictures [19].

of a metal alloy, a resistive electrode equipped with metal contacts at its ends, the signal undergoes significant attenuation during its propagation towards the electronics contacts. The longer the propagation length, the larger the signal attenuation. In this way, a conventionally manufactured single-sided microstrip sensor can provide the two-dimensional coordinates of the particle impinging point; the transverse coordinate derived from the usual electrode segmentation [76] and the longitudinal coordinate determined by relating signals amplitude at both ends of the electrode.

The resistive electrode represents a diffusive RC line, in which a current pulse undergoes not only an amplitude attenuation but also an increase of the rise time the further it travels. Using readout electronics characterized by a short shaping time compared to the RC constant of the line, which translates into a non-constant signal ballistic deficit [18]. The ballistic deficit can be reduced increasing the shaper peaking time; however, a longer peaking time increases the parallel readout noise contribution. In reference [75], Radeka derived the optimal peaking time for a resistive charge division configuration, under the assumption of high

electrode resistance compared to the amplifier impedance and long amplifier peaking time compared to input signal rise times. Under these assumptions, dependence between the longitudinal coordinate of the particle position and the fractional signal amplitude read from one side of the strip is expected to be linear. The actual functional form is given by equation 6.2 (with  $A_1$  and  $A_2$  the amplitudes of  $S_1$  and  $S_2$  respectively):

$$y = L \frac{A_2}{A_1 + A_2} \quad (6.2)$$

## 6.2 Proof of concept prototypes

Several wafers were processed at IMB-CNM. Two different 2D position-sensitive sensor prototypes were produced with different electrode resistivity in order to study their possible influence in the sensor performance. Each sensor has 384  $p^+$  strips (  $20 \mu\text{m}$  wide and 2 cm long) with a pitch of  $80 \mu\text{m}$  on a  $285 \mu\text{m}$  thick p-on-n substrate.

The two 2D microstrip sensor have the same structure of a standard sensor with the same geometry but with resistive instead of metallic (Aluminum) electrodes which are readout from the two electrode ends (instead of just one end as in the case of standard microstrip sensors). In table 6.1 are shown the main parameters of these two prototypes. And the results from the electrical characterization are shown in figure 6.2.

$R_{electrode}$	Full Depletion (V)	Breakdown (V)	$C_{int}$ (pF/cm)	$C_{AC}$ (pF/cm)
$2.8 \Omega/\mu\text{m}$	20	300	0.46	189
$12.2 \Omega/\mu\text{m}$	20	400	0.46	189

Table 6.1: Main parameters of the two sensor prototypes.

For this study, no dedicated analog signal processing electronics was built and therefore the front-end filtering of the signal was non-optimal; no effort was made to optimize the shaper peaking time accordingly with the detector time characteristic, i.e., the time characteristic of the RC propagation line equivalent to the detector strip. An Alibava DAQ system developed within the framework of the CERN RD50 collaboration was used [77]. The analog front-end of the ALIBAVA system is based on the Beetle readout chip used for the microstrip sensor readout of the silicon tracking subsystem of the LHCb experiment at LHC [78]; consequently, the analog front-end shaper peaking time of the Alivaba system is set around 25 ns. Figure 6.3 shows a photo of one of the detectors mounted on the Alibava daughter board.

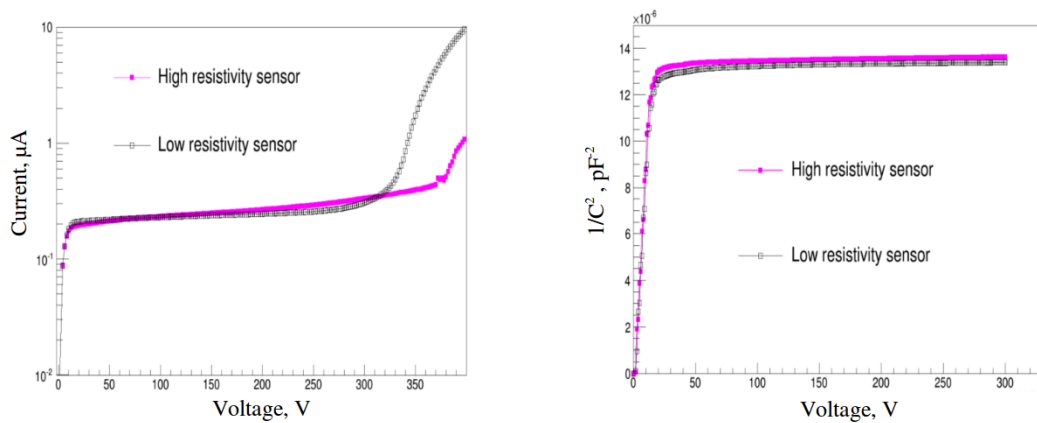


Figure 6.2: IV-curves (left) and CV-curves (right) from the two 2D-position sensitive prototypes [71].

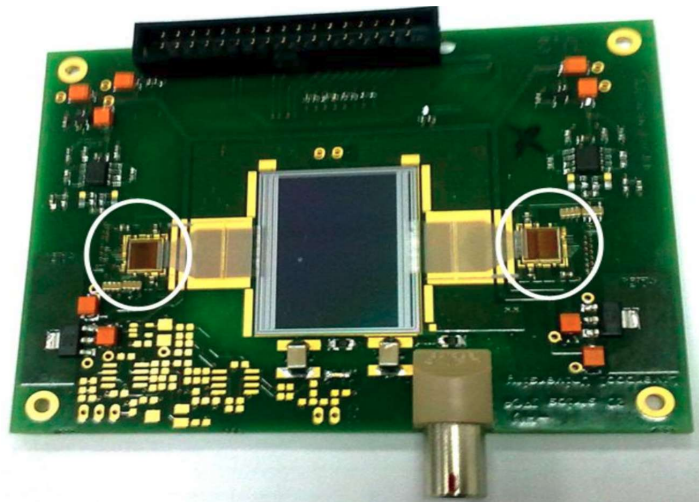


Figure 6.3: Photo of one of the detectors mounted on the Alibava daughter board, the two Beetle chips are indicated with white circles. Each one reads out the same 128 consecutive strips providing double-sided readout [71].

### 6.3 Electrical simulation vs laser characterization

A SPICE-like model of the detectors was developed with Virtuoso Spectre by Cadence [79] which was used for studying the signal propagation along the resistive strips: attenuation and delay. The simulation was experimentally validated against a laser (1060 nm) longitudinal scan moving the focused beam spot ( $5 \mu\text{m}$ ) along the poly-silicon electrode.

In the SPICE model a simulated current pulse was injected at different points along the

strip length and its response was studied. The model was built starting from reference [80] using standard components from the AnalogLib library of Virtuoso Spectre by Cadence. Five consecutive strips have been modeled composed from 80 different unit cells, each one corresponds to a section of  $250 \mu\text{m}$  of the strip length. The unit cell is formed by different capacitances and resistors that represent the main electrical characteristics of the device.  $R_{sub}$  and  $C_{sub}$  describe the substrate,  $R_{int}$  and  $C_{int}$  the interstrip parameters,  $C_{AC}$  the coupling capacitance and finally, the implant and electrode resistances are represented by  $R_{imp}$  and  $R_{el}$ , respectively. Figure 6.4 shows the schematic of a unit cell. Five different strips can be distinguished. The model of the readout electronics connected to the ends of each strip emulates a generic charge sensitive preamplifier followed by a CR-RC filter whose peaking time matches the Beetle chip peaking time (about 25 ns). The shape of the simulated input signal along the strip length is shown. It has a rise time of 2 ns (similar to the laser pulse rise time) and a total integrated charge of 4 fC. In the simulation, the signal was injected in different nodes along the implant line on the central strip in 2 mm steps.

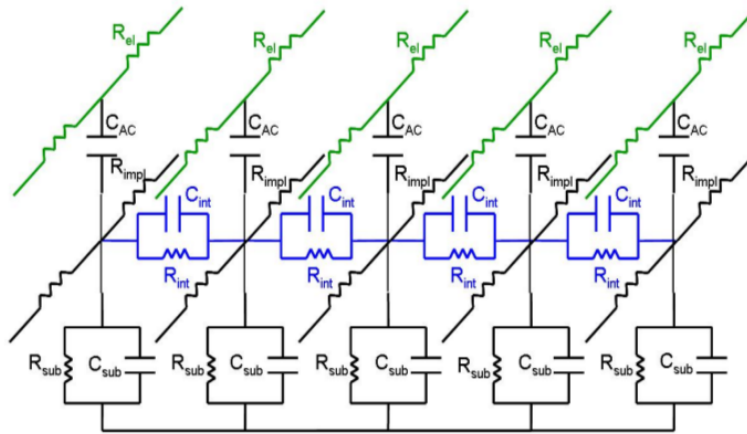


Figure 6.4: Schematic of one of the 80 cells used to model the detector. One cell represents  $250 \mu\text{m}$  of all the five strips together [71].

The linear dependence of the position along the strip on the fractional signal amplitude is clearly seen in figure 6.5. According to equation 6.2, with  $A_1$  and  $A_2$  the amplitudes read at the first and the last cells of the strip respectively, the derived fractional position versus the injection fractional position ( $L$ ) is shown in figure 6.5 (left). The data related to the more resistive prototype reveals a clear separation (larger residuals spread in figure 6.5) from the ideal values due to the ballistic deficit which increases with the distance covered by the signal from the point of generation.

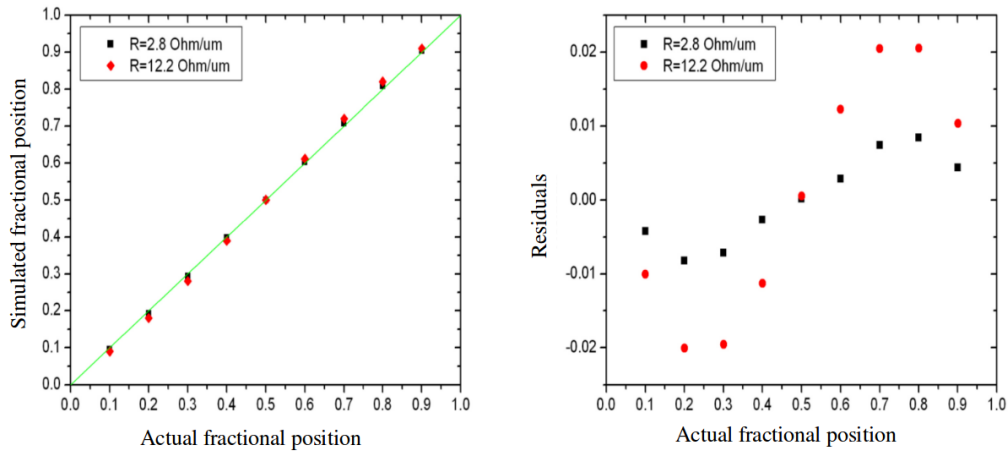


Figure 6.5: Simulated fractional position as a function of the actual fractional position (left) and residuals (right) obtained from simulated prototypes [71].

It is worth to note also that in the case of the low resistivity prototype, even for the more attenuated pulse, the rise time is around 10 ns, nearly 40% of the beetle peaking time, and therefore the effect of the ballistic deficit in this sensor is highly suppressed.

The laser measurements consisted of a longitudinal scan along a polysilicon electrode for each sensor. The polycrystalline silicon that forms the electrodes is transparent to the infrared light, so that allows to test the signal division in the strip. The measurements were done using the Alibava DAQ system and the analysis of the recorded data was done by modifications of the source code supplied by the Alibava system based in ROOT [44]. The reconstruction of the pulse shape for every scan position was obtained and in order to reproduce the results obtained from the simulation, the amplitude from the reconstructed pulses were accurately extrapolated by fitting a Gaussian function to the peak region. Then, the mean and the sigma values were used for the calculation of the fractional position defined by equation 6.2.

An excellent agreement between the experimental data (fractional position  $y$ ) and the sensor electrical emulation was found, as can be seen in figure 6.6. Simulation and experimental results are in very good agreement showing a similar systematic behavior, confirming that the electrical simulation of the devices is able to reproduce properly the systematic errors due to a non-optimal shaping time.

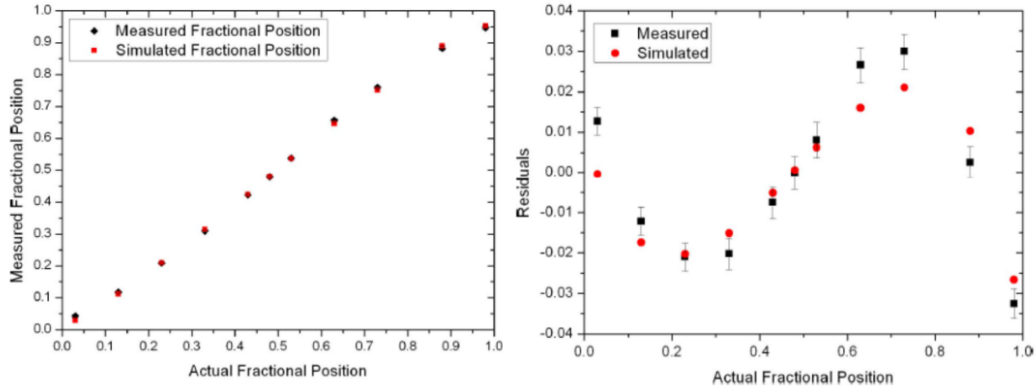


Figure 6.6: Experimental results compared with the simulation for the high resistivity prototype [19].

## 6.4 Studies on the position measurement error

A very detailed study on the position measurement error using the laser characterization of these first proof-of-concept demonstrators can be found in these two reference [81, 71]. In this study, special emphasis on how the different noise sources are affecting the device position error along the strip was done.

As in a standard silicon sensor, the noise of these prototypes (read out by an analog front-end consisting in a charge sensitive amplifier followed by a shaping stage) depends both on the sensor itself and on the signal processing electronics. The most important noise sources are:

1. Noise from the input transistor of the amplifier  $\sigma_a$ . This noise varies with the kind of amplifier input transistor. The most relevant point for this discussion is the fact that this error is uncorrelated between the two ends of the sensor.
2. Thermal noise  $\sigma_R$  from the resistive electrode, this noise, being originated by thermal fluctuations of the current in the electrode, is expected to be anti-correlated between the two ends of the sensor.
3. Shot noise produced by the statistical fluctuation of the sensor's leakage current. Due to the external origin of this noise contribution generated in the silicon bulk, the noise must be fully correlated between the two ends of the sensor.

In order to evaluate the noise in the prototypes, a longitudinal scan moving the focused laser beam spot along the midline of a polysilicon electrode was performed. The whole electrode length (20 mm) was scanned. For each scanning point, 20,000 laser pulses were recorded.

The noise in absence of laser source or other signal was measured. It was defined as the width of the pedestal obtaining a Gaussian distribution with a sigma of 1.83 ADU and 1.8 ADU respectively for the noise of  $A_1$  and  $A_2$  amplitudes. The lack of correlation ( $\rho \simeq 0.03$ ) implies that the uncorrelated noise component (amplifier noise) dominates.

In figure 6.7 the noise value for channel  $A_1$  when doing the laser scan along the strip length is shown. This noise is computed as the width of the amplitude distribution at each scanning point. As expected, the further we move the laser spot away from the  $A_1$  end, the further the noise is reduced, that is, the laser contribution to the noise is reduced linearly as  $y/L$  increases until the other noise components (amplifier, leakage and thermal) start to be dominant, reaching a final noise figure at the far end of the electrode very similar to the previously quoted pedestal width.

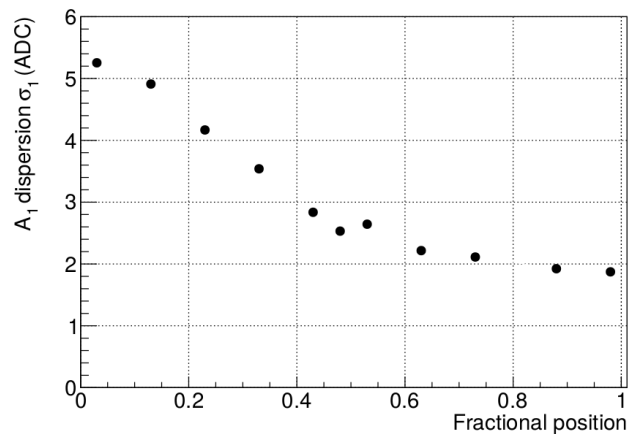


Figure 6.7: Noise values for the  $A_1$  signal along the strip scanning points [81].

The change in the relative contribution of each of the noise components is also shown in the dependence of the lineal correlation coefficient from the variables  $A_1$  and  $A_2$  with the laser scan position, as it is shown in figure 6.8.

The position measurement error was estimated in two different ways:

1. In a direct way, taking as error the width of the distribution of variable  $y/L$  (defined in

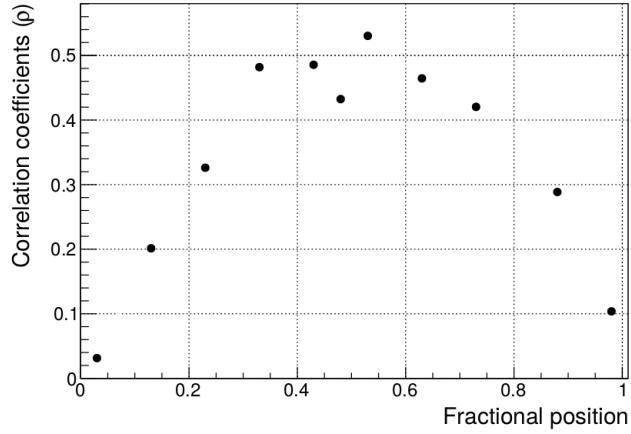


Figure 6.8: Correlation coefficients  $\rho$  at the different laser scan points. The change in  $\rho$  for each point is due to the change in the relative contribution of the different noise sources [81].

equation 6.2) obtained at each scanning point from the 20.000 laser pulses.

2. In an indirect way, using equation 6.3 and propagating the uncertainty on the measurement of the signal amplitudes and taking into account the measured correlation at each scanning point.

$$\sigma_y^2 = \frac{1}{(A_1 + A_2)^2} [(L - y)^2 \sigma_2^2 - 2y(L - y)\rho\sigma_1\sigma_2 + y^2 \sigma_1^2] \quad (6.3)$$

From equation 6.3, assuming  $\rho \approx 0$  and  $\sigma_1 \approx \sigma_2 = \sigma_A$  it is obtained equation 6.4. Thus, the resolution is proportional to the inverse of the signal-to-noise ratio.

$$\sigma_y^2 = \frac{(L - y)^2 + y^2}{(A_1 + A_2)^2} \sigma_A^2 \quad (6.4)$$

The resulting position errors are given in figure 6.9. As expected, a minimum of the error around the center of the electrode with maxima near the ends is observed. As a consistency test and a proof of the gaussianity of the uncertainty distributions it can be seen that the two ways of estimating the error yield almost identical values.

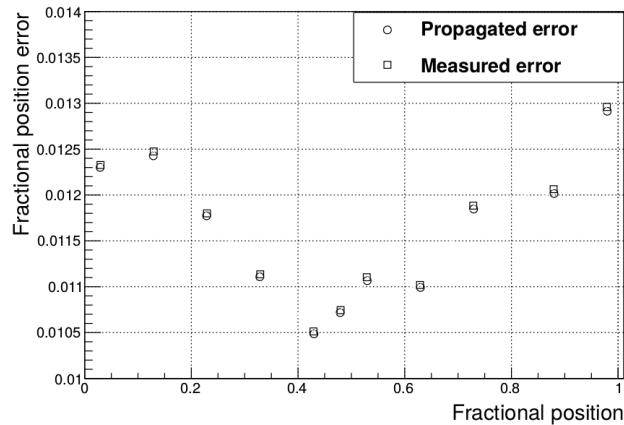


Figure 6.9: Fractional position measurement error at each scanning point [81].

## 6.5 Signal-to-noise studies with radioactive source

To evaluate the signal-to-noise ratio in these 2D position-sensitive sensors and the its dependence with the position along the strip a  $^{90}\text{Sr}$  radioactive source was used. In figure 6.10, it is shown the set-up used for this propose. The  $^{90}\text{Sr}$  radioactive source, the sensor and the photomultiplier were well aligned using a mechanical support and two positioning stages allowed precise movements of the sensor along the beam spot. A beam collimator was used to focalize the impact of the electrons coming from the  $^{90}\text{Sr}$  radioactive source on the surface of the sensor. The diameter of the spot was about 1.5 mm. A scan over the Y-coordinate (the resistive one) was done in steps of 1 mm (18 in total) in order to measure the S/N along the strip and to reconstruct the longitudinal position over the y-coordinate as a function of the real position given by the stages. The measurements were done using the Alibava DAQ system and the analysis of the recorded data was done in ROOT. It was only measured the low resistivity sensor as the high resistivity one was not available when this test was carried out. The bias voltages applied was 100 V to guarantee the full depletion and the measurements were performed in a dry atmosphere at room temperature.

In each step 20.000 events were collected to have enough statistic to do the analysis. For each step was measured the noise (fitted with a Gaussian function) and the charge distribution was extracted and fitted with a convoluted Landau and Gaussian function [64]. In order to get the S/N the most provable value of the Landau fitting function was divided by the noise measured. This was done for all the 18 steps. Figure 6.11 shows the charge distribution fitted with the convoluted function, in S/N units, for one spot close to the center of the strip. The

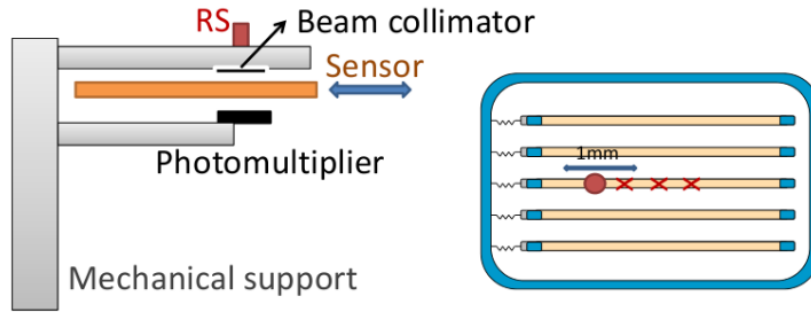


Figure 6.10: Schematic of the set-up used for the S/N studies.

longitudinal position was extracted using equation 6.2 for each hit of every step in the strip. The distribution of all the positions extracted for the 20.000 hits of every single step was fitted with a Gaussian function and the mean value of the distribution was giving the position of the spot over the strip. Figure 6.11 shows the hit distribution along the strip for the same step already mentioned above.

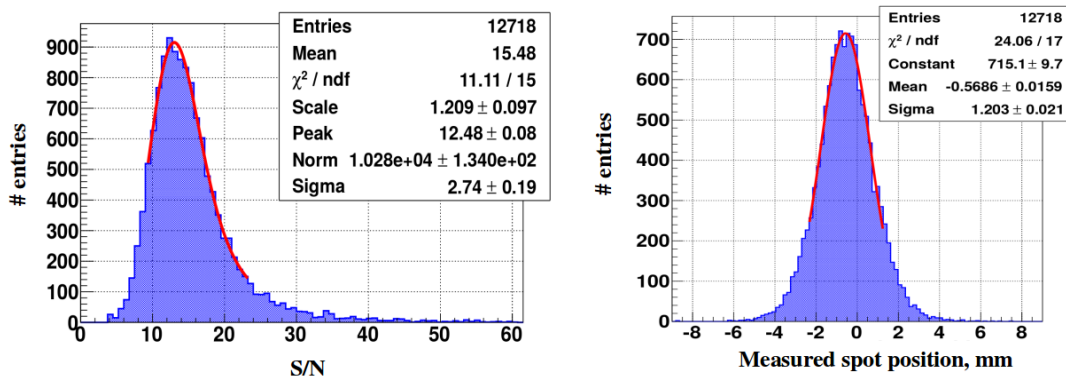


Figure 6.11: Charge distribution (left) for one position close to the centre of the strip done with the  $^{90}\text{Sr}$  radioactive source, the S/N measured was 12.48. The corresponding distribution of the reconstructed position (right).

The resulting signal-to-noise ratio, defined by equation 6.5, measured along the y-coordinate for all the 18 steps is shown in figure 6.12. It can be observed that the signal-to-noise in the case of the low resistivity 2D position-sensitive sensor is around 12.5 and quite constant along

the y-coordinate. It is significantly smaller than the value obtained in a standard sensors with the same thickness (around 20). This difference is due to the fact that the channel noise of a resistive strip increases from 1100 electrons to 1500 electrons; moreover, the signal is divided among the two opposite channels. In consequence, the signal-to-noise ratio is expected to be reduced approximately by a factor of  $1.35 \times \sqrt{2}$ ; the factor 1.35 comes from the ratio of the channel's noise and the factor  $\sqrt{2}$  is due to the charge division.

$$S/N = \frac{A_1 + A_2}{\sigma_{(A_1+A_2)}}; \quad \sigma_{(A_1+A_2)} = \sqrt{2} \sigma_{A_1} \quad (6.5)$$

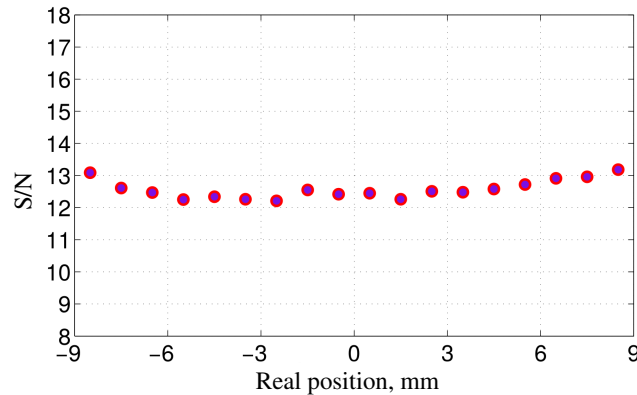


Figure 6.12: Signal-no-noise measured along the strips. The value obtained is about 12.5 and it is quite constant along the y-coordinate.

The extracted spot position as a function of the real position is shown in figure 6.13 (left). The fit between real position and reconstructed position is almost lineal. The fitted slope differs from one due to the misalignment between the axes of movement and the strip direction. The residual from the fit are plotted in figure 6.13 (right), where we can see that the linearity is degraded at the end of the strips, mostly due to fact that the radioactive source illumination area is outside the sensor's fiducial region.

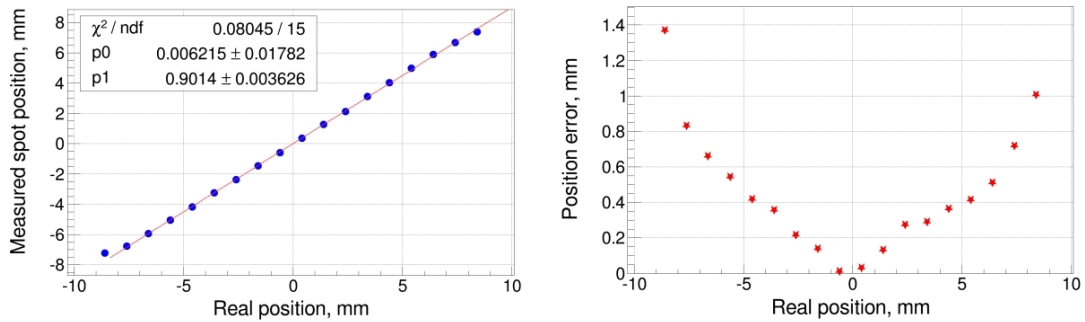


Figure 6.13: Reconstructed spots positions along the strip as a function of the real position given by the stages (left). Residuals (right).

## 6.6 Test-beam studies: beam monitoring and spacial resolution

In order to evaluate the performance of these sensors in a more realistic conditions a test-beam was carried out in November 2012 at the SPS H6 line at CERN [46]. The initial idea was to test at the same time both prototypes, but the high resistivity one was not working and it was replaced for a standard strip detector of  $300 \mu\text{m}$  thick. The goal of the test-beam was to measure the tracking performance of the prototypes; mainly, their spacial resolution over both coordinates (longitudinal and transversal). For measuring the spacial resolution in these sensors it was required to have tracking information during the test-beam and this was accomplished by using the EUDET telescope previously introduced in section 3.4. The full system integration and synchronization between them (telescope, trigger, sensors) was successfully achieved.

### 6.6.1 Experimental set-up

The set-up used during the test-beam is shown in figure 6.14 where the different elements of the set-up, listed, can be observed. The main elements are: devices under test (DUTs) (7 and 8), telescope planes with the Mimosas26 sensors on them (from 1 to 6), movable support with the DUTs (9) and photomultiplier for the triggering (0). The alignment between the DUTs and the telescope planes is shown at the bottom right. For limitations of the mechanical support it was not possible to center the standard strip sensor but it was useful anyway during

the test-beam for the S/N measurements. The measurements were done using the Alibava DAQ system which was fully integrated into the DAQ system of the EUDET telescope to allow the event synchronization and the subsequent tracking reconstruction of the full system.

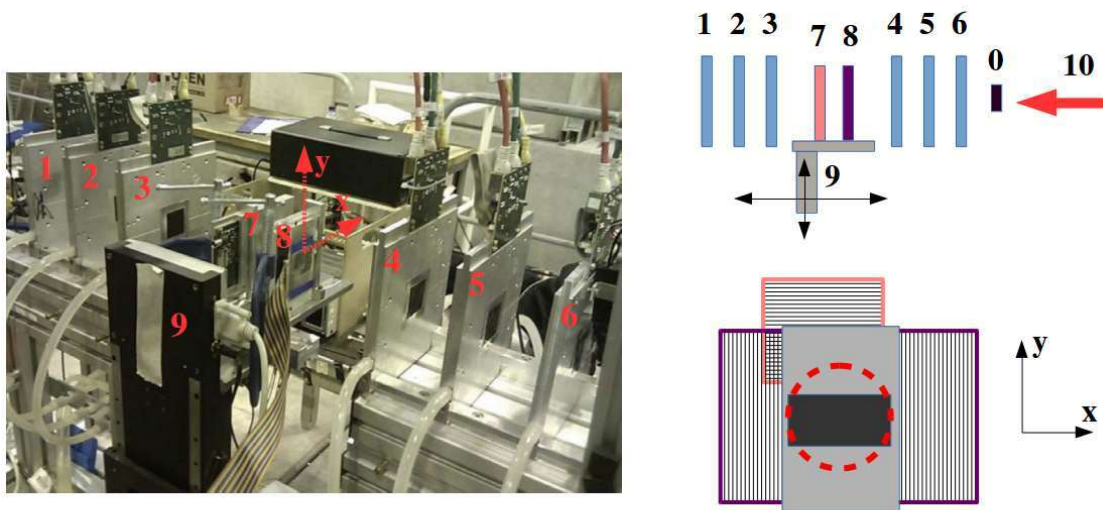


Figure 6.14: Picture of the set-up with the main elements listed (left). 0 photomultiplier, from 1 to 6 telescope planes, 7 standard strip sensor, 8 proof-of-concept sensor, 9 movable support, 10 pion beam direction. Schematic right-side view of the set-up (top right) and schematic front view of the set-up (bottom right). The size of the pion beam is represented in a dotted red line (12 mm of rms).

The test-beam was performed at room temperature and both sensors were biased at 80 V. At this voltage the 2D position-sensitive sensor was fully depleted but the standard strip sensor was not, and due to time constraints during the test-beam it was not possible to measure it fully depleted. The beam particles were pions of 150 GeV with a spot beam of 12 mm. During the test-beam different runs were taken depending on the propose of the test, and the DUTs were moved around de vertical axis (y) up and down for testing the monitoring performance of the sensors and to see possible influences in the S/N or in the position resolution at different position of the strip.

## 6.6.2 Analysis and results

The signal-to-noise measured during the test-beam was found to be in agreement with the one measured with the  $^{90}\text{Sr}$  source in the lab and presented in the previous section. There was no variation during the different runs taken as it was expected. Figure 6.15 shows the signal-to-noise ratio measured during one of the test-beam runs for both sensors. The value was found to be about 11.5 for the 2D position-sensitive sensor and about 14.5 for the standard strip one (that it was not fully depleted). Notice that the signal measured with the  $^{90}\text{Sr}$  radioactive source is in general higher than the one measured in the test-beam with MIPs. This is mainly for two reasons: the first one is due to the energy spectrum of the electrons emitted from the  $^{90}\text{Sr}$  source is wider than the range where the energy absorption in silicon is minimum, see figure 3.16; and the second reason is due to the percentage of the electrons whose incident is not perpendicular to the sensor while measuring with the  $^{90}\text{Sr}$  source, and they generate more signal as the ionizing path inside the sensor is larger.

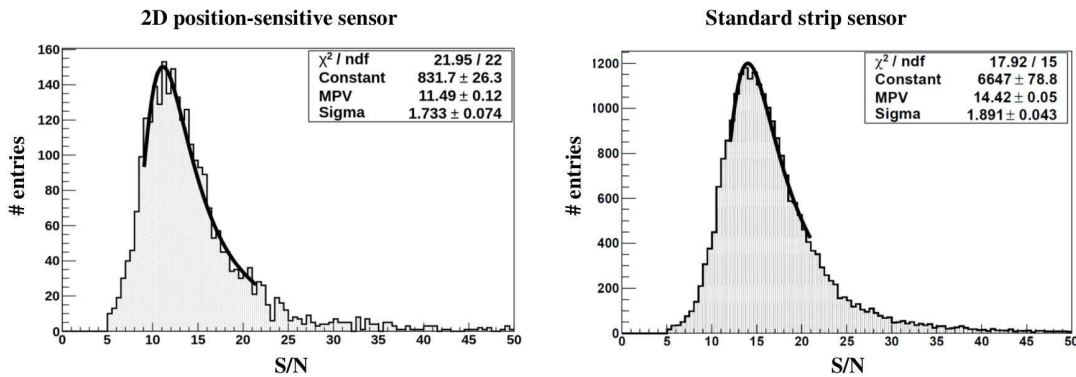


Figure 6.15: Signal-to-noise ratio measured during the test-beam for the 2D position-sensitive sensor and the standard strip sensor.

The beam profile of the beam was measured during the test-beam, but the shape of the beam spot over the 2D position-sensitive sensor was biased by the area of the two coincident photomultiplier. The resulting spot measured on the sensor was a convolution of the beam spot (12 mm in rms) with the square area of the coincidence photomultipliers ( $5 \times 10 \text{ mm}^2$ ). The beam profile for the first run centred in the sensors can be observed in figure 6.16.

In order to have enough statistics for the spacial resolution studies all runs were analyzed together and the spatial resolution as a function of the resistive coordinate was not studied.

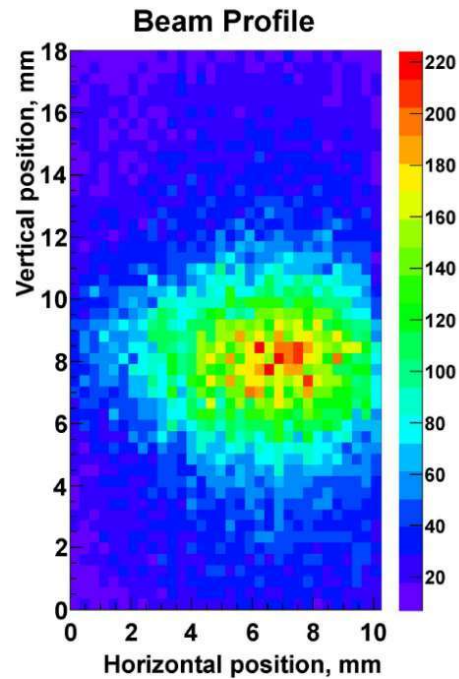


Figure 6.16: Pion beam profile measured on the sensor during one run in the test-beam.

The reconstruction of the particle tracks was done using the standard software framework for EUDET pixel beam telescope [82] with the particular geometry of this test-beam (distance between telescope planes and position of the DUT). All the tracks were projected on the DUT plane in order to have the x-coordinate and y-coordinates on the detector that were used as a reference. In figure 6.17 the residuals of the particle tracks extracted in the offline analysis in one of the planes of the telescope are shown for both coordinates. The projection of the particle tracks in the DUT plane was done with a precision of around  $6 \mu\text{m}$ .

The hits in the 2D position-sensitive sensor were extracted using the original Alibava software previously mentioned with some modifications included for the proper analysis of these type of sensors. The fractional position over the y-coordinate (resistive one) was calculated in the same ways as in the previous section, using equation 6.2. But in the case of the x-coordinate the position was not determined by the charge weighted centre of gravity between strips, instead a  $\eta$  distribution was considered [83, 76]. The charge division between strips is far from been linear, in that case the  $\eta$  distribution should be flat and the charge weighted centre of gravity could be applied. This observed non-linearity can be fully explained by the

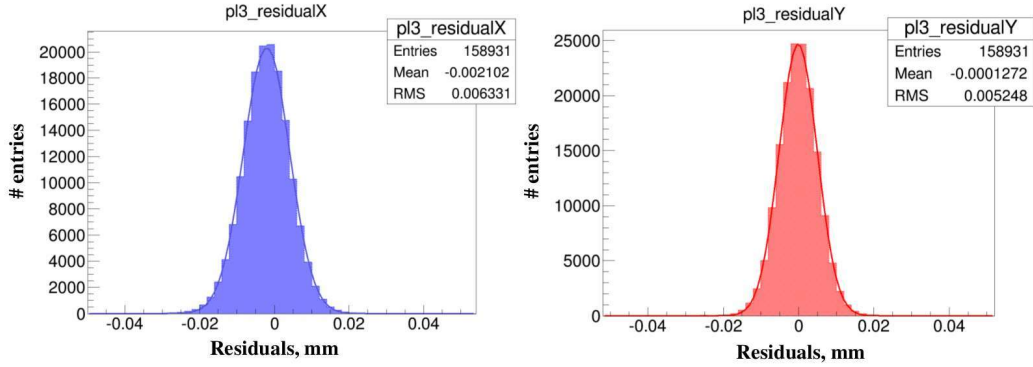


Figure 6.17: Residuals of the particle tracks in one plane of the telescope.

width of the diffusion cloud. For perpendicular tracks, which is the case, charge spread is dominated by diffusion. The width of the charge cloud depends on detector parameters as the thickness, the resistivity and the applied voltage. For most of the detectors used in high-energy physics, the thickness is around  $300 \mu\text{m}$  and the resistivity is a few  $\text{k}\Omega\text{cm}$ ; this gives a width of the diffusion cloud of about  $5\text{-}10 \mu\text{m}$  for a fully depleted detector. Thus, the charge cloud is far smaller than the pitch in most of the microstrip detectors in use. The variable  $\eta$  is defined in equation 6.6 where  $S_R$  is the signal on the right strip and  $S_L$  the signal on the left strip [83].

$$\eta = \frac{S_R}{S_R + S_L} \quad (6.6)$$

Since hits are uniformly distributed over the detector, the position of the cluster with respect to the left strip ( $X_\eta$ ) can be calculated using the equation 6.7, where  $f(\eta)$  is an arbitrary monotonic growing function of  $\eta$ , with  $f(0) = 0$  and  $f(1) = 1$ ,  $P$  is the readout pitch and  $dN/d\eta$  gives the differential  $\eta$  distribution. Equation 6.7 defines a non-linear algorithm with  $f(\eta)$  given by the integral of the  $\eta$  distribution, normalized to the total number of events in the distribution.

$$f(\eta) = \frac{X_\eta}{P} = \frac{\int_0^\eta \frac{dN}{d\eta} d\eta}{\int_0^1 \frac{dN}{d\eta} d\eta} \quad (6.7)$$

With the data taken in the test beam and with the tracking information projected on the

DUT plane, it was possible to extract the  $\eta$  distribution needed for the proper calculation of the x-coordinate ( $X_\eta$ ) in the sensor. The  $\eta$  distribution measured and its  $f(\eta)$  function are shown in figure 6.18.

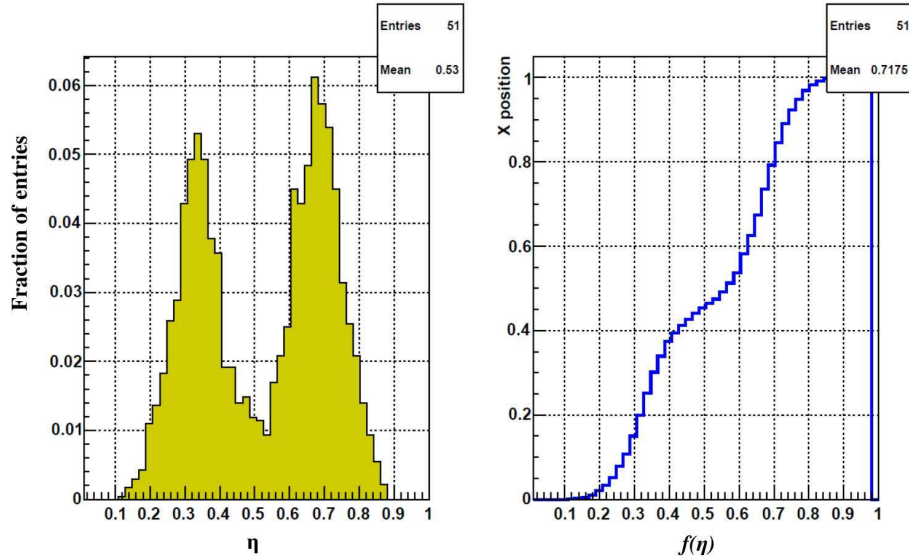


Figure 6.18: Differential  $\eta$  distribution measured during the test-beam (left), and the corresponding  $f(\eta)$  distribution (right).

The space resolution in both coordinates of the sensors was obtained as the difference between the  $(x,y)$  position of the tracks measured for the telescope and projected in the DUT plane and the  $(x,y)$  positions measured in the sensors. A correlation plot between the x-coordinates from the telescope and the DUT is shown in figure 6.19. It shows the existing synchronization in the data taking between the telescope and the DUT. Thus, in figure 6.20 is shown the measured resolution on X-coordinate that was found to be about  $26 \mu\text{m}$ , very close to the value expected for a  $80 \mu\text{m}$  pitch strip sensor ( $23 \mu\text{m}$  according to equation 6.1). In figure 6.21 is shown the measured resolution on Y-coordinate that was found to be about  $1.7 \text{ mm}$ , in a  $20 \text{ mm}$  strip length sensor with corresponded to the  $8.5 \%$  of the total length of the strip for a MIP. For this plot, only tracks with a correct measured X position were considered.

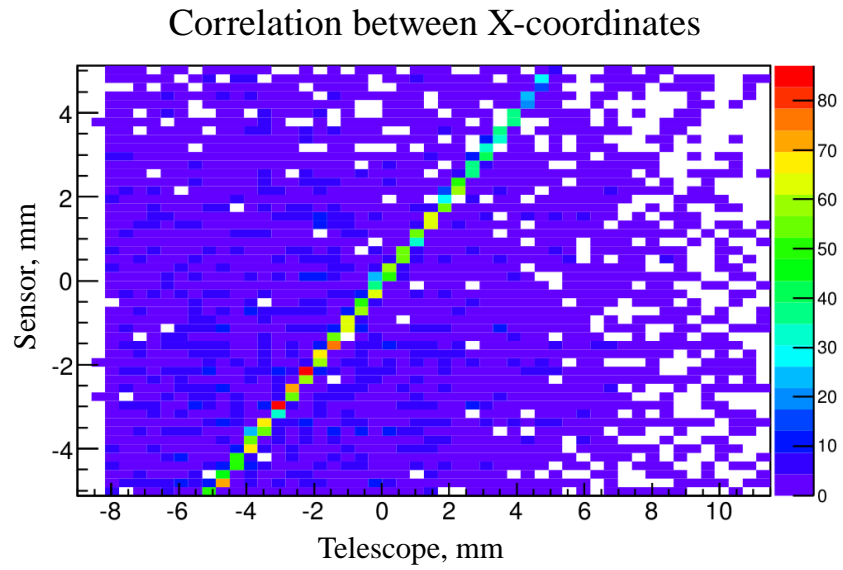


Figure 6.19: Correlation map of the tracks over the X-coordinate between telescope and DUT.

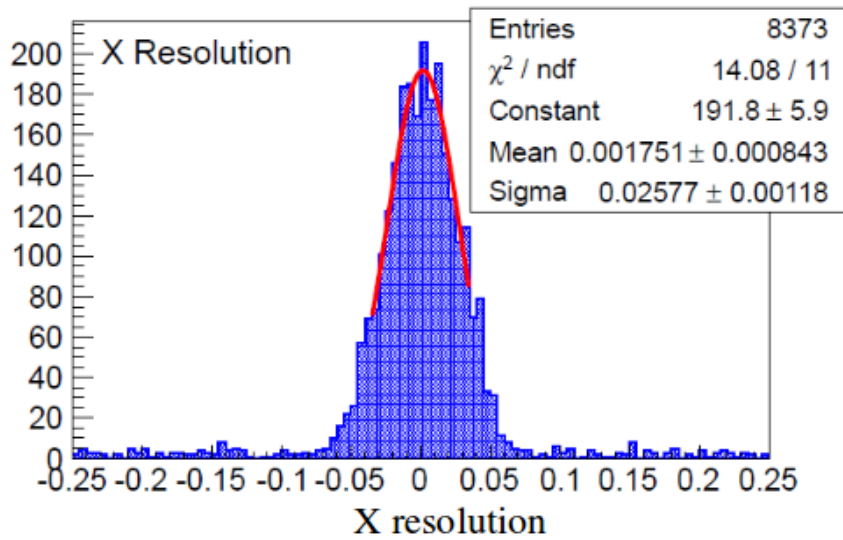


Figure 6.20: Measured resolution on X-coordinate.

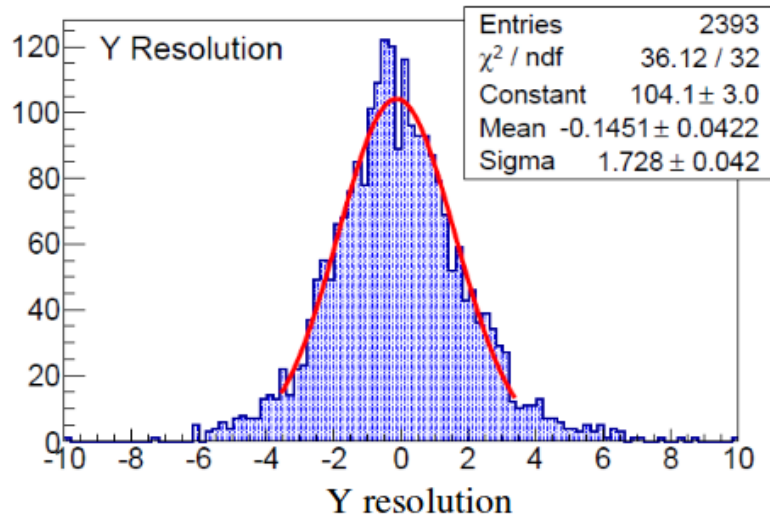


Figure 6.21: Measured resolution on Y-coordinate.



## Chapter 7

# Summary and conclusions

For the first time, a detailed radiation tolerance study of silicon diodes after a purely neutron irradiation up to fluence of  $1.6 \times 10^{16} n_{eq}/cm^2$  was carried out. This study was done on planar non segmented diodes (pads) produced by Hamamatsu using two different types of silicon growth techniques: epitaxial and deep-diffused float-zone (dd-FZ). The area of the silicon pads was  $25 \text{ mm}^2$  and the active thickness was  $50 \text{ }\mu\text{m}$  and  $100 \text{ }\mu\text{m}$  for the epitaxial devices; and  $120 \text{ }\mu\text{m}$ ,  $200 \text{ }\mu\text{m}$  and  $320 \text{ }\mu\text{m}$  for the dd-FZ diodes. Also, two types of bulk doping were studied, p-type and n-type.

The studies performed during this work provided a very important input for the Technical Proposal for the Phase II Upgrade of the Compact Muon Solenoid experiment, in which some results were included, and they confirmed the radiation hardness of this technology and the consequent viability of a future High Granularity Calorimeter (HGCal) based on silicon as an active material.

A complete set of results of the characterization of these silicon pads were presented in this work:

- In the reverse current as a function of voltages measurement (IV) was found that the reverse current normalized by the volume of the diodes scales linearly with the fluence as expected. Moreover, the evaluation of the power consumption due to the reverse current of the diodes at the end of their live in nominal conditions was found to be around 25 kW (at  $-35^\circ\text{C}$ ), only about the 25% of the total power consumption of the HGCal.

- 
- From the capacitance as a function of the voltage measurement (CV) was possible to measure the depleted volume of the diodes before irradiation. It gives a good approximation of the expected charge that can be collected for each thickness. It was done a homogeneity study among different sensors from different wafers and it was found a good homogeneity among sensors of the same type.
  - Two important points were observed combining IV and CV measurements:
    - In all the measurements with the dd-FZ diodes, is observed that the capacitance is decreasing up to 1000 V and they never reach a plateau, with the exception of the 300  $\mu\text{m}$  p-on-n. The same happens with the reverse current that grows up to 1000 V, with the exception again of the 300  $\mu\text{m}$  p-on-n. This is a strong indication that the irradiated diodes are not fully depletion in the working points studied (600 V and 800 V).
    - Meanwhile in all the measurements with the epitaxial diodes is observed that the capacitance reaches a plateau, but the reverse current keeps increasing in the full range of the bias voltages studied. Additionally, it is observed a change in the slope in the IV curves, from concave to convex. This exponential growth could be an indication of the emergence of some amplification mechanisms after irradiation.
  - The collected charge decreases with the fluence and after irradiation it reduces from 22, 16, 10 and 7  $\text{ke}^-$  to 10, 6, 4 and 6  $\text{ke}^-$ , respectively, for thicknesses of 300, 200, 120 and 100  $\mu\text{m}$  in the worst scenario. In this way, epitaxial diodes revealed a superior radiation tolerance after neutron irradiation at high fluences in comparison with the dd-FZ. The reason for this is not clear and a further investigation will be required, but this could be another indication of some amplification mechanism, as it was previously indicated. With the exception of the dd-FZ 320 diodes, where the n-on-p diodes collect less charge than the p-on-n ones, both bulk types behave similarly. This difference was not expected and needs to be further investigated, nevertheless this could be explained by the difference in the depletion volume observed in the CV measurements.
  - I developed a new test station for the study of the energy-loss fluctuations in the energy deposits of charged particles in thin sensor as a part of this work. This project was successfully carried out during my work in this thesis. This specific activity was granted by the European project AIDA-2020. Minimum ionizing particle measurement were conducted in this new test station using a  $^{90}\text{Sr}$  source for all the unirradiated diodes,

and for all the n-on-p irradiated diodes. However, at the highest fluences the signal-to-noise measured was relatively low, around two/three. It was not possible to measure the p-on-n irradiated diodes due to the high noise that appeared during the biasing. All measurements done with the  $^{90}\text{Sr}$  source are in agreement with the measurements done in the TCT characterization.

- The timing capabilities of irradiated diodes were probed in the HGICAL environment. Several test-beams were carried out in order to evaluate the timing performance of thin silicon layers when traversed by multiple simultaneous minimum ionizing particles (MIPs). It was probed that it is possible to perform precise timing measurements (below 20 ps) using silicon sensors for large pulse heights, signal higher than 20 MIPs. It was probed that it is possible to further improve timing measurements when information from several sensors are combined. This has the the potential to improve the calorimeter performance in very dense environments, such as the forward region of the High Luminosity LHC.

On the other hand, the performance of a bidimensional position-sensitive semiconductor detector concept based on the resistive charge-division readout method was studied. This detector was measured with a  $^{90}\text{Sr}$  source in order to evaluate its signal-to-noise along the longitudinal strip (the resistive one), showing that the signal-to-noise is quite uniform along the strip and giving a value around 12.5. The performance of the detector was also evaluated in a test-beam with MIPs. The readout system was successfully integrated with the EUDET telescope in order to have tracking information and measure its spacial resolution. The spacial resolution in the interstrip coordinate was found to be  $26\ \mu\text{m}$ . This value is very close to the expected one for a  $80\ \mu\text{m}$  pitch strip sensor ( $23\ \mu\text{m}$ ). The spacial resolution in the resistive coordinate was found to be 1.7 mm for a MIP in a 20 mm strip length sensor. This value correspond to the 8.5 % of the total length of the strip. These results show the feasibility of this kind of sensors for their implementation in tracking detectors for the future collider experiments.



## Chapter 8

# Resumen

### 8.1 Introducción

Durante los últimos 40 años, se han hecho grandes descubrimientos en el campo de la física de partículas, rama de la física que estudia los componentes fundamentales de la materia y las interacciones que los gobiernan. La física de partículas moderna se centra en el estudio de las partículas subatómicas gobernadas por la mecánica cuántica. En los años 70, se desarrolló el modelo estándar de la física de partículas, que a día de hoy es el modelo que mejor describe la estructura fundamental de la materia e interacciones fundamentales. Las partículas fundamentales, bloques constituyentes de la materia, se suponen indivisibles y por lo tanto no estarían compuestas por más partículas, según dicho modelo.

La principal herramienta para el descubrimiento de nuevas partículas, o el estudio de sus propiedades, son los aceleradores y colisionadores de partículas. Los más importantes son: el "Super Proton Synchrotron" (SPS) [1] donde se descubrieron los bosones W y Z, el "Large Electron-Positron Collider" (LEP) [3] donde se descubrió una nueva familia de neutrinos, el Tevatron [4] cuyo mayor logro fue el descubrimiento del quark top y por último el "Large Hadron Collider" (LHC) [2], el mayor acelerador del mundo en la actualidad, famoso por el descubrimiento en 2012 del Bosón de Higgs.

A corto plazo, los esfuerzos de la comunidad internacional en física de partículas están puestos en la explotación de todo el potencial del LHC en su futura actualización llamada High-Luminosity (HL-LHC) [12]. Pero con vistas al futuro, hay abiertos varios proyectos

---

de nuevos colisionadores para continuar investigando una vez finalicen las actividades en el HL-LHC. Los más destacados son: el "International Linear Collider" (ILC) [7], el "Compact Linear Collider" (CLIC) [8], el "Future Circular Collider" (FCC) [9] o el "Circular Electron Positron Collider" (CEPC) [10] entre otros.

De cara a la mejora del LHC prevista sobre el 2023, ver figura ??, en la cual se planea incrementar la tasa de colisiones en un factor 10 sobre su diseño original, serán necesarias una serie de mejoras tanto en el acelerador como en los experimentos que operan en él (ver figura 1.1): ATLAS [84], CMS [85], ALICE [86] y LHCb [87]. Debido al incremento en la luminosidad, uno de los principales retos para los distintos componentes será el daño por radiación que van a sufrir durante los 10 años en los que se espera esté operativo el HL-LHC. El experimento CMS planea actualizar varios componentes para poder soportar con éxito esta nueva fase [13]. Entre estos componentes se encuentra el Calorímetro, que será actualizado usando capas de sensores de silicio que cubrirán un total de 600 m<sup>2</sup>. A esta mejora en el calorímetro se le ha dado el nombre de "High Granularity Calorimeter" (HGCal), un esquema del mismo se muestra en la figura 1.2 y en la tabla 1.1 aparecen sus principales parámetros. Los sensores de silicio usados serán diodos hexagonales de entre 0.5 cm<sup>2</sup> y 1.0 cm<sup>2</sup> de área. El espesor de dichos diodos variará desde los 50 μm hasta los 300 μm y deberán ser capaces de soportar dosis de hasta 1.5 MGy y fluencias de neutrones de hasta 10<sup>16</sup>n<sub>eq</sub>/cm<sup>2</sup> en el peor de los casos.

Uno de los objetivos de este trabajo es el estudio de la viabilidad de estos sensores durante los 10 años de operación previstos del HL-LHC. Para ello, se ha llevado a cabo un estudio de tolerancia a la radiación de distintos tipos de diodos de silicio, exponiéndolos a fluencias de neutrones de hasta 1.6 × 10<sup>16</sup>n<sub>eq</sub>/cm<sup>2</sup>.

Por otro lado, de cara a los futuros experimentos de colisionadores, otro objetivo de este trabajo es el estudio de la viabilidad de un nuevo prototipo de sensores de microtiras con electrodos resistivos sensibles en dos coordenadas. Estos sensores fueron propuestos como una posible solución a incorporar en uno de los detectores del futuro ILC. En este nuevo prototipo de sensores, se incorpora el método de división de carga resistiva a lo largo de las microtiras.

## 8.2 Técnicas de caracterización

Las diferentes técnicas usadas para la caracterización de los dispositivos estudiados en esta tesis serán descritos a continuación. Las diferentes caracterizaciones se realizaron en instalaciones del Instituto de Física de Cantabria, laboratorio de detectores de estado sólido del CERN y la Universidad de Hamburgo. Las técnicas de caracterización usadas fueron:

- Caracterización eléctrica. Se basa en la medida de la corriente inversa y capacidad de los sensores en función del voltaje aplicado. Con estas caracterizaciones se pretenden estudiar diferentes aspectos de los sensores como son: el grado de calidad en la fabricación, la estimación del consumo eléctrico, la evaluación del daño por radiación o la obtención de los parámetros de funcionamiento (voltaje de vaciado y voltaje de ruptura). Un esquema del equipo usado para hacer la caracterización eléctrica de la corriente inversa en función del voltaje se muestra en la figura 3.2, mientras que el esquema usado para la medida de la capacidad en función del voltaje se muestra en la figura 3.4. Una imagen de los principales componentes del sistema de medición usado en el CERN se muestra en la figura 3.1.
- Otra técnica de caracterización usada fue la caracterización mediante láser usando la técnica "Transient Current Technique" (TCT) [39]. Esta herramienta consiste en la generación de portadores de carga dentro del sensor mediante la iluminación con un láser. Debido a la presencia de un campo eléctrico, generado al aplicar voltaje al sensor, estos portadores inducen un pulso de corriente en su recorrido hacia los electrodos del sensor. Este pulso de corriente es amplificado y medido para su posterior estudio. Un esquema del proceso se muestra en la figura 3.7, mientras que una imagen del equipo utilizado en el CERN con todos sus componentes se muestra en la figura 3.10.
- La caracterización mediante fuente radioactiva fue otra técnica empleada durante este trabajo. Para ello, se utilizó una fuente radioactiva de  $^{90}\text{Sr}$ , ver figura 3.16. En este caso, no había equipo disponible para realizar este tipo de caracterizaciones y como parte del trabajo de esta tesis se diseñó y se puso en funcionamiento un nuevo equipo dentro del departamento de detectores de estado sólido del CERN. Una imagen del equipo con todos sus elementos se muestra en la figura 3.17. El diseño y puesta en marcha del equipo de medida con fuente radioactiva fue una tarea financiada por el proyecto europeo AIDA-2020 [43]. La responsabilidad en el cumplimiento de los objetivos y plazos previstos inicialmente fue mía, teniendo que hacerme cargo del diseño, de la

---

adquisición de los equipos necesarios, del montaje de todos los componentes, de la puesta en marcha y del desarrollo del software de control y toma de datos. Para el análisis de las medidas se desarrolló otro código independiente basado en ROOT. El objetivo perseguido es la caracterización de la deposición de carga y sus fluctuaciones en sensores altamente irradiados en las condiciones de trabajo esperadas en el HL-LHC.

- Instalaciones para hacer caracterizaciones en "test-beam" también fueron usadas durante este trabajo. Se realizaron varias pruebas, todas ellas en el área norte de pruebas del SPS en el CERN [46]. En la figura 3.23 se pueden ver todas las líneas de prueba disponibles en este área. Dependiendo de la línea usada, se puede medir con diferentes tipos de partículas, pudiendo también modificar la energía de las mismas. Para una de las pruebas fue necesario tener información de la posición de impacto de las partículas en el sensor. Para ello se usó un telescopio de EUDET que está disponible como parte del servicio dado a los usuarios, en caso de ser necesario [48]. El telescopio usado fue DATURA, y cuenta con seis planos dotados con sensores de píxeles MIMOSA26. Con ellos, se puede hacer una reconstrucción adecuada de las trayectorias de las partículas y se puede llegar a definir con una precisión cercana a los  $4 \mu\text{m}$  (en el mejor de los casos) la posición de impacto en el sensor estudiado. Una imagen de este telescopio se puede ver en la figura 3.24.
- Dado que uno de los principales objetivos de este trabajo es la caracterización de sensores después de una irradiación con neutrones, una campaña de irradiación fue llevada a cabo al comienzo de este trabajo. Esta irradiación consistió en exponer a los sensores a flujos de neutrones en el reactor nuclear del centro "Jozef Stefan Institute" en Liubliana (Eslovenia) [52]. Este reactor nuclear es de tipo TRIGA Mark II y dependiendo de su potencia, el flujo de partículas (neutrones) varía entre  $2 \times 10^9 n_{eq}/\text{cm}^2\text{s}$  y  $2 \times 10^{12} n_{eq}/\text{cm}^2\text{s}$ . La precisión dada en los flujos de neutrones está dentro del 10% [39].

## 8.3 Resultados

En esta sección se resumen las caracterizaciones realizadas y los resultados más importantes obtenidos en ellas.

### 8.3.1 Daño por radiación en diodos de silicio

Los diodos estudiados para el calorímetro HGC de CMS son diodos de silicio deep-diffused float-zone (dd-FZ) y epitaxial (Epi) fabricados por Hamamatsu [56]. Estos diodos fueron estudiados en trabajos anteriores [29, 59], pero nunca después de ser irradiados con neutrones. El espesor de los diodos varía de entre los  $50 \mu\text{m}$  hasta los  $320 \mu\text{m}$  con un área de  $25 \text{ mm}^2$  y los dos tipos de dopado (p-on-n y n-on-p). Un esquema y una imagen de estos diodos se muestra en las figuras 4.3 y 4.2 respectivamente. Las fluencias a las que fueron irradiados se muestran en la tabla 4.1.

La mayor parte de los resultados de las caracterizaciones realizadas después de la irradiación fueron ya publicados [61, 62]. En todas las calibraciones las medidas se realizaron a  $-20^\circ\text{C}$  ( y  $-30^\circ\text{C}$  cuando el equipo de medida lo permitía). Los voltajes aplicados llegaron hasta los  $700 \text{ V}$  para los no irradiados y los  $1000 \text{ V}$  para los irradiados (a excepción de los diodos de  $50 \mu\text{m}$  donde solo se llegó a  $400 \text{ V}$ ). Durante las caracterizaciones eléctricas el anillo de guarda se conectó a tierra, mientras que para las medidas con láser y fuente radioactiva se dejó flotando al no tener influencia. Todas las medidas se hicieron después de un "annealing" de  $10 \text{ min}$  a  $60^\circ\text{C}$ . Las caracterizaciones realizadas fueron:

- Corriente inversa frente a voltaje. Los objetivos principales de esta caracterización son: evaluar el daño por radiación generado en el volumen del diodo y estimar el consumo eléctrico de los mismos. Para ello se mide la corriente inversa en función del voltaje aplicado al diodo. Todas las medidas realizadas se pueden ver en las figuras 4.4, 4.5, 4.6, 4.7 para los diodos dd-FZ de  $320 \mu\text{m}$ ,  $200 \mu\text{m}$ ,  $100 \mu\text{m}$  y epitaxial respectivamente. La corriente inversa medida comprende valores de entre unos pocos microamperios hasta los  $70 \mu\text{A}$ . Por lo general, la corriente inversa crece en todo el rango de voltajes estudiado. Se puede estimar el consumo de eléctrico de los diodos al final de su vida útil, que será en torno a los  $40 \text{ kW}$  si la temperatura de operación es de  $-30^\circ\text{C}$ . Normalizando el incremento de corriente inversa generado por la radiación por el volumen del diodo y representando este valor frente a la fluencia se puede estimar el daño por radiación. La pendiente del ajuste lineal mide el daño por radiación [34]. En las figuras 4.8 y 4.9 se muestra los resultados de este cálculo. Se puede observar que la corriente inversa normalizada por el volumen escala linealmente con la fluencia y los datos se ajustan al valor usado habitualmente como referencia [34]. En la figura 4.10 se muestran medidas de la corriente inversa en función de la temperatura. Se observa la dependencia esperada según la ecuación 2.15

- 
- Capacidad frente a voltaje. Tiene también dos objetivos que son: la medida de la capacidad y como resultado directo el cálculo del espesor del diodo usando la ecuación 3.1. Esta ecuación solo es aplicable en el caso de los diodos no irradiados. Los resultados de esta caracterización se muestran en las figuras 4.11, 4.12, 4.13, 4.14 y 4.15 para los diodos dd-FZ de 320  $\mu\text{m}$ , 200  $\mu\text{m}$ , 100  $\mu\text{m}$ , Epi 100  $\mu\text{m}$  y Epi 50  $\mu\text{m}$  respectivamente. Las capacidades medidas varían desde los 9 pF hasta los 60 pF y los espesores obtenidos antes de ser irradiados se muestran en la tabla 4.2. Se realizó también un estudio de homogeneidad entre varios diodos del mismo tipo pertenecientes a diferentes obleas y los resultados se muestran en la figura 4.16 y tabla 4.3. No se apreció variación importante entre distintos diodos de una misma oblea, ni entre diodos de diferentes obleas.
  - Caracterización con láser. El principal objetivo de estas medidas es la estimación de la eficiencia en la colección de la carga (CCE) siempre relativa al diodo no irradiado que se usa como referencia. Para ello se usa la técnica TCT, antes descrita, con láser infrarrojo. Las medidas realizadas de CCE se muestran en las figuras 4.17, 4.18, 4.19, 4.20 y 4.21 y ejemplos de las forma de onda medidas a 600 V se muestran en las figuras 4.22, 4.23, 4.24, 4.25 y 4.26 para todos los diodos. Se observa una clara pérdida de señal después de la irradiación y los pulsos en las formas de onda son más pequeños y estrechos como regla general. Un resumen de estas medidas se puede ver en la figura 4.27 donde es más sencillo comparar los distintos tipos de diodos. En esta gráfica se ve con claridad la menor degradación de los diodos epitaxiales en lo que a colección de carga se refiere.
  - Caracterización con fuente radioactiva. El objetivo de esta caracterización es evaluar con partículas de mínima energía de ionización la deposición de carga en los diodos. Esta se parametriza con una distribución de Landau. Para ello, se usa una fuente radioactiva de  $^{90}\text{Sr}$  y el ajuste de las distribuciones de carga se hace con una función de ajuste Landau convolucionada con una Gaussiana (para ajustar las componentes no Gaussianas en la deposición de carga y el ruido electrónico). Las distribuciones de carga obtenidas a 400 V se muestran en las figuras 4.36, 4.37, 4.38, 4.39 y 4.40. Como se esperaba, el valor más probable y la anchura de la Landau disminuyen con en los diodos irradiados. Del mismo modo, el ruido medido aumenta con la capacidad del sensor y la fluencia. Las tablas 4.4 y 4.5 resumen los parámetros fundamentales extraídos de los ajustes. En la figura 4.41 se compara la carga medida con fuente radioactiva de  $^{90}\text{Sr}$  y con la medida usando TCT; se observan resultados muy similares, salvo en el caso de los diodos altamente irradiados.

### 8.3.2 Resolución temporal en diodos de silicio

Para poder medir la resolución temporal de los diodos dd-FZ se realizaron una serie de test-beams en los que primero se midieron los diodos no irradiados, por simplicidad al poder medirse a temperatura ambiente, y posteriormente los irradiados, medidos a casi  $-30^{\circ}\text{C}$ . El montaje realizado y los equipos utilizados se muestran en las figuras 5.1 para los diodos no irradiados y 5.2 para los diodos irradiados. En el caso de los no irradiados, se midieron dos sensores al mismo tiempo usando como señal de referencia la procedente de los "micro-channel plates" (MCP). Las señales fueron digitalizadas y analizadas offline con un convertidor AD V1742 de la marca CAEN. Las señales de los diodos fueron amplificadas usando amplificadores de corriente CIVIDEC [40]. Para incrementar la señal en los diodos, se colocaron placas de plomo entre el haz y los diodos, no así para hacer la calibración frente a MIP. En el caso de los diodos irradiados, se midieron seis diodos al mismo tiempo y se usaron como referencia dos diodos no irradiados, validados en el primer test-beam.

En el análisis, se definieron los tiempos de los pulsos como el tiempo en el que la amplitud de la señal alcanza el 50% de su valor máximo. En la figura 5.4, se muestra el resultado de la calibración frente a MIP, resultando lineal para los tres espesores estudiados. El estudio de la resolución temporal se hizo usando tres configuraciones distintas:

- Usando como referencia uno de los diodos 5.10. Esta fue la única configuración estudiada en el caso de los diodos irradiados, figura 5.11.
- Usando los MPC como referencia, figure 5.12.
- Usando los MCP como referencia, pero estudiando la señal combinada de los dos diodos, figure 5.13.

Se observa que la resolución temporal de un único diodo, si la señal es suficientemente grande, está por debajo de los 20 ps, si la señal es baja (del orden de unos pocos MIPs) su comportamiento empeora notablemente. Esta observación es igualmente válida para los diodos irradiados. Otra conclusión es que si se combinan las señales de varios diodos, la resolución temporal mejora notablemente.

---

### 8.3.3 Detectores de microtiras sensibles en dos coordenadas

Un nuevo diseño de sensores de microtiras sensibles en las dos direcciones fue caracterizado en este trabajo. Estos sensores de microtiras incluyen electrodos resistivos de tal forma que es posible leer la señal en ambos extremos de la microtira, aprovechando así la división de carga resistiva. La posición en la coordenada resistiva se calcula según la ecuación 6.2. En la otra coordenada (transversal), la división de carga capacitiva entre microtiras nos da la posición. La figura 6.1 muestra un esquema del funcionamiento de este novedoso sensor.

Se realizaron dos tipos de caracterizaciones:

- Caracterización con fuente radiactiva  $^{90}\text{Sr}$ , donde fue posible verificar que la relación señal/ruido es constante a lo largo del strip resistivo, dando un valor de 12.5. Ver figura 6.11.
- Caracterización en test-beam para medir la resolución espacial en ambas coordenadas. La resolución obtenida fue de  $26\ \mu\text{m}$  en la coordenada transversal y de  $1.7\ \text{mm}$  en la coordenada longitudinal (resistiva). En la figura 6.14, se pueden ver los sensores montados en el test-beam junto con el resto de elementos.

## 8.4 Conclusiones

Por primera vez, fue realizado un estudio detallado del daño por radiación en diodos de silicio después de una irradiación únicamente con neutrones, habiendo sido irradiados hasta fluencias de  $1.6 \times 10^{16} \text{neq}/\text{cm}^2$ . Este estudio fue llevado a cabo con diodos de  $25\ \text{mm}^2$  de área, fabricados usando dos técnicas de crecimiento de silicio: "deep-defused float zone" y "epitaxial". Fueron estudiados diodos con dos tipos de dopado (n-on-p y p-on-n) y de diferentes grosores:  $50\ \mu\text{m}$  y  $100\ \mu\text{m}$  para los "epitaxiales" y  $120\ \mu\text{m}$ ,  $200\ \mu\text{m}$  y  $320\ \mu\text{m}$  para los "deep-defused float zone".

Los estudios realizados en este trabajo proporcionaron importantes resultados que fueron incluidos en el "Technical Proposal" para la actualización del experimento CMS [13]. Estos resultados confirmaron la resistencia a radiación de los diodos y la viabilidad del futuro calorímetro (HGCAL) para el experimento CMS.

En este trabajo se ha presentado una completa caracterización de los diodos, cuyos resultados más importantes se enumeran a continuación:

- En la caracterización eléctrica de la corriente inversa frente a voltaje, se puede destacar que la corriente medida normalizada por el volumen del diodo escalan linealmente con la fluencia tal y como se esperaba. La estimación del consumo de potencia de los diodos al final de su vida útil, será en torno al 25% de la potencia total consumida por el calorímetro. Lo cual no representa un mayor problema en términos de consumo de potencia o disipación de calor.
- En la caracterización eléctrica de capacidad frente a voltaje, se midió el volumen vaciado de los diodos antes de ser irradiados, el cual proporciona una buena aproximación de la carga que se espera coleccionen para cada espesor. Se realizó un estudio de homogeneidad de los diferentes obleas usadas con los datos de la campaña realizada para la actualización del detector de trazas de CMS. Se observó una buena homogeneidad en todos los sensores de distintas obleas (dentro del 5%).

Comparando los resultados de las caracterizaciones IV y CV, se pueden destacar dos puntos importantes:

- Centrándose en los resultados de los diodos dd-FZ de  $300 \mu\text{m}$ , se ve en las curvas de capacidad que solo los diodos p-on-n llegan a depletar, pero ya a voltajes superiores a 700-800 V, mientras que en los n-on-p la capacidad sigue disminuyendo en todo el rango medido (hasta 100 V). Esto se confirma con las curvas de corriente inversa, donde los p-on-n llegan a alcanzar un plato pero no así los n-on-p, donde la corriente inversa continúa creciendo hasta los 1000 V. Estos son claros indicios de que los diodos no están completamente depletados debido al daño sufrido por radiación.
- El segundo punto tiene que ver con indicios de mecanismos de amplificación observados en los diodos epitaxiales. Centrándose en los resultados IV y CV de los diodos epitaxiales de  $100 \mu\text{m}$ , se ve en las curvas CV como la capacidad llega a saturar por encima de 400 V, mientras que la corriente inversa continúa creciendo de forma exponencial. Esto podría ser explicado por la presencia de mecanismos de amplificación generados por el daño por radiación.
- De la caracterización con láser se estimó que la carga coleccionada por los diodos se reduce de 22, 16, 10, y  $7 \text{ Ke}^-$  a 10, 6, 4,  $6 \text{ Ke}^-$ , respectivamente para los espesores de

---

320, 200, 120 y 100  $\mu\text{m}$  en el peor de los casos. Sorprendentemente, los diodos "epitaxiales" presentaron una mayor resistencia a la radiación de lo esperado, comparando los resultados con los diodos dd-FZ. Esto podría ser debido, tal y como se indicó en el punto anterior, a la presencia de algún mecanismo de amplificación. Otro punto a destacar es que diodos n-on-p y p-on-n presentan una degradación similar, salvo en el caso de los diodos dd-FZ de 300  $\mu\text{m}$ . No está del todo claro porque sucede esto, pues se esperaría una degradación similar, pero una explicación es que tal y como se comentó anteriormente, los diodos n-on-p tendrían un volumen vaciado mucho menor a los voltajes de operación. Estos dos puntos tienen que ser investigados en más detalle, para entender los motivos de estas diferencias.

- Financiado por el proyecto europeo AIDA-2020 [43] y con el objetivo de estudiar las fluctuaciones en las deposiciones de carga con fuente radioactiva en sensores de silicio altamente irradiados, puse en funcionamiento un nuevo equipo dentro del departamento de estado sólido del CERN. Con este equipo, fue posible estudiar la respuesta de estos sensores al ser medidos con partículas de ionización mínima (MIPs). No fue posible medir los diodos p-on-n irradiados debido a la aparición de un ruido anormal durante la alimentación. Los diodos más irradiados presentan una relación señal/ruido muy baja, pero fue posible medirlos. Los resultados concuerdan con las medidas hechas con láser.
- La resolución temporal de los diodos dd-FZ fue medida en varios test-beams. Se demostró que se puede llegar a tener una resolución temporal con estos diodos de hasta 20 ps, si la señal medida es superior a 20 MIPs. No se observó un deterioro de la resolución temporal con la radiación. Se comprobó que si se combina la información de varios diodos, la resolución temporal mejora. Estos resultados son muy prometedores a la hora de mejorar el comportamiento de los calorímetros en ambientes con altos índices de colisiones, como es el caso del HL-LHC.
- Por último, el comportamiento de un nuevo sensor de microtiras sensible en las dos coordenadas basado en el método de división de carga resistiva fue estudiado. Este sensor fue medido con una fuente de  $^{90}\text{Sr}$  para medir su relación señal/ruido a lo largo de las tiras resistivas, mostrando un valor bastante constante a lo largo de toda la tira de 12.5. Se evaluó también su comportamiento en un test-beam, donde por primera vez se pudo sincronizar con el telescopio EUDET para poder tener información sobre la trayectorias de las partículas. Con esta información fue posible evaluar su resolución espacial resultando ser de unos 26  $\mu\text{m}$  en la coordenada transversal a las tiras y de unos 1.7 mm en la coordenada longitudinal a las tiras (la resistiva). Estos valores son los esperados

para esta geometría de sensores, quedando probado el adecuado comportamiento de estos sensores para su uso en experimentos de aceleradores.



## Appendix A

# Acronyms

**AIDA** → Advanced European Infrastructures for Detectors at Accelerators

**ALICE** → A Large Ion Collider Experiment

**APDs** → Silicon Avalanche Photodiodes

**ATLAS** → A Toroidal LHC ApparatuS

**BH** → Backing Hadron Calorimeter

**CALICE** → Calorimeter for Linear Collider Experiment

**CCE** → Charge Collection Efficiency

**CEPC** → Circular Electron Positron Collider

**CERN** → European Organization for Nuclear Research

**CLIC** → Compact Linear Colider

**CMS** → Compact Muon Solenoid

**CSC** → Cathode Strip Chambers

**CV** → Capacitance as a function of the Voltage

**CVD** → Chemical Vapour Deposition

**Cz** → Czochralski process

---

**DATURA** → DESY Advanced Telescope Using Readout Acceleration

**dd-FZ** → Deep-diffused Float-zone

**DT** → Drift Tubes

**DUT** → Device Under Test

**ECAL** → Electromagnetic Calorimeter

**EE** → Electromagnetic Calorimeter

**Epi** → Epitaxial

**FCC** → Future Circular Collider

**FH** → Front Hadron Calorimeter

**FWHM** → Full Width at Half Maximum

**FZ** → Float-zone

**HCAL** → Hadron Calorimeter

**HEP** → High Energy Physics

**HGCAL** → High Granularity Calorimeter

**HL-LHC** → High Luminosity Large Hadron Collider

**HV** → High Voltage

**IFCA** → Instituto de Física de Cantabria

**ILC** → International Linear Collider

**IV** → Current as a function of the Voltage

**LEP** → Large Electron-Positron Collider

**LHC** → Large Hadron Collider

**LHCb** → Large Hadron Collider beauty

**MCP** → Micro Channel Plates

**MCz** → Magnetic Czochralski technique

**MIP** → Minimum Ionizing Particle

**MPV** → Most Probable Value

**NIEL** → Non Ionizing Energy Lost

**PH-DT** → Detector Technologies group in the Experimental Physics department at CERN

**PKA** → Primary Knock on Atom

**PMT** → Photomultiplier

**PS** → Proton Synchrotron

**RH** → Relative Humidity

**RMS** → Root Mean Square

**RPC** → Resistive Plate Chambers

**SiPM** → Silicon Photomultiplier

**SM** → Standard Model

**S/N** → Signal-to-noise

**SNR** → Signal-to-noise Ratio

**SPPC** → Super Proton-Proton Collider

**SPS** → Super Proton Synchrotron

**SSD** → Solid State Department

**SUSY** → super-symmetry

**TCT** → Transient Current Technique

**TLU** → Trigger Logic Unit

**ToT** → Time Over Threshold

**VPE** → Vapour Phase Epitaxy



# List of Figures

1.1	Schematic map of the CERN accelerator complex. . . . .	3
1.2	Technical drawing of the HGICAL overall structure. . . . .	7
1.3	Carbon-fiber structure and cassettes illustration. . . . .	8
1.4	Location of the different sensors according to their active thickness. . . . .	9
2.1	An schematic of the pn-junction with space charge density profile and electric field. . . . .	18
2.2	Principle of a semiconductor detector. . . . .	21
2.3	Schematic representation of the Czochralski process. . . . .	23
2.4	Schematic representation of the float zone crystal growth. . . . .	24
2.5	Diffusion of dopants in a silicon wafer and schematic of its doping profile. . .	25
2.6	Initial distributions of vacancies by 10 MeV protons, 24 GeV/c protons and 1 MeV neutrons. . . . .	27
2.7	Fluence dependence of reverse current for silicon detectors produced by various process technologies. . . . .	31
2.8	Alpha value as a function of the annealing time at different temperatures. . .	32
2.9	Change in the depletion voltage respectively the absolute effective doping concentration as measured immediately after irradiation. . . . .	33

---

3.1	Main components of the IV/CV set-up used at CERN for the electrical characterization. . . . .	37
3.2	Schematic view of the IV set-up. . . . .	38
3.3	Current-voltage characteristic of an unirradiated silicon diode at different temperatures. . . . .	39
3.4	Schematic view of the CV set-up. . . . .	39
3.5	Equivalent circuit of a reverse-biased diode. . . . .	40
3.6	Capacitance-voltage characteristic of a silicon diode before and after neutron irradiation. . . . .	41
3.7	Location of the charge carriers generated with two types of laser sources (red and IR). . . . .	43
3.8	Comparison between two TCT pulses taken with IR laser and red laser. . . .	43
3.9	A schematic of a TCT set-up. . . . .	44
3.10	main systems of the TCT set-up at CERN. . . . .	45
3.11	Diode glued on a pcb. . . . .	45
3.12	Schematic of the optical system in the TCT set-up at CERN. . . . .	46
3.13	IR laser intensity as a function of the position of the manual attenuator. . . . .	47
3.14	IR laser intensity as a function of the laser intensity measured in the reference diode. . . . .	47
3.15	Charge collected with IR laser in a dd-FZ 300 $\mu\text{m}$ p-type silicon diode. . . . .	48
3.16	Energy spectrum emitted from the $^{90}\text{Sr}$ source and Bethe-Bloch graph for beta electron absorption in silicon. . . . .	49
3.17	Main elements of the new test station for the study of the landau fluctuation in thin silicon layes. . . . .	50

3.18	Average signal taken in an unirradiated dd-FZ 320 $\mu\text{m}$ diode with the $^{90}\text{Sr}$ source. . . . .	52
3.19	Noise distributions in the measurements. . . . .	53
3.20	Fitting of the charge distribution using a convoluted Landau and Gaussian function. . . . .	54
3.21	Calibration plot of the internal ACD of the oscilloscope. . . . .	55
3.22	Calibration plot of the charge amplifier. . . . .	55
3.23	Schematic view of the different lines in the SPS North Area test beam facility. . . . .	57
3.24	EUDET type beam telescope at DESY. . . . .	58
4.1	Equivalent 1 MeV neutron fluence for Phase-II endcap calorimetry at HL-LHC. . . . .	62
4.2	Front side and back plane of one p-on-n diode. . . . .	63
4.3	Schematic of the diodes studied in this work. . . . .	63
4.4	IV measurements for all the irradiated dd-FZ 320 $\mu\text{m}$ diodes. . . . .	65
4.5	IV measurements for all the irradiated dd-FZ 200 $\mu\text{m}$ diodes. . . . .	66
4.6	IV measurements for all the irradiated dd-FZ 120 $\mu\text{m}$ diodes. . . . .	66
4.7	IV measurements for all the irradiated epitaxial diodes. . . . .	67
4.8	Reverse currents as a function of neutron fluence at 600 V. . . . .	68
4.9	Reverse currents, as a function of neutron fluence at 800 V. . . . .	69
4.10	Measurements of the bulk current as a function of the temperature. . . . .	70
4.11	CV measurements for all dd-FZ 320 $\mu\text{m}$ diodes. . . . .	71
4.12	CV measurements for all dd-FZ 200 $\mu\text{m}$ diodes. . . . .	72
4.13	CV measurements for all dd-FZ 120 $\mu\text{m}$ diodes. . . . .	72

---

4.14	CV measurements for all epitaxial 100 $\mu\text{m}$ diodes. . . . .	73
4.15	CV measurements for all epitaxial 50 $\mu\text{m}$ diodes. . . . .	73
4.16	CV measurements for all the unirradiated diodes measured for the CMS tracker upgrade. . . . .	75
4.17	Charge collection efficiency for all the dd-FZ 320 $\mu\text{m}$ thickness diodes. . . .	77
4.18	Charge collection efficiency for all the dd-FZ 200 $\mu\text{m}$ thickness diodes. . . .	78
4.19	Charge collection efficiency measurements for all the dd-FZ 120 $\mu\text{m}$ thickness diodes. . . . .	78
4.20	Charge collection efficiency measurements for all the Epitaxial 100 $\mu\text{m}$ thickness diodes. . . . .	79
4.21	Charge collection efficiency measurements for all the Epitaxial 50 $\mu\text{m}$ thickness diodes. . . . .	79
4.22	TCT spectra at 600 V for all the dd-FZ 320 $\mu\text{m}$ thickness diodes. . . . .	80
4.23	TCT spectra at 600 V for all the dd-FZ 200 $\mu\text{m}$ thickness diodes. . . . .	80
4.24	TCT spectra at 600 V for all the dd-FZ 120 $\mu\text{m}$ thickness diodes. . . . .	81
4.25	TCT spectra at 600 V for all the Epitaxial 100 $\mu\text{m}$ thickness diodes. . . . .	81
4.26	TCT spectra at 300 V for all the Epitaxial 50 $\mu\text{m}$ thickness diodes. . . . .	82
4.27	Signal ( $e^-/\mu\text{m}$ ) extracted from the TCT measurements for the different diodes.	82
4.28	Signal ( $ke^-$ ) extracted from the TCT measurements for the different diodes. .	83
4.29	Surface scan with infrared laser top illumination on the dd-FZ diodes. . . . .	83
4.30	Surface scan with infrared laser top illumination on the epitaxial diodes. . . .	84
4.31	Reproducibility of the TCT measurements using IR laser top illumination. . .	85
4.32	Edge-TCT measurement done in a fully depleted unirradiated dd-FZ 320 n-on-p $\mu\text{m}$ diode. . . . .	86

4.33	Charge distribution measured with $^{90}\text{Sr}$ for all the unirradiated diodes. . . . .	87
4.34	Charge distribution measured with $^{90}\text{Sr}$ for all the unirradiated diodes. MPV shifted to 0. . . . .	88
4.35	Comparison between the thickness ratio and the charger ratio measured with the $^{90}\text{Sr}$ (MPV). . . . .	89
4.36	Charge distribution measured with $^{90}\text{Sr}$ for all dd-FZ 320 $\mu\text{m}$ n-on-p diodes. .	89
4.37	Charge distribution measured with $^{90}\text{Sr}$ for all dd-FZ 200 $\mu\text{m}$ n-on-p diodes. .	91
4.38	Charge distribution measured with $^{90}\text{Sr}$ for all dd-FZ 120 $\mu\text{m}$ n-on-p diodes. .	91
4.39	Charge distribution measured with $^{90}\text{Sr}$ for all Epi 100 $\mu\text{m}$ n-on-p diodes. . .	92
4.40	Charge distribution measured with $^{90}\text{Sr}$ for all Epi 50 $\mu\text{m}$ n-on-p diodes. . . .	92
4.41	Comparison between the signal ( $\text{ke}^-$ ) extracted from the TCT and the $^{90}\text{Sr}$ measurements. . . . .	93
5.1	The schematic of the layout displays the main components and the readout scheme. . . . .	97
5.2	Schematic of the set-up for the irradiated diodes test-beam. . . . .	97
5.3	Cold box with the three sets of diodes inside. . . . .	98
5.4	Comparison of the diodes response to MIPs as a function of their thickness. .	99
5.5	Reconstructed multi-MIP signal from the beam data. . . . .	101
5.6	Examples of single pulse shapes from two diodes for the same event. . . . .	102
5.7	The average pulse-shapes from different thickness diodes. . . . .	103
5.8	Rise time measured with IR laser for the irradiated diodes. . . . .	104
5.9	Rise time as a function of the temperature. . . . .	104

---

5.10	The timing resolution based on two diodes as a function of the effective signal and signal-to-noise ration. . . . .	105
5.11	Time resolution as a function of the S/N for the irradiated dd-FZ 320 $\mu\text{m}$ . . .	106
5.12	The timing resolution between the signal of the first diode and the MCP as a function of the effective signal and signal-to-noise ratio. . . . .	106
5.13	The timing resolution between the mean signal of the two diodes and the MCP as a function of the effective signal and signal-to-noise ratio. . . . .	107
6.1	Schematic view of the novel 2D position microstrip sensor. . . . .	111
6.2	IV-curves and CV-curves from the two 2D-position sensitive prototypes. . . .	113
6.3	Photo of one of the detectors mounted on the Alibava daughter board. . . . .	113
6.4	Schematic of one of the 80 cells used to model the detector. . . . .	114
6.5	Linear dependence of the position and residuals. . . . .	115
6.6	Experimental results compared with the simulation. . . . .	116
6.7	Noise values for the $A_1$ signal along the strip scanning points. . . . .	117
6.8	Correlation coefficients $\rho$ at the different laser scan points. . . . .	118
6.9	Fractional position measurement error at each scanning point. . . . .	119
6.10	Schematic of the set-up used for the S/N studies. . . . .	120
6.11	Charge distribution and measured at one position close to the centre of the strip with the $^{90}\text{Sr}$ radioactive source. . . . .	120
6.12	Signal-no-noise measured along the strips. . . . .	121
6.13	Reconstructed spot positions and their errors. . . . .	122
6.14	Picture and schematic of the set-up used during the test-beam. . . . .	123
6.15	Signal-to-noise ration measured during the test-beam. . . . .	124

6.16 Pion beam profile measured on the sensor. . . . .	125
6.17 Residuals of the particle tracks in one plane of the telescope. . . . .	126
6.18 $\eta$ distribution measured during the test-beam. . . . .	127
6.19 Correlation map of the tracks over the X-coordinate between telescope and DUT. . . . .	128
6.20 Measured resolution on X-coordinate. . . . .	128
6.21 Measured resolution on Y-coordinate. . . . .	129



# List of Tables

1.1	Parameters of the EE, FH and BH. . . . .	7
1.2	Silicon sensor arrangement: thickness of active silicon layer in the EE and FH & BH, with the associated cell size and capacitance. . . . .	10
4.1	Summary of sensor types and irradiation fluences covered in this work. . . . .	64
4.2	Pad sensors' main parameters before irradiation. . . . .	74
4.3	Homogeneity study results. . . . .	74
4.4	Landau parameters distribution for all the unirradiated diodes. . . . .	88
4.5	Landau parameters distribution for all the irradiated diodes. . . . .	90
6.1	Main parameters of the two sensor prototypes. . . . .	112



# Bibliography

- [1] The Super Proton Synchrotron. <https://home.cern/about/accelerators/super-proton-synchrotron>.
- [2] The Large Hadron Collider. <http://www.fnal.gov/pub/tevatron/tevatron-accelerator.html>.
- [3] The Large Electron-Positron Collider. <https://home.cern/about/accelerators/large-electron-positron-collider>.
- [4] Tevatron. <http://www.fnal.gov/pub/tevatron/tevatron-accelerator.html>.
- [5] CERN Document Server. <https://cds.cern.ch/record/1621583>.
- [6] Vladimir Shiltsev. *Crystal Ball: On the Future High Energy Colliders*. PoS, EPS-HEP2015:515, 2015.
- [7] ILC: International Linear Collider. <https://www.linearcollider.org/ILC>.
- [8] CLIC: Compact Linear Collider. <http://clic-study.web.cern.ch>.
- [9] The Future Circular Collider. <https://home.cern/about/accelerators/future-circular-collider>.
- [10] Jingyu Tang et al. *Concept for a Future Super Proton-Proton Collider*. 2015.
- [11] CERN Council: The European Strategy for Particle Physics. <https://council.web.cern.ch/en/content/european-strategy-particle-physics>.
- [12] The High-Luminosity LHC. <https://home.cern/topics/high-luminosity-lhc>.

- 
- [13] J Butler, D Contardo, M Klute, J Mans, and L Silvestris. *Technical Proposal for the Phase-II Upgrade of the CMS Detector*. Technical Report CERN-LHCC-2015-010. LHCC-P-008, CERN, Geneva, Jun 2015.
- [14] Ties Behnke, Chris Damerell, John Jaros, Akiya Miyamoto, Wladyslaw Dabrowski, Jan Gajewski, Marek Idzik, Danuta Kisielewska, Szymon Kulis, Leszek Suszycki, et al. *ILC Reference Design Report Volume 4 - Detectors*. 2007.
- [15] *HGCAL: A High-Granularity Calorimeter for the Endcaps of CMS at HL-LHC*. <http://www.bo.infn.it/sminiato/sienal6.html>, October 2016.
- [16] Jerome K. Carman et al. *Longitudinal resistive charge division in multi-channel silicon strip sensors*. *Nucl. Instrum. Methods Phys. Res., A*, 646(1):118 – 125, 2011.
- [17] D Bassignana, M Fernandez, R Jaramillo, M Lozano, F J Munoz, G Pellegrini, D Quirion, and I Vila. *First investigation of a novel 2D position-sensitive semiconductor detector concept*. *Journal of Instrumentation*, 7(02):P02005, 2012.
- [18] Daniela Bassignana. *New technologies of silicon position-sensitive detectors for future tracker systems*. PhD thesis, Barcelona, Inst. Microelectron., 2012.
- [19] E. Curras et al. *2D position sensitive microstrip sensors with resistive charge division along the strip*. 37th International Conference on High Energy Physics, ICHEP 2014, Valencia (Spain).
- [20] Helmuth Spieler. *Semiconductor Detector Systems*. Oxford University Press, 2005.
- [21] Simon M. Sze. *Physics of Semiconductor Devices*. A Wiley-Interscience Publication, 2 edition, 1981.
- [22] Nicola Pacifico and Mauro De Palma. *Radiation damage study on innovative silicon sensors for the CMS tracker upgrade*. PhD thesis, Bari U., Dec 2011. Presented 07 May 2012.
- [23] Simon Ramo. *Currents induced by electron motion*. *Proc. Ire.*, 27:584–585, 1939.
- [24] Jorn Lange. *Radiation Damage in Proton Irradiated Epitaxial Silicon Detectors*. PhD thesis, Hamburg U., 2008.
- [25] HyperPhysics. <http://hyperphysics.phy-astr.gsu.edu/hbase/Tables/elabund.html>.

- [26] *Ein neues Verfahren zur Messung der Kristallisationsgeschwindigkeit der Metalle.* A. Phys. Chem., 92(219), 1918.
- [27] Silicon growth techniques. [http://meroli.web.cern.ch/meroli/Lecture\\_silicon\\_floatzone\\_czochralski.html](http://meroli.web.cern.ch/meroli/Lecture_silicon_floatzone_czochralski.html).
- [28] Manijeh Razeghi. *Technology of Quantum Devices.* Springer US, pages 41-79, United States, 2010.
- [29] Joachim Erfle. *Irradiation study of different silicon materials for the CMS tracker upgrade.* PhD thesis, U. Hamburg, Dept. Phys., 2014.
- [30] M. Huhtinen. *Simulation of non-ionising energy loss and defect formation in silicon.* Nucl. Instrum. Methods Phys. Res., A, 491(1-2):194 – 215, 2002.
- [31] M.S Lazo, D.M. Woodall and P.J. McDaniel. *Silicon and Silicon dioxide neutron damage functions.* SAND87-0098-Vol1, pages 85-104, United States, 1987.
- [32] Messenger, G C and Ash, Milton S. *The Effects of Radiation on Electronic Systems.* Van Nostrand Reinhold, New York, 1986.
- [33] A. Chilingarov. *Temperature dependence of the current generated in Si bulk.* JINST, 8(10):P10003, 2013.
- [34] Michael Moll. *Radiation damage in silicon particle detectors: Microscopic defects and macroscopic properties.* PhD thesis, Hamburg U., 1999.
- [35] R Wunstorf. *A Systematic investigation of the radiation hardness of silicon detectors for high-energy physics experiments.* PhD thesis, DESY, 1992.
- [36] M. Mikuž et al. *Study of anomalous charge collection efficiency in heavily irradiated silicon strip detectors.* Nucl. Instrum. Methods Phys. Res., A, 636(1, Supplement):S50 – S55, 2011.
- [37] Gianluigi Casse et al. *Enhanced efficiency of segmented silicon detectors of different thicknesses after proton irradiations up to  $1 \times 10^{16} n_{eq} cm^2$ .* Nucl. Instrum. Methods Phys. Res., A, 624(2):401 – 404, 2010.
- [38] E. Borch, M. Bruzzi, S. Pirollo, and S. Sciortino. *Temperature and frequency dependence of the capacitance of heavily irradiated silicon diodes.* Solid State Electronics, 42:2093–2096, November 1998.

- 
- [39] Gregor Kramberger, Vladimir Cindro, and Marko Mikuz. *Signal development in irradiated silicon detectors*. PhD thesis, Ljubljana U., Ljubljana, 2001. Presented 21 Jun 2001.
- [40] Cividec. <https://cividec.at/>.
- [41] Paola La Rocca and Francesco Riggi. *Absorption of beta particles in different materials: an undergraduate experiment*. *European Journal of Physics*, 30(6):1417, 2009.
- [42] H. Spieler. *Energy Deposition in the Detector and Spectrum Formation-1. Lecture Notes - Physics 198, Spring Semester 1999 - UC Berkeley*, 1999.
- [43] AIDA2020, Advanced European Infrastructures for Detectors at Accelerators.
- [44] R. Brun and F. Rademakers. *ROOT: An object oriented data analysis framework*. *Nucl. Instrum. Meth.*, A389:81–86, 1997.
- [45] Kurt Siegfried Kölbig and Benno Schorr. *A program package for the Landau distribution*. *Comput. Phys. Commun.*, 31(CERN-DD-83-18):97–111. 21 p, Jun 1983. Erratum published in 2008: *Comput. Phys. Commun.* 178 (2008) 972.
- [46] CERN Engineering Department: Beam lines PS and SPS.  
<http://sba.web.cern.ch/sba/BeamsAndAreas/ExpList.asp>.
- [47] AIDA2020, Advanced European Infrastructures for Detectors at Accelerators.  
<http://aida2020.web.cern.ch/content/cern>.
- [48] I. Rubinskiy. *An EUDET/AIDA Pixel Beam Telescope for Detector Development*. *Physics Procedia*, 37:923 – 931, 2012.
- [49] Hendrik Jansen. *Resolution studies with the DATURA beam telescope*. *JINST*, 11(12):C12031, 2016.
- [50] EUDET-type beam telescopes. [https://telescopes.desy.de/Main\\_Page](https://telescopes.desy.de/Main_Page).
- [51] C. Hu-Guo et al. *First reticule size MAPS with digital output and integrated zero suppression for the EUDET-JRAI beam telescope*. *Nucl. Instrum. Methods Phys. Res.*, A, 623(1):480 – 482, 2010. 1st International Conference on Technology and Instrumentation in Particle Physics.

- [52] Jozef Stefan Institute and Department of Physics, University of Ljubljana, SI-1000 Ljubljana, Slovenia.
- [53] D Žontar, V Cindro, G Kramberger, and M Mikuž. *Time development and flux dependence of neutron-irradiation induced defects in silicon pad detectors*. *Nucl. Instrum. Methods Phys. Res., A*, 426(1):51 – 55, 1999.
- [54] A Dierlamm. *Silicon sensor developments for the CMS Tracker upgrade*. *Journal of Instrumentation*, 7(01):C01110, 2012.
- [55] H Behnamian. *Sensor R&D for the CMS outer tracker upgrade for the HL-LHC*. *Journal of Instrumentation*, 9(04):C04033, 2014.
- [56] Hamamatsu Photonics. <http://www.hamamatsu.com/eu/en/index.html>.
- [57] K. H. Hoffmann. *Campaign to identify the future CMS tracker baseline*. *Nucl. Instrum. Meth.*, A658:30–35, 2011.
- [58] Karl-Heinz Hoffmann. *Development of new sensor designs and investigations on radiation hard silicon strip sensors for CMS at the Large Hadron Collider during the high luminosity phase*. PhD thesis, KIT, Karlsruhe, Dept. Phys., 2013.
- [59] Alexandra Junkes. *Influence of radiation induced defect clusters on silicon particle detectors*. PhD thesis, Hamburg U., 2011.
- [60] Robert Jeraj Matjaz Ravnik. *Research Reactor Benchmarks*. *NUCLEAR SCIENCE AND ENGINEERING*, 145:145–152, 2003.
- [61] E. Curras et al. *Radiation hardness and precision timing study of Silicon detectors for the CMS High Granularity Calorimeter (HGC)*. *Nucl. Instrum. Methods Phys. Res., A*, (AIDA-2020-PUB-2016-004), May 2016. In press.
- [62] E. Currás, M. Mannelli, M. Moll, S. Nourbakhsh, G. Steinbrueck, and I. Vila. *Radiation hardness study of Silicon Detectors for the CMS High Granularity Calorimeter (HGCAL)*. *Journal of Instrumentation*, 12(02):C02056, 2017.
- [63] Robert Eber. *Investigations of new Sensor Designs and Development of an effective Radiation Damage Model for the Simulation of highly irradiated Silicon Particle Detectors*. PhD thesis, KIT, Karlsruhe, Dept. Phys., 2013.
- [64] Convolutd Landau and Gaussian fitting function. <https://root.cern.ch/root/html/tutorials/fit/langaus.C.html>.

- 
- [65] Sebastian N. White. *R&D for a Dedicated Fast Timing Layer in the CMS Endcap Upgrade*. *Acta Phys. Polon. B Proc. Suppl.*, 7:743, 2014.
- [66] Stéphane Fartoukh. *Pile up management at the high-luminosity LHC and introduction to the crab-kissing concept*. *Phys. Rev. ST Accel. Beams*, 17:111001, Nov 2014.
- [67] N. Akchurin, E. Curras, et al. *On the timing performance of thin planar silicon sensors*. *Nucl. Instrum. Methods Phys. Res., A*, 859:31 – 36, 2017.
- [68] T. Mäenpää et al. *Silicon beam telescope for {LHC} upgrade tests*. *Nucl. Instrum. Methods Phys. Res., A*, 593(3):523 – 529, 2008.
- [69] W. R. Leo. *Techniques for Nuclear and Particle Physics Experiments: A How to Approach*. 1987.
- [70] Arabella Martelli et al. *Results of beam-tests of HGCALE diodes for fast-timing measurements*. AIDA-2020 First annual meeting, DESY. 2016.
- [71] Francisca Javiela Muñoz Sánchez and Ivan Vila Alvarez. *Study of New Silicon Sensors for Experiments at Future Particle Colliders*. PhD thesis, Cantabria U., 2014.
- [72] H. Foeth, R. Hammarström, and C. Rubbia. *On the localization of the position of the particle along the wire of a multiwire proportional chamber*. *Nuclear Instruments and Methods*, 109(3):521 – 524, 1973.
- [73] P. Schübelin, J. Fuhrmann, S. Iwata, V. Radeka, W.N. Schreiner, F. Turkot, A. Weitsch, and R.W. Sancton. *Low mass cylindrical multiwire proportional chamber with unambiguous dual coordinate readout*. *Nuclear Instruments and Methods*, 131(1):39 – 46, 1975.
- [74] R. B. Owen and M. L. Awcock. *One and Two Dimensional Position Sensing Semiconductor Detectors*. *IEEE Transactions on Nuclear Science*, 15:290–303, 1968.
- [75] V. Radeka. *Signal, Noise and Resolution in Position-Sensitive Detectors*. *IEEE Transactions on Nuclear Science*, 21(1):51–64, 1974.
- [76] R. Turchetta. *Spatial resolution of silicon microstrip detectors*. *Nucl. Instrum. Methods Phys. Res., A*, 335(1):44 – 58, 1993.
- [77] Alivaba system. <http://www.alibavasystems.com>.

- [78] Beetle - a readout chip for LHCb.  
<http://www.kip.uni-heidelberg.de/lhcb/>.
- [79] Cadence - Spectre Circuit Simulator. <https://www.cadence.com>.
- [80] N. Bacchetta et al. *SPICE analysis of signal propagation in Si microstrip detectors*. *IEEE Transactions on Nuclear Science*, 42(4):459–466, Aug 1995.
- [81] D. Bassignana, E. Curras, et al. *2D position sensitive microstrip sensors with charge division along the strip: Studies on the position measurement error*. *Nucl. Instrum. Methods Phys. Res., A*, 732:186 – 189, 2013. Vienna Conference on Instrumentation 2013.
- [82] Hendrik Jansen and othes. *Performance of the EUDET-type beam telescopes*. *EPJ Techniques and Instrumentation*, 3(1):7, 2016.
- [83] E. Belau et al. *Charge collection in silicon strip detectors*. *Nuclear Instruments and Methods in Physics Research*, 214(2):253 – 260, 1983.
- [84] ATLAS. <https://home.cern/about/experiments/atlas>.
- [85] CMS. <https://home.cern/about/experiments/cms>.
- [86] ALICE. <https://home.cern/about/experiments/alice>.
- [87] LHCb. <https://home.cern/about/experiments/lhcb>.